UNIVERSITY OF CALIFORNIA SAN DIEGO
SAN DIEGO STATE UNIVERSITY

Experimental and Computational Studies of Silver Nanoparticles in Solution and on Sensitized Solar Cells

A dissertation submitted in partial satisfaction of the
requirements for the degree
Doctor of Philosophy

in

Chemistry

by

Martha Patricia Zepeda Torres

Committee in charge:

University of California San Diego

Professor Michael Galperin
Professor Amitabha Sinha

Committee in charge:

San Diego State University

Professor David Pullman, Chair
Professor Douglas Grotjahn
Professor Sam Kassegne

2021

The dissertation of Martha Patricia Zepeda Torres is approved, and it is acceptable in quality and form for publication on microfilm and electronically:

_____

_____

_____

_____

_____

Chair

University of California San Diego

San Diego State University

2021

DEDICATION

To the person who has been with me since the beginning of this long journey,

Luis.

EPIGRAPH

I was taught that the way to progress was neither swift nor easy.

—Marie Curie

TABLE OF CONTENTS

LIST OF FIGURES

LIST OF TABLES

ACKNOWLEDGEMENTS

I would like to thank Dr. Pullman for his guidance during my time in his laboratory. Also, I would like to thank my family for everything they have done for me especially my mom who has made innumerable sacrifices for me to get an education.

Chapter 6 contains material that is being prepared for a publication. Yamamoto, N; Torres, M; Harris, D,; Pullman, D.P. "Seedless, one-pot synthesis of infrared-absorbing silver nanoparticles". *Manuscript in preparation*. I would like Nobu Yamamoto for his work on this project.

VITA

2013	B.S. in Chemistry, University of California Los Angeles, Los Angeles
2013-2020	Graduate Teaching Assistant, San Diego State University, San Diego
2021	Ph.D. in Chemistry, University of California San Diego San Diego State University, San Diego

ABSTRACT OF THE DISSERTATION

Experimental and Computational Studies of Silver Nanoparticles in Solution and on Sensitized Solar Cells

by

Martha Patricia Zepeda Torres

Doctor of Philosophy in Chemistry

University of California San Diego, 2021
San Diego State University, 2021

Professor David Pullman, Chair

Silver nanoparticles (AgNPs) have been investigated for many years now due to their exceptionally strong absorption and scattering of light and to their antimicrobial capabilities. These properties are the basis of many applications such as chemical sensors, Surface-enhanced Raman Spectroscopy, antimicrobial textiles, and medical devices with sterilized surfaces. AgNPs have also been added to solar cells in an attempt to enhance the photoefficiency. Thus far the results have been mostly unsuccessful. For this reason, the purpose of this project was to try a new approach to adding AgNPs to enhance the efficiency of solar cells in which the AgNPs

are separated from the surface by distances on the order of 1nm, and they have a size and shape such that they absorb and scatter light in the red and near-infrared (near-IR) regions where the absorption by solar cells is low. Experimental results of the work are presented in which the efficiency of bare thin silicon solar cells was modestly increased by about 1%. These results prove a proof of concept that can lead to further explorations. Computer simulations that use the discrete dipole approximation (DDA) were also carried out to provide theoretical guidance to the experiments. In separate work the DDA was used to simulate the UV-Visible/ near-IR extinction spectra of the AgNPs that were synthesized in solution for the solar cell project. The solution phase simulations along with Transmission Electron Microscopy (TEM) images of the AgNPs provided a cross check of the origins of the structure in the experimental UV-Visible/ near-IR spectrum.

Chapter 1

Introduction

Solar power is the most abundant renewable energy source.[1] However, one of the challenges with solar power has been obtaining high efficiency solar cells. The efficiency of solar cells was calculated by Shockley-Queisser[2] based on the band gap of one p/n junction of semiconductors. The most used and readily available p/n junction solar cells are composed of silicon. Using the bandgap of silicon of 1.1 eV, the maximum efficiency of silicon solar cells can be about 30%. In practice solar cells used on commercial and residential buildings are typically about 20% efficient, while thin silicon and amorphous silicon solar cells used in consumer products usually show even lower efficiencies that come down to about 10%. One reason for this decrease is the fact that thin silicon solar cells absorption coefficient, between 700 and 1100nm, decreases by a factor of 500.[3] As a result, we were interested in light trapping the energy from this region by using silver nanoparticles.

Silver nanoparticles (AgNPs) have been investigated for many years now due to their strong surface plasmon resonance[4] and antimicrobial capabilities.[5] These properties are the basis of applications such as Surface-enhanced Raman Spectroscopy,[6] biological sensing,[7] and antimicrobial surface coatings.[8] Additionally, in recent years, there has been an interest in adding

AgNPs to devices such as solar cells in an attempt to improve their efficiency. A possible mechanism behind this enhancement is that the excitation of the Localized Surface Plasmon Resonance (LSPR) of metal nanoparticles, specifically gold and silver, leads to an intense electric field in the vicinity of the nanoparticle.[9] which could potentially lead to an enhanced absorption of light by the solar cell. There have been studies that demonstrate that the use of metal nanostructures in solar cells create a stronger field and greater absorption enhancement.[10] Multiple approaches have been taken to achieve this enhancement, from depositing silver islands onto solar cells,[11] to having nucleated AgNPs separated from the solar cell by a dielectric layer,[12] to embedding silver nanostructures within the solar cell. These approaches sometimes demonstrate a small increase in the efficiency of solar cells, but the results thus far are inconclusive. A new way of adding the AgNPs to the solar cells that could bypass some issues is to separate the AgNPs from the surface by an ultra-thin insulating layer whose thickness can be optimized. This control can be achieved through the use of linker molecules to attach the AgNPs to the solar cells. Linker molecules are bifunctional molecules in which one end binds to the surface while the other binds to the nanoparticle. Because the length of the linker molecule can be varied, the use of a linker molecule enables the distance between the solar cell and nanoparticle to be tuned precisely from a few angstroms to above a nanometer.

For this reason, the purpose of this research project was to investigate the use of linker molecules as a means of chemically attaching AgNPs to solar cell surfaces in order to improve the efficiency of solar cells. Specifically, our focus was on thin silicon solar cells, which have a low optical absorption in the region from 700 nm to 1100 nm. Solar energy in this region is wasted and as a result, we used AgNPs that scatter and absorb light in this region.

The first step of this project was to synthesize AgNPs that scatter and absorb light in the red and near-infrared (near-IR) region. Specifically, the nanoparticles we used are triangular in shape with an edge length of about 50 nm or greater. Chapter 2 describes in detail the two routes taken to accomplish the synthesis of these nanoparticles.

Before the synthesized red and near-IR absorbing and scattering nanoparticles were attached to solar cells, computational simulations were used to determine the optimal conditions for the interaction between AgNPs and silicon surfaces. Chapter 3 describes how we simulated the interaction between AgNPs and silicon surfaces using the program Discrete Dipole Scattering (DDSCAT).

Following the results from DDSCAT, the next step was to attach a linker molecule to the solar cell. We started the process by using silicon wafers as the trial material. Silicon wafers provided a more stable surface to attach bifunctional molecules and how this was accomplished will be discussed in Chapter 4.

Once the process was proven to work on silicon wafers, it was duplicated but this time using thin silicon solar cells. The final step was to attach the near-infrared scattering AgNPs to the linker molecule by adding AgNPs solution to the surface of modified thin silicon solar cells. Chapter 5 describes in detail the process of functionalizing the thin silicon solar cells with linker molecules, attaching the AgNPs to the modified surfaces followed by the testing of the photoefficiency.

Finally, the UV-Visible-near-IR extinction spectra of the AgNPs that were synthesized in solution for the solar cell project showed an unusually broad peak and we wanted to understand the origin of this broadness. Computer simulations using DDSCAT were used to simulate the solution phase spectra. Chapter 6 is dedicated to determining the optical properties of AgNPs in solution that would accurately describe the behavior taking into consideration experimental factors such as the refractive index of the medium, the size distribution of the AgNPs (as determined by Transmission Electron Microscopy), and the tumbling motion of the AgNPs in solution.

1.1 References

1. Parida, B.; Iniyan, S.; Goic, R. A Review of Solar Photovoltaic Technologies. *Renewable and Sustainable Energy Reviews* **2011**, *15* (3), 1625-1636.

2. Shockley, W.; Queisser, H. J. Detailed Balance Limit of Efficiency of p-n Junction Solar Cells. *Journal of Applied Physics* **1961**, *32* (3), 510-519.

3. Atwater, H. A.; Polman, A. Plasmonics for Improved Photovoltaic Devices. *Nature Materials* **2010**, 9, 205–213.

4. Jensen, T. R.; Malinsky, M. D.; Haynes, C. L.; Van Duyne, R. P. Nanosphere Lithography: Tunable Locazied Surface Plasmon Resonance of Silver Nanoparticles. *The Journal of Physics Chemistry B* **2000**, *104*, 10549-10556.

5. Sondi, I.; Siiman, O.; Matijevic, E. Synthesis of CdSe Nanoparticles in the Presence of Aminodextran as Stabilizing and Capping Agent. *Journal of Colloid and Interface Science* **2004**, *275*, 503-507.

6. Cao, Y. C. Nanoparticles with Raman Spectroscopic Fingerprints for DNA and RNA Detection. *Science* **2002**, *297*, 1536-1540.

7. Moulin, E.; Sukmanowski, J.; Luo, P.; Carius, R.; Royer, F. X.; Stiebig, H. Improved Light Absorption in Thin-Film Silicon Solar Cells by Integration of Silver Nanoparticles. *Journal of Non-Crystalline Solids* **2008**, *354*, 2488-2491.

9. Zheng, G.; Xu, L.; Lai, M.; Chen, Y.; Liu, Y.; Li, X. Enhancement of Optical Absorption in Amorphous Silicon Thin Film Solar Cells with Periodical Nanorods to Increase Optical Path Length. *Optics Communications* **2012**, *285*, 2755-2759.

10. Scholl, J. A.; Koh, A. L.; Dionne, J. A. Quantum Plasmon Resonances of Individual Metallic Nanoparticles. *Nature* **2012**, *483*, 421-427.

11. Pillai, S.; Catchpole, K. R.; Trupke, T.; Green, M. A. Surface Plasmon Enhanced Silicon Solar Cells. *Journal of Applied Physics* **2007**, *101*, 093105.

12. Chen, X.; Jia, B.; Saha, J. K.; Cai, B.; Stokes, N.; Qiao, Q.; Wang, Y.; Shi, Z.; Gu, M. Broadband Enhancement in Thin-Film Amorphous Silicon Solar Cells Enabled by Nucleated Silver Nanoparticles. *Nano Letters* **2012**, *12*, 2187-2192.

Chapter 2

Synthesis of Near-Infrared Absorbing Silver Nanoparticles

2.1 Introduction

The first part of the project was to synthesize silver nanoparticles (AgNPs) that absorb light in the infrared region. The importance of having AgNPs that absorb in the near-infrared region is to capture the solar energy that is not captured by thin silicon solar cells. More specifically, the goal is to enable the solar cells to capture the energy of light between 700 and 1100 nm, where the absorption coefficient of silicon decreases by a factor 500.[1]

Two methods of synthesis were investigated: photochemical and simultaneous chemical reduction and oxidation. In both methods, silver was reduced with sodium borohydride in the presence of trisodium citrate acting as the capping agent. The difference between them was the use of light for the photochemical method and the addition of sodium borohydride and hydrogen peroxide for the chemical method. The photochemical method also relies on the use of small, pre-made silver nanospheres as a reagent, while the chemical method is a one-pot technique.

Both methods led to the synthesis of AgNPs that absorbed light in the infrared region. However, the photochemical approach took several days to give the desired nanoparticles. As a result, we tried a second method, not involving light, in which sodium borohydride was added to a solution containing hydrogen peroxide, silver ions, and sodium citrate. Using this method, we synthesized the needed nanoparticles within ten to twenty minutes.

Figure 2.1 shows the UV-visible absorption spectra of the AgNPs synthesized by these two approaches compared to AgNPs synthesized by the commonly used method of borohydride reduction.[2]As shown in the figure, the blue curve shows the AgNPs synthesized by the photochemical method compared to the green curve that shows the triangular AgNPs synthesized by the borohydride/peroxide /reduction/oxidation method. The yellow curve shows the AgNPs synthesized using the standard borohydride reduction method in which peroxide is not added. The borohydride reduction method produces 5-10 nm diameter nanospheres that serve as the seeds for the photochemical method, while the photochemical method produces mostly hexagonal nanoparticles, and the chemical method produces nanotriangles.

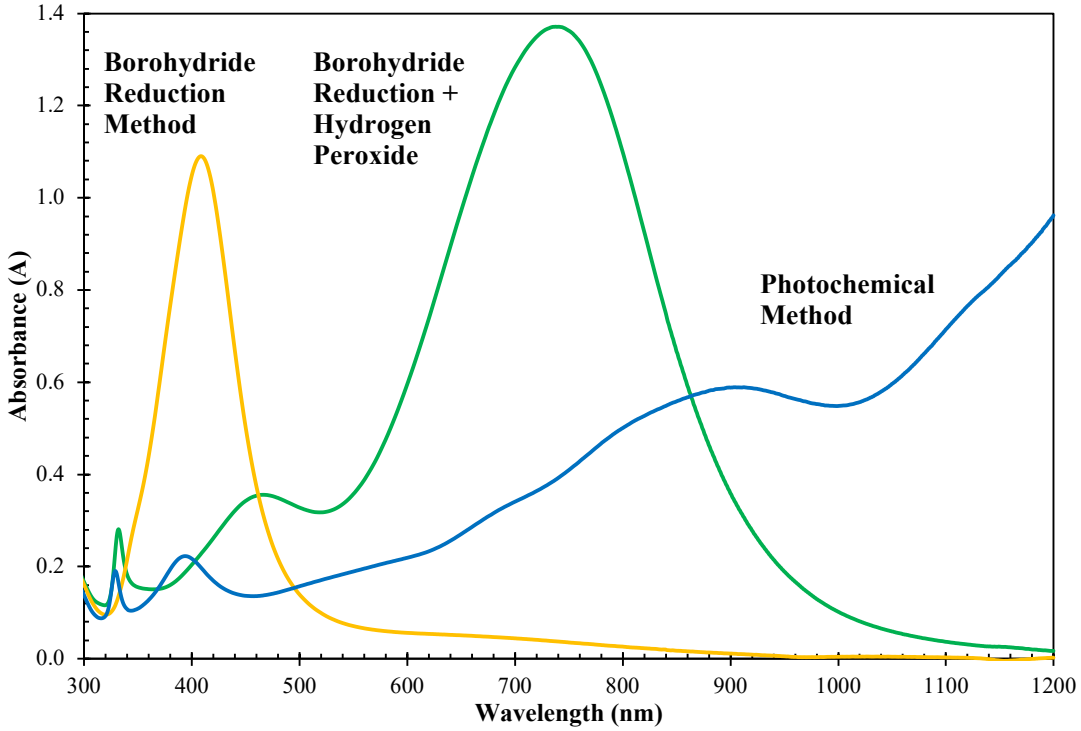

Figure 2.1: UV-Visible-Near-Infrared absorption spectra of spherical (yellow curve) and triangular (green and blue curve) AgNPs.

2.2 Photochemical Method

The photochemical method requires the use of previously synthesized 5-10 nm spherical AgNPs in aqueous solution, produced by reducing silver ions with sodium borohydride in the presence of sodium citrate of small spherical AgNPs using sodium citrate as the capping agent and sodium borohydride as the reducing agent. These spherical nanoparticles were then photochemically converted to the large triangles by exposing them to intense red light ($\sim$15 mW/cm^2) while periodically adding more trisodium citrate. Jin *et al.* discussed the important role that the citrate ion plays for the growth of AgNP.[3] This was the reason why we decided to keep adding trisodium citrate to the solution to replenish this ion. The progress of the reaction was monitored using UV-Visible-Near-Infrared absorption spectroscopy, as shown in the Results and Discussion section.

2.2.1 Materials

Silver nitrate of 99.9% purity was purchased from Fisher Scientific, and due to its light sensitivity, it was stored in a dark cabinet. Trisodium citrate of $>$ 99.9% purity was also purchased from Fisher Scientific. Sodium borohydride of 99% purity was purchased from Acros Organics and stored in a vacuum desiccator due to its hygroscopic nature. Photoexcitation of the reaction sample was carried out in a small chamber designed and constructed in the Pullman Lab. The chamber contained a high-power red LED (LED Engin, 630 nm peak wavelength, 3 W), a magnetic stirrer, and a fan for cooling the sample to maintain it at room temperature. The light flux at the sample was 15mW/cm^2, as measured with a calibrated photodiode (Thorlabs, model S130C). A schematic diagram of the light box is shown in Figure 2.2.

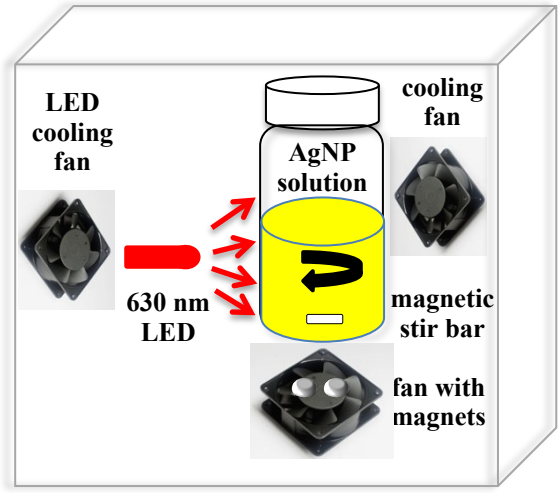

Figure 2.2: Schematic of the red LED photoexcitation box used for the synthesis of the photogrown AgNPs.

2.2.2 Preparation and Experimental Procedure

Stock solutions of 4.5 mM silver nitrate and sodium citrate were prepared using 5 Mohm deionized (DI) water and stored in a dark cabinet. To produce AgNPs by the photochemical method, first spherical AgNPs were synthesized using silver nitrate as the source of silver, sodium

borohydride as a reducing agent, and sodium citrate as the capping agent. The mechanism of producing the spherical AgNPs involves the sodium borohydride reduction of silver ions to atomic silver,[4] which then aggregate to form small clusters of silver atoms. The function of the sodium citrate is to bind to the surface of the nanoparticles and electrostatically prevent aggregation of them. The specific procedure used in our work was published by our lab.[2] To make a 12 mL solution, 7.8 mL of deionized (DI) water, 0.6 mL of 4.5 mM silver nitrate, and 0.6 mL of 4.5 mM sodium citrate were added to a vial and stirred. A solution of 0.45 mM sodium borohydride was then made. Immediately after making the borohydride solution, 3.0 mL were added slowly at a rate of 1 drop per second to the vial using a pipette. In the final volume of 12 mL, the concentrations of the different species-assuming no reaction occurred-would be [silver nitrate] = [sodium citrate] = 0.225 mM and [sodium borohydride] = 0.1125 mM. Since each borohydride (BH_4-) can in principle reduce four Ag^+ ions, excess hydride is present. This is necessary since some of the borohydride reacts with the water, diminishing the available hydride concentration.

We confirmed the synthesis of the spherical AgNPs using UV-Visible-Near-Infrared spectroscopy. We collected the samples on a Jasco V-670 spectrometer equipped with a temperature controller (EHC-746) using quartz cuvettes of 1 cm pathlength and DI water as the background. The temperature was set to 22.0 °C. The solutions were diluted with a 1:2 dilution ratio before taking their spectrum.

Once the synthesis of the spherical AgNPs was confirmed using UV-Visible-Near-Infrared spectroscopy, the vial was exposed to the high-power red LED contained in the photoexcitation chamber shown in Figure 2.2. After an exposure of 24 hours, the vial was removed from the light, a UV-Visible-Near-Infrared spectrum was taken. Then, because the photochemical reaction involves the oxidation of citrate (and thus citrate is lost), 0.6 mL of 4.5 mM sodium citrate was added to the mixture to replenish the citrate. The same process was repeated two more times. In the end, the nanoparticle solution was exposed to 96 hours of red LED, and the extra amount of sodium citrate that was added in the three aliquots was 1.8 mL.

2.2.3 Results and Discussion

In the first part of the synthesis, one can immediately recognize if spherical AgNPs were made since when the sodium borohydride is added to the vial, the solution changes color from clear to yellow. The yellow color is the result of the solution absorbing light at about the 400 nm wavelength.

The spectra in Figure 2.3 show the progress of the photogrown reaction as it was exposed to the red LED. The first spectrum taken was right after the synthesis of the spherical AgNPs; it is shown in red and has a maximum absorbance at 396 nm. The next spectrum was taken after exposing the spherical AgNPs solution for 24 hours to the red LED (no aliquot of sodium citrate was added). The recorded spectrum is shown in blue and with a change in 820 nm region, indicating that the solution was composed of the smaller spherical nanoparticles and larger nanoprisms. The next spectrum of the AgNPs solution was recorded after adding the first aliquot of citrate (0.6 mL) and exposing it to the red LED for another 24 hours, total LED time of 48 hours. The resulting spectrum (green curve) shows that the peak in the 820 nm region increased in absorbance, there was an appearance of a peak at 1200 nm region and most importantly the peak near 400 nm disappeared. All of this indicated the growth of the larger nanoprisms. The process of adding an aliquot of citrate and exposing the solution to 24 hours of LED time was repeated twice. The corresponding spectra are shown in Figure 2.3, yellow curve (2 aliquots of citrate and 72 hours of LED exposure) and purple curve (3 aliquots of citrate and 96 hours of LED exposure).

To illustrate the importance of adding additional aliquots of sodium citrate, absorption spectra were recorded of a control spherical AgNPs solution that was exposed to the red LED without adding the aliquot of sodium citrate, but instead adding aliquots of DI water. The control solution (gray curve) was the result of exposing the solution to 96 hours of red LED and 1.8 mL of added DI water (3 aliquots of DI water). The other control curves of 24, 48 and 72 hours of

exposure to red LED and that correspond to 0, 1 and 2 aliquots of added DI water, respectively, are not displayed to keep the graph from being congested.

From the control spherical AgNPs solution (gray curve), one can see that adding the citrate was crucial in converting the smaller spherical AgNPs into the larger nanoprisms since there was still a peak at 400 nm after exposing the solution to 96 hours of red LED. In contrast, after 96 hours of red LED exposure and a total of 1.8 ml of sodium citrate added, there was no peak at 400 nm indicating that there were mainly larger nanoprisms and almost no spherical nanoparticles. This change was confirmed with Scanning Electron Microscopy (SEM). An example of a SEM image taken is shown in Figure 2.4. This image shows that there were mainly larger triangular nanoprisms with sharp tips and some with truncated tips on the photogrown AgNPs solution.

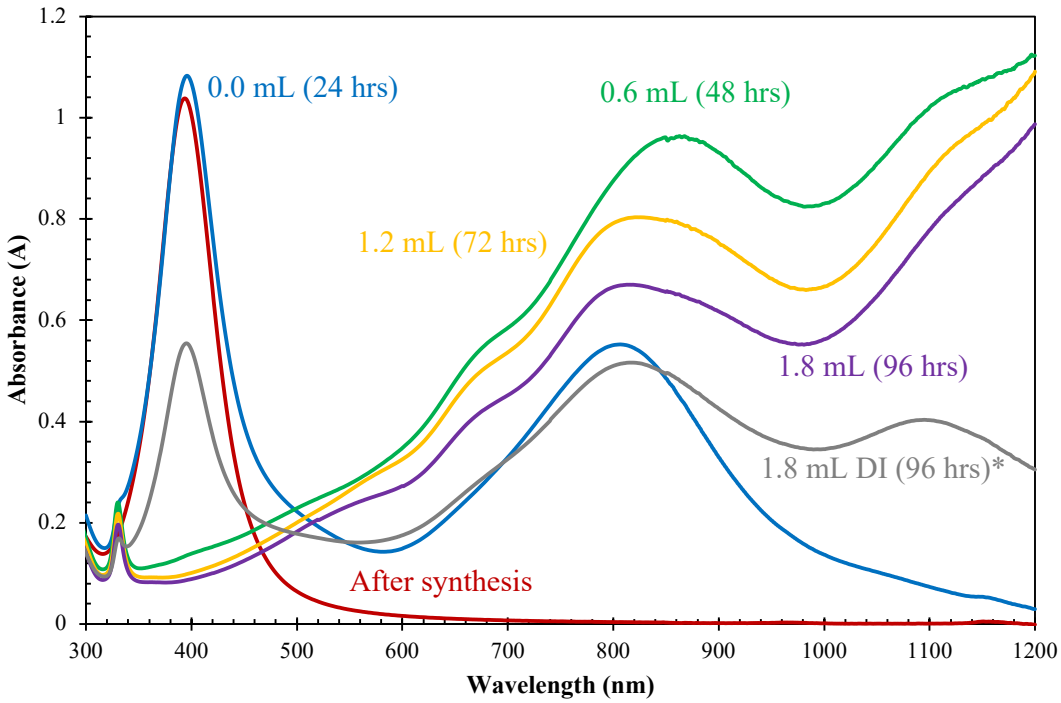

Figure 2.3: UV-Visible-Near-Infrared absorption spectra monitoring the appearance of photogrown AgNPs. Note that the control solution (gray curve) is marked with an asterisk. Total aliquot volume is shown next to each corresponding curve along with the total LED exposure time, shown in parenthesis

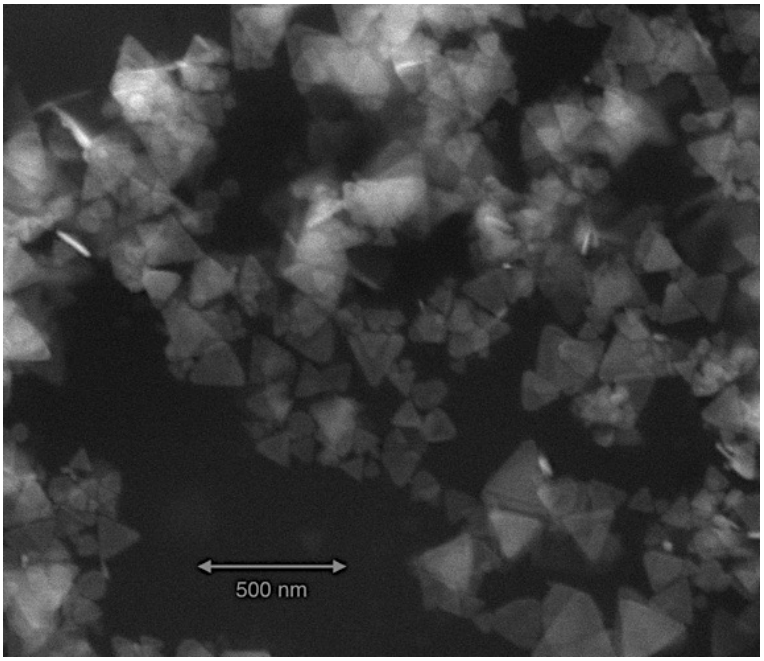

Figure 2.4: SEM image of photogrown AgNPs solution (96 hours LED and 1.8 ml sodium citrate) on a silicon surface.

We briefly attempted to isolate the larger AgNPs from the other large AgNPs by centrifuging the solution for 10 minutes at 10,000 rpm (Eppendorf, model 5430) and resuspending the pellet in DI water. Figure 2.5 shows the nanoparticle solution after being exposed to 96 hours and 1.8 ml of citrate added before and after the solution was centrifuged. From this graph, one can see the peaks remain in the same location, indicating that the centrifugation was not successful in separating the larger nanoparticles. Furthermore, although the photochemical method was successful in synthesizing triangular nanoparticles, the time it took was a drawback. Therefore, we decided to research a different method that was less time consuming.

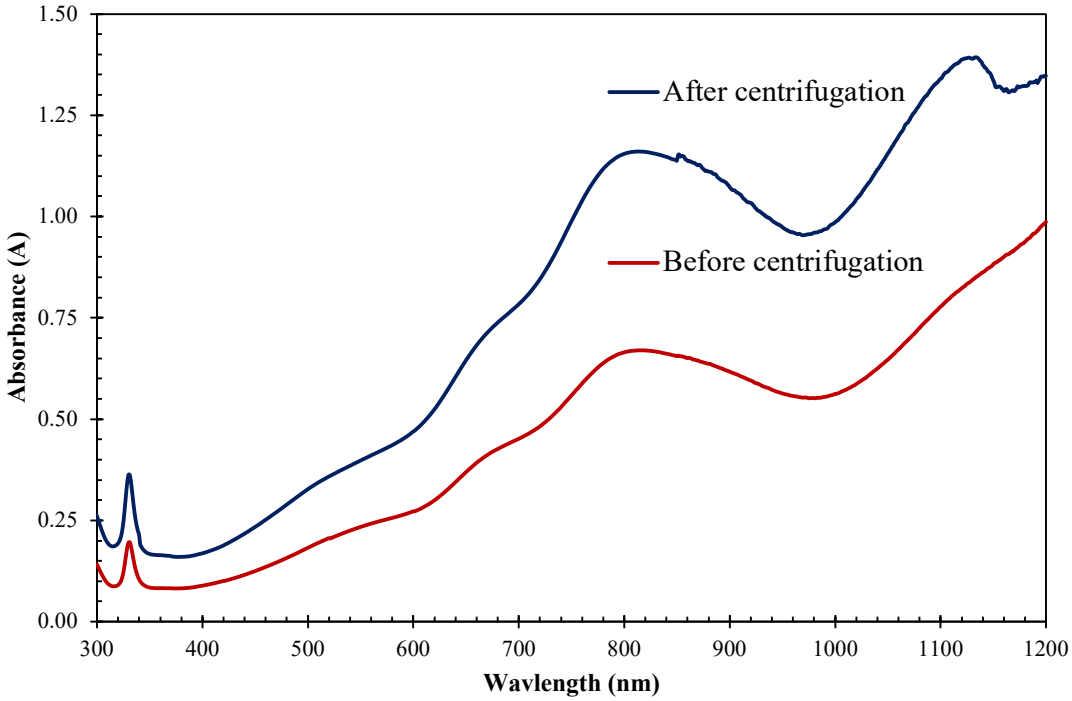

Figure 2.5: UV-Visible-Near-Infrared absorption spectra of AgNPs solution after being exposed to red LED for 96 hours and 1.8 ml sodium citrate added before being centrifuged (red) and after being centrifuged (blue). Note that the concentrations of solution before and being centrifuged are different.

2.3 Production via Chemical Reduction and Oxidation

The other method used to synthesize the near-infrared absorbing AgNPs involved the simultaneous use of hydrogen peroxide as an etching agent and sodium borohydride as a reducing agent; exposure to the red light was not needed. For this synthesis, sodium citrate was used as capping agent.The synthesis takes about 10 minutes, compared to four days for the photochemical method. As a result of this, the borohydride reduction/peroxide oxidation method was the one selected for future AgNP syntheses.[5]

2.3.1 Materials

Trisodium citrate of >99.9% purity was purchased from Fisher Scientific. Sodium borohydride of 99% purity was purchased from Acros Organics and stored in a vacuum desiccator due to its hygroscopic nature and reaction with water. Silver nitrate of 99.9% purity was purchased from Fisher Scientific and stored in a dark cabinet due to its light sensitivity. Hydrogen peroxide 30% was purchased from Acros Organics and stored in a 4°C refrigerator.

2.3.2 Preparation and Experimental Procedure

Stock solutions of 0.1 M sodium citrate and 0.1 M silver nitrate were made using 5 Mohm deionized (DI) water. Using the experimental procedure outlined by Panzarasa[5], and by Zhang *et al.*,[6] multiple vials with solutions of 20 mL each were prepared at the same time. The first step was to add 12.83 mL of deionized (DI) water, 444 μL of 0.1 M silver nitrate, 6.67 mL of the sodium citrate, and 56 μL of 30% hydrogen peroxide to each clean vial, which were then stirred vigorously for 10 minutes. While the solutions were stirring, a 0.1 M sodium borohydride solution was prepared. The sodium borohydride solution degrades after it is made and as a result while the solutions containing sodium citrate and silver nitrate were stirring, the sodium borohydride solution was prepared. Once the reactant solution was mixed for 10 minutes, the stirring rate was decreased and 200 μL of 0.1 M sodium borohydride solution was added slowly to each vial.

2.3.3 Results and Discussion

Immediately after adding the sodium borohydride, the solution changed color from clear to yellow, indicating the presence of small AgNPs. After a reaction time of 3 minutes, the solution slowly changed color from yellow to blue. The transition of colors indicated the growth to larger AgNPs.

Hydrogen peroxide was added to the solution as a means of limiting the size and shape

of the AgNPs. Zhang *et al.* show that hydrogen peroxide disturbs the dynamic equilibrium by removing other less stable structures making the citrate more susceptible to binding to the (1 1 1) plane of the silver surface. The (1 1 1) surfaces are protected, and as a result, silver atoms tend to add along the edges of the nanoparticle, leading to the triangular nanoparticles.

To determine if we synthesized AgNPs that absorb in red and near-infrared region, we recorded UV-Visible-Near-Infrared absorption spectra of the solutions. Figure 2.6 compares a spectrum for AgNPs obtained using the hydrogen peroxide method (blue curve, blue-colored solution) to a spectrum obtained for small spherical AgNPs (yellow curve, yellow solution) produced with the standard borohydride reduction method (no added peroxide). From this graph, the blue solution has a much higher absorbance in the desired region between 700 to 1000 nm. Also, evident is a smaller peak at around 470 nm corresponding to smaller nanoparticles.

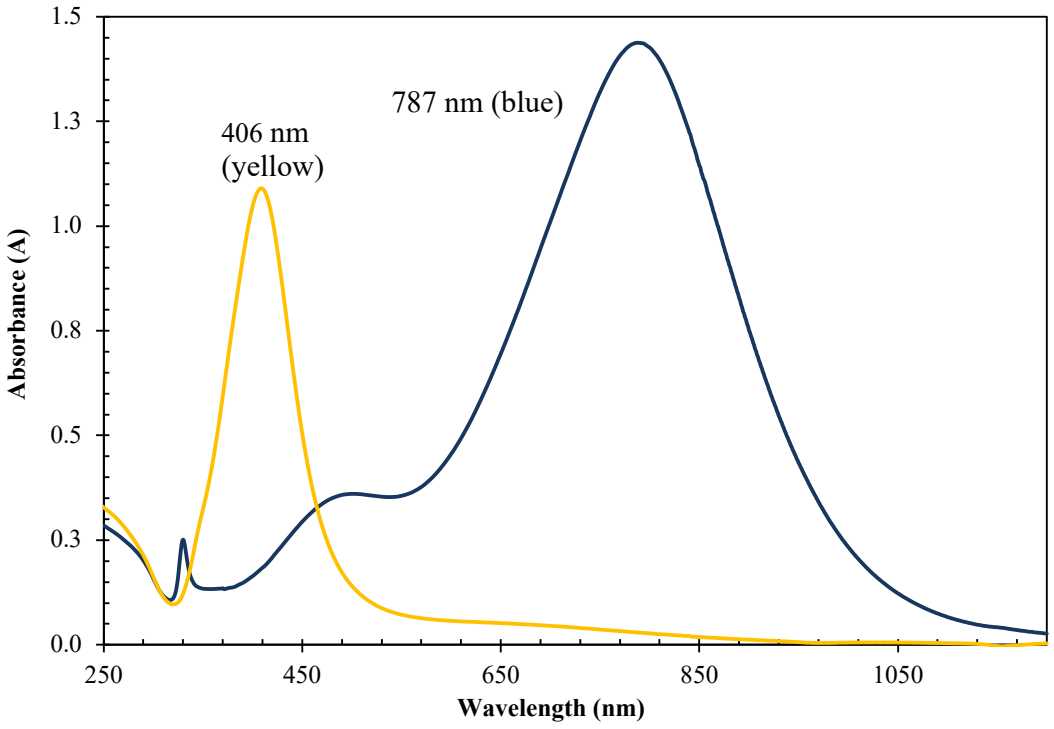

Figure 2.6: UV-Visible-Near-Infrared absorption spectra of AgNPs produced in the presence of hydrogen peroxide (blue curve, blue solution) compared to sodium borohydride reduced AgNPs (yellow curve, yellow solution).

To separate the smaller nanoparticles, the solution was centrifuged using the same procedure as in the photochemical method. We recorded UV-Visible-Near-Infrared absorption spectra of the solutions, and the results are shown in Figure 2.7. After the centrifugation, the pellet was resuspended in 5.0 mL of DI water and the supernatant was kept. Comparing the spectrum of before centrifugation (blue curve) to after centrifugation (red curve), one can see that the separation was not successful in removing the smaller nanoparticles (i.e., the relative peak sizes remain about the same). Although the peak at 470 nm could potentially be due to the overlapping in-plane and out-plane quadrupole resonance. We will explain these in-plane and out-plane quadrupole resonances in more detail later in chapter 6. The supernatant (green curve) shows some absorbance in the region from 400 to 480 nm region, demonstrating that some of the smaller nanoparticles were indeed separated from the solution. However, also shown is a peak at 620 nm that shows that larger AgNPs were also separated.

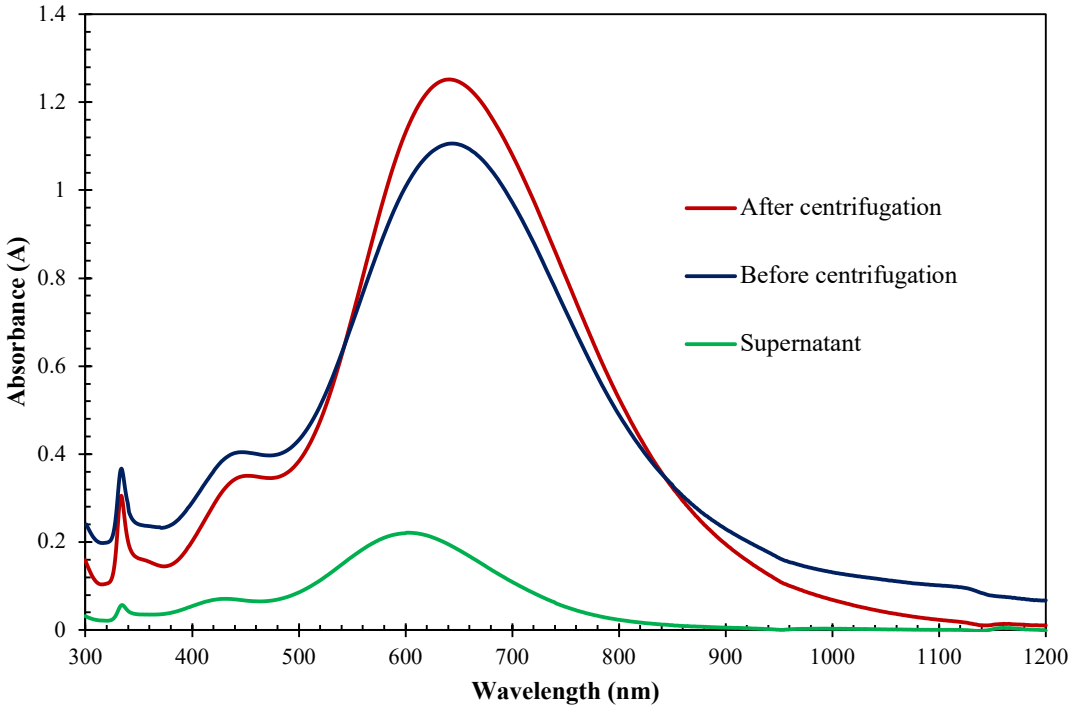

Figure 2.7: UV-Visible-Near-Infrared absorption spectra of AgNPs produced in the presence of hydrogen peroxide before being centrifuged (blue curve), after being centrifuged (red curve) and supernatant (green curve) of centrifuged solution. Note that the concentrations of solution before and being centrifuged are different.

2.3.4 Conclusion

In conclusion, we were able to synthesize AgNPs that absorb light in the red and near-infrared region using two methods. Both methods were successful in the AgNPs synthesis, but the chemical reduction and oxidation method was chosen since it is less time consuming. The chemical reduction and oxidation method AgNPs will be used in Chapter 4 and Chapter 5 to test out their effectiveness in absorbing light in the desired region of 700 to 1000 nm.

2.4 References

1. Atwater, H. A. and Polman, A. Plasmonics for Improved Photovoltaic Devices. *Nature Materials*, **2010**, *9*, 205-213

2. Espinoza, M. G.; Hinks, M. L.; Mendoza, A. M.; Pullman, D. P.; Peterson, K. I. Kinetics of Halide-Induced Decomposition and Aggregation of Silver Nanoparticles. *The Journal of Physical Chemistry C*, **2012**, *116* (14), 8305-8313

3. Jin, R.; Cao, Y., Mirkin; C.A., Kelly, K. L.; Schatz, G. C.; Zheng, J. G. Photoinduced Conversion of Silver Nanospheres to Nanoprisms. *Science*, **2001**, *294*, 1901-1903.

4. Song, K. C.; Lee, S. M.; Park, T. S.; Lee, B. S. Preparation of Colloidal Silver Nanoparticles by Chemical Reduction Method. *Korean Journal of Chemical Engineering* **2009**, *26* (1), 153-155.

5. Panzarasa, G. Just What Is It That Makes Silver Nanoprisms so Different, so Appealing? *Journal of Chemical Education* **2015**, *92* (11), 1918-1923.

6. Zhang, Q.; Li, N.; Goebl, J.; Lu, Z.; Yin, Y. A Systematic Study of the Synthesis of Silver Nanoplates: Is Citrate a "Magic" Reagent? *Journal of the American Chemical Society*, **2011**, *133*, 46 18931-18939

Chapter 3

Modeling The Optical Response of Silver Nanoparticles Bound to Silicon via the Discrete Dipole Approximation

3.1 Introduction

For our project, we theorized the electric field enhancement of silver nanoparticles will enable thin silicon solar cells to capture more of the incoming light. There have been various studies using plasmonic nanostructures to convert the collected light into electric energy to increase photoeffciency.[1−3] The goal of the work presented in this chapter was to determine the optimal conditions for the interaction between silver nanoparticles (AgNPs) and silicon surfaces by using computational simulations. Once the optimal configurations were determined, then the experiments described in Chapters 4 and 5 were optimized using the results from this chapter.

In Chapter 2, we discussed the importance of having silver nanoparticles that absorb light in the region between 700 nm and 1100 nm and how we were able to synthesize such

nanoparticles. Shown in Figure 3.1 is a transmission electron microscopy (TEM) image of these nanoparticles. From the image, one can see that these nanoparticles are triangular in shape and range in edge length size from 10 nm up to 305 nm, with a thickness of 7 nm. The triangular shape is of key importance since the sharp points provide "hot spots" where the electric field is amplified and can potentially interact strongly with the solar cell.

Using the Discrete Dipole Approximation (DDA), which is a method that allows the interaction of light with an array of dipoles in arbitrary-shaped targets to be investigated and the size distribution from Figure 3.1 we modeled the electric field enhancement near the surface of an isolated triangular silver nanoparticle with edge length size, 57.5 nm, and thickness of 7 nm. These dimensions were chosen because they represent averages from the distribution. The next part of the project was to model the interaction of the silver nanoparticle on a silicon surface to determine how the electric field would be affected by changing the nanoparticle-to-silicon distance and the orientation of the nanoparticles with respect to the silicon surface. The final part of the project was to simulate the interaction of possible linker molecules in the space between the nanoparticle and silicon surface.

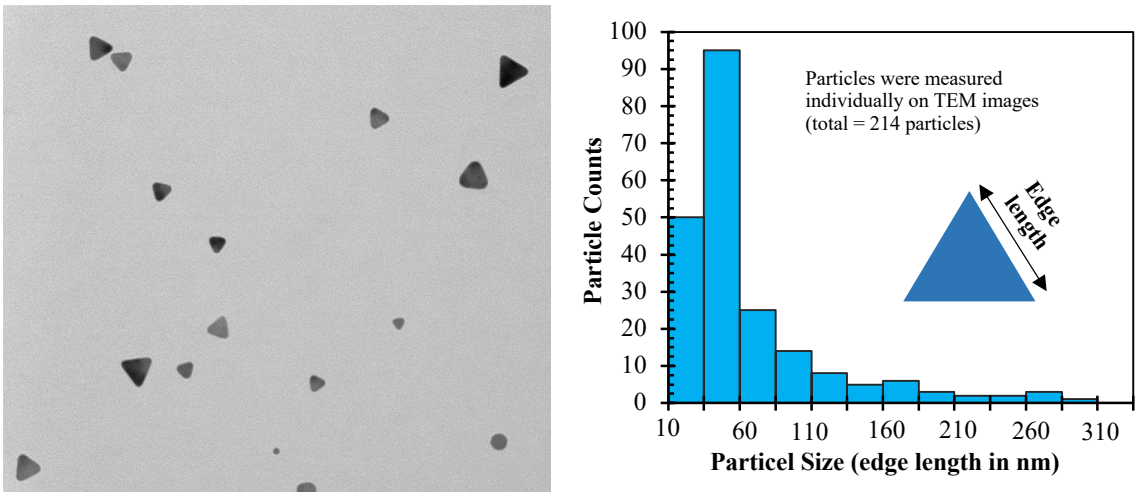

Figure 3.1: TEM image of silver nanoparticle solution (left) and the size distribution of the solution (right) (Images provided by Nobuyuki Yamamoto.

3.2 Discrete Dipole Scattering (DDSCAT) and General Computational Procedure

The Discrete Dipole Scattering (DDSCAT) computer program developed by Draine *et al.*[4] is a numerical implementation of the Discrete Dipole Approximation (DDA) method formulated by Purcell and Pennypacker.[5] The DDA is a powerful technique for calculating the scattering and absorption of light by arbitrarily-shaped particles, as well as the electric field outside of the particles (the "near field"). In this technique, the particle is modeled as a periodic cubic array of polarizable point dipoles placed within the boundary of the particle. What distinguishes one type of material from another is the complex, wavelength-dependent polarizability that is used in the calculation (actually, the user enters the complex, wavelength-dependent index of refraction, which is tabulated for many materials and is related to the polarizability). Effects of the medium in which the particle is embedded can be considered by including the refractive index of the medium.

When light of a given wavelength and polarization is incident on the particle, the optical response is determined in an iterative fashion. Initially, the electric field generated by a polarizable dipole (call it dipole number 1) is calculated. The electric field present at a neighboring dipole (number 2) is then the incident field plus the field generated by dipole number 1. Similarly, the field at dipole number 3 is the incident field plus the field generated by dipoles 1 and 2. Once all the dipoles have been stepped through, the field generated by dipole number 1 is recalculated, except now the field that dipole 1 experiences is the incident field plus the fields due to all the other dipoles. This process is repeated until the fields have converged within a user-selected tolerance.

To run the DDSCAT program, three input files are needed, all of which are text files: the shape and parameter files, as well as a file containing the complex refractive index of the

material as a function of wavelength. The shape file contains the coordinates of all the dipoles for the particle while the parameter file provides the instructions for the calculations including the desired parameters i.e. a pointer to the file containing the wavelength-dependent refractive index of the material, refractive index of the environment, orientation of the particle with respect to the incident light propagation direction and polarization, wavelength or range of wavelengths of the incident light, spacing of the dipoles, etc. To generate the shape file, the size and shape of the particle must first be chosen. In our case, the particle was either a spherical or triangular silver nanoparticle with dimensions of a few nanometers up to a few hundred nanometers, a silicon surface, or a silver nanoparticle in close proximity to a silicon surface. The first step was to draw the nanoparticle and/or silicon surface using a graphics program called Blender.[6] Once drawn, the shape was converted into an array of dipoles using a program called Shape Converter[6], which then created the shape file. In this program, the dipole-to-dipole distance is chosen. Examples of the shape, parameter, and optical dielectric function files are provided in the Appendix A. Using the obtained shape and parameter files and the refractive index file, the DDSCAT calculation was submitted to one of our lab computers (3.6 GHz quad core-i7, 16GB RAM). On these computers, DDSCAT was compiled with the Intel Fortran compiler and linked with the Intel MKL library (Math Kernel Library). The calculation for a nanoparticle with a silicon surface took about 24 hours.

For all the calculations, we used a dipole spacing of 1 nm. Other dipole spacings of 0.5, and 2 nm were investigated (see Figure 3.2). As shown in Figure 3.2, ideally 2 nm would have been better, but the number of dipoles exceed the calculation limit. Therefore, we chose to use a spacing of 1nm, which gives a spectrum that is roughly similar to the 2 nm spacing case. The nanoparticles were modeled as being in air, and thus 1.0 was chosen as the value of the refractive index of the surrounding dielectric medium. The wavelength-dependent optical dielectric function for both silver and silicon were from Green *et al.*[7,8] The scattering, absorption, and extinction cross-sections (C_{sca}, C_{abs}, and C_{ext}, where $C_{ext} = C_{sca} + C_{abs}$) were computed

at wavelengths every 10 nm, and with the incident light coming from the top. By default, the DDSCAT program has the incident wave propagate along the x-axis- i.e., the wave vector, k, lies along the x-axis. The light could be polarized in either the y or z direction. In general, calculations for both polarization directions were done in order to allow simulation of unpolarized light, as would be the case in most actual experiments in which the light source is a solar simulator or the sun. Figure 3.3 illustrates the orientation of a triangular nanoparticle on a silicon surface with respect to the incident radiation. To resemble the experimental conditions, a simulation with periodic boundary conditions was used. Specifically, the silver nanoparticle and silicon surface were repeated along the y-axis.

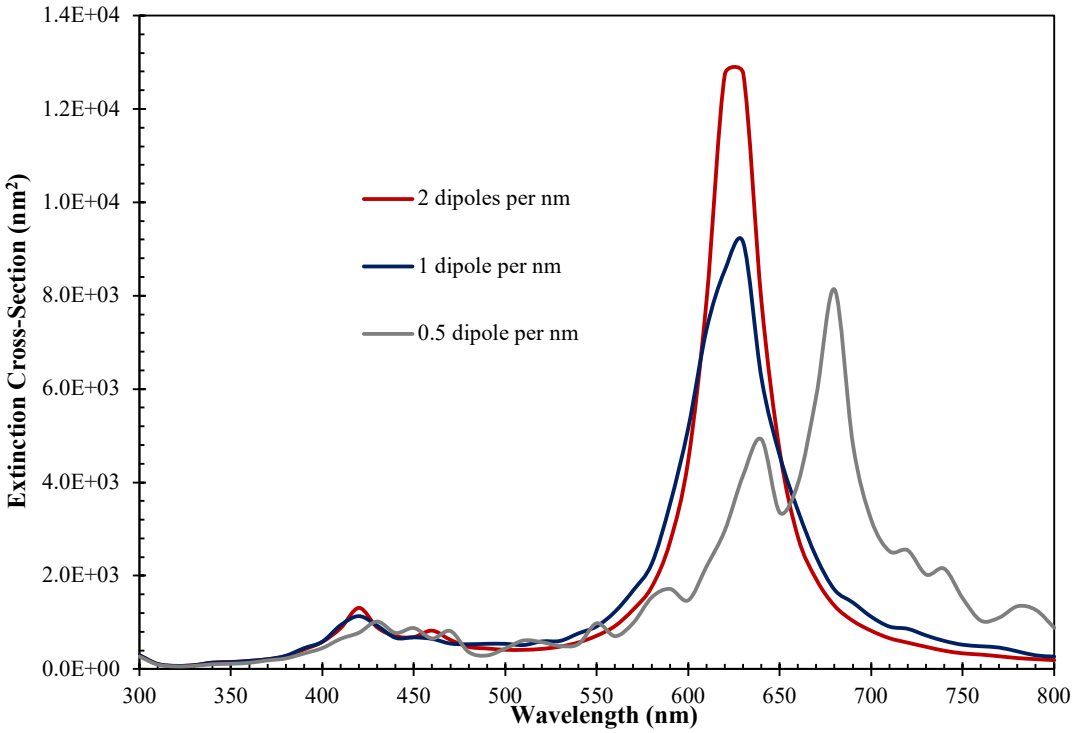

Figure 3.2: Extinction cross-section spectra of a triangular AgNP 57.5 nm in edge length and 7 nm thick with various dipole spacing 0.5 dipole per nm (gray), 1 dipole per nm (blue) and 2 dipoles per nm (red). The index of refraction of the medium is 1.0.

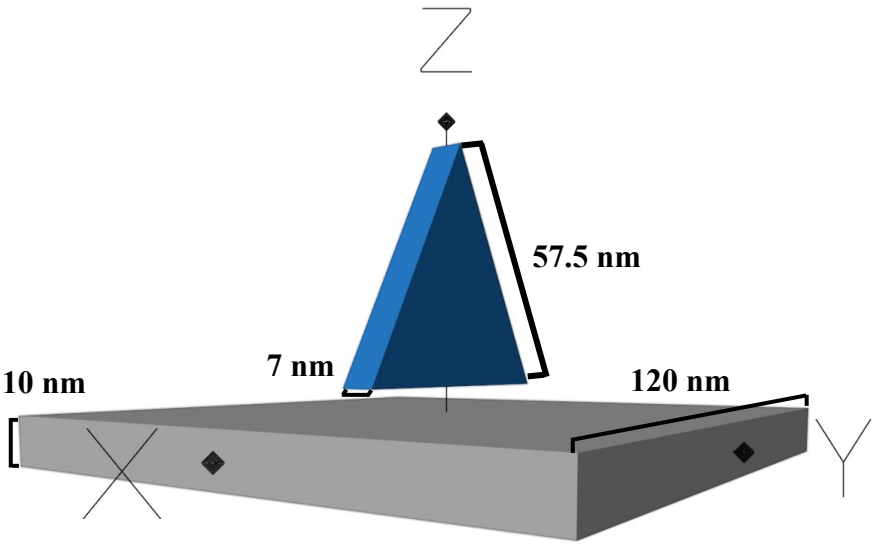

Figure 3.3: Image of a silver nanoparticle (blue) on a silicon surface (gray) illustrating the size and coordinates used.

3.3 Discrete Dipole Approximation Applied to an Isolated Triangular Silver Nanoparticle

The end goal was to simulate the electric field in the vicinity of a silver nanoparticle and a silicon surface. We started by simulating the electric field of a single AgNP. The objective of the first part of the project was to calculate the electric field enhancement of a single triangular nanoparticle. The dimensions used for this simulation were an edge length of 57.5 nm and a thickness of 7 nm (see Figure 3.3). The first part of the simulations was to determine the extinction cross-section over the wavelength range of 300 nm to 1200 nm at every 10 nm. Once the position of the highest extinction peak was determined, the electric field was calculated using this wavelength.

Figure 3.4 shows the extinction spectrum for nanoparticles with 27.5 nm, 57.5 nm, and 87.5 nm edge length and 7 nm thickness using pure water as the surrounding medium (n=1.33). For the 57.5 nm edge length nanoparticle, the principal peak is at 790 nm, with two smaller ones

at 540 nm and 480 nm. The spectrum is comparable to what is found in literature. Using the DDA method for a triangular silver nanoparticle immersed in water and with 60 nm edge length and 12 nm thickness, Hao and Schatz[9] determined that the highest extinction peak occurs at 700 nm. One might have expected that our principal resonance peak should be blue-shifted (i.e., at lower wavelength) relative to theirs because our nanoparticle is 4% smaller in the lateral, in-plane dimensions. The peak is in fact red-shifted because our nanoparticle is thinner by 40%, and the trend is that as the aspect ratio of the nanoparticle increases, the dipole resonance wavelength red shifts.9 The aspect ratio of our 57.5 nm edge length nanoparticle was about 8.2, while that of Hao and Schatz was 5. The aspect ratio of the 27.5 nm edge length nanoparticle was 3.9 compared to the 87.5 nm edge length nanoparticle with an aspect ratio of 12.

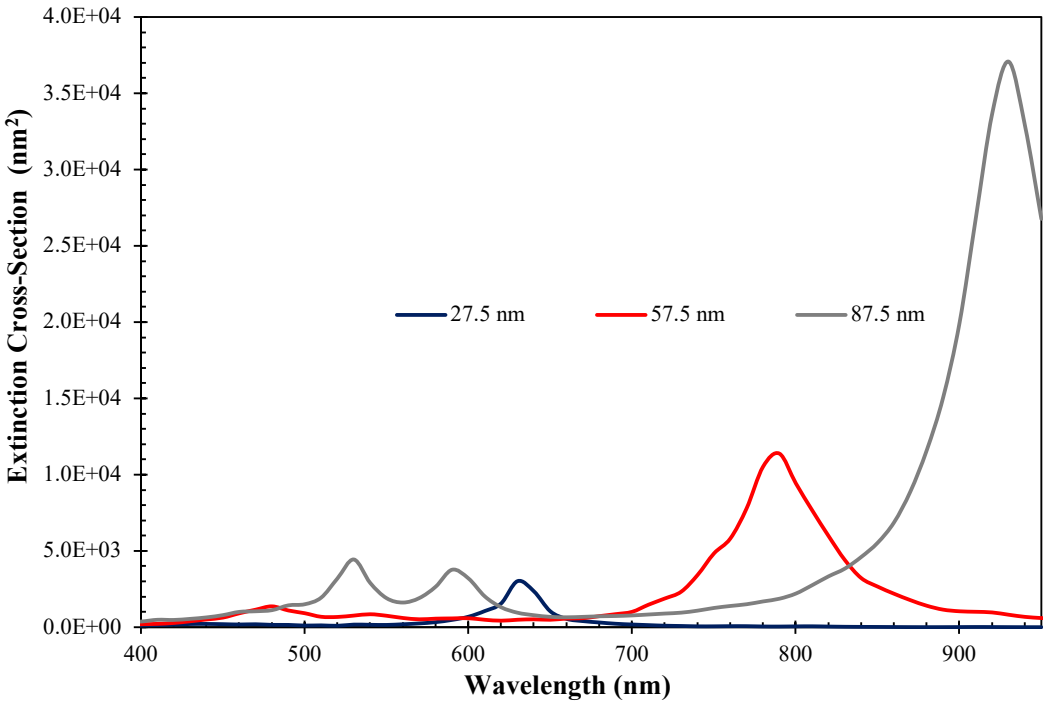

Figure 3.4: Extinction cross-section of a triangular AgNPs 27.5 nm, 57.5 nm and 87.5 nm in edge length and 7 nm thick. Refractive index of the medium was pure water (n=1.33).

Hao and Schatz also showed the electric field contours of a silver triangular nanoparticle and, by analyzing the shape of the contours, were able to identify the peaks as dipolar or

quadrupolar in nature. Similarly, we were able to assign the resonance peaks in our results in Figure 3.4. The in-plane quadrupole resonance was excited at 480 nm, followed by a weak in-plane dipole peak at 540 nm, and the strong in-plane dipole resonance was at 790 nm. In addition to identifying the resonance peaks, the electric field contours (see Figure 3.5) show that the highest electric field enhancement occurs at the tips of the nanoparticle, as one would anticipate.

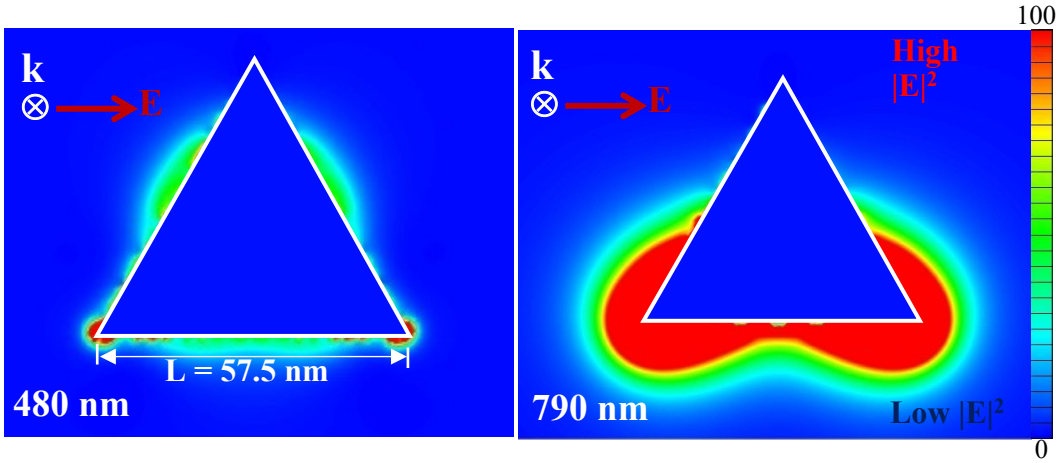

Figure 3.5: Calculated $|E|^2$ contours for a 57.5 nm edge length triangular AgNP of thickness 7 nm using pure water (n=1.33) as the surrounding refractive index medium. Shown are (left) out-plane quadrupole at 480 nm and (right) in-plane dipole at 790 nm. The location of the AgNP is shown as a blue rectangle.

Once we confirmed the electric field enhancement of the 57.5 nm AgNP was comparable with what is found in the literature, we changed the refractive index of the medium from pure water (n =1.33) to air (n =1.0). A refractive index of 1.0 would probably more closely approximate experiment since the solar cells will be air. Figure 3.6 shows the results of decreasing the refractive index of the medium from pure water (n=1.33) to air (n=1.0). From this graph, the effect of decreasing the medium's refractive index blue shifted both main resonance peaks, in-plane dipole, and out-of-plane quadrupole. A detailed explanation for the blue shift of the resonance peaks when decreasing the medium's refractive index will be provided later in Chapter 6. The electric

field contours of the out-plane quadrupole at 420 nm and in-plane dipole at 630 nm are shown in Figure 3.7.

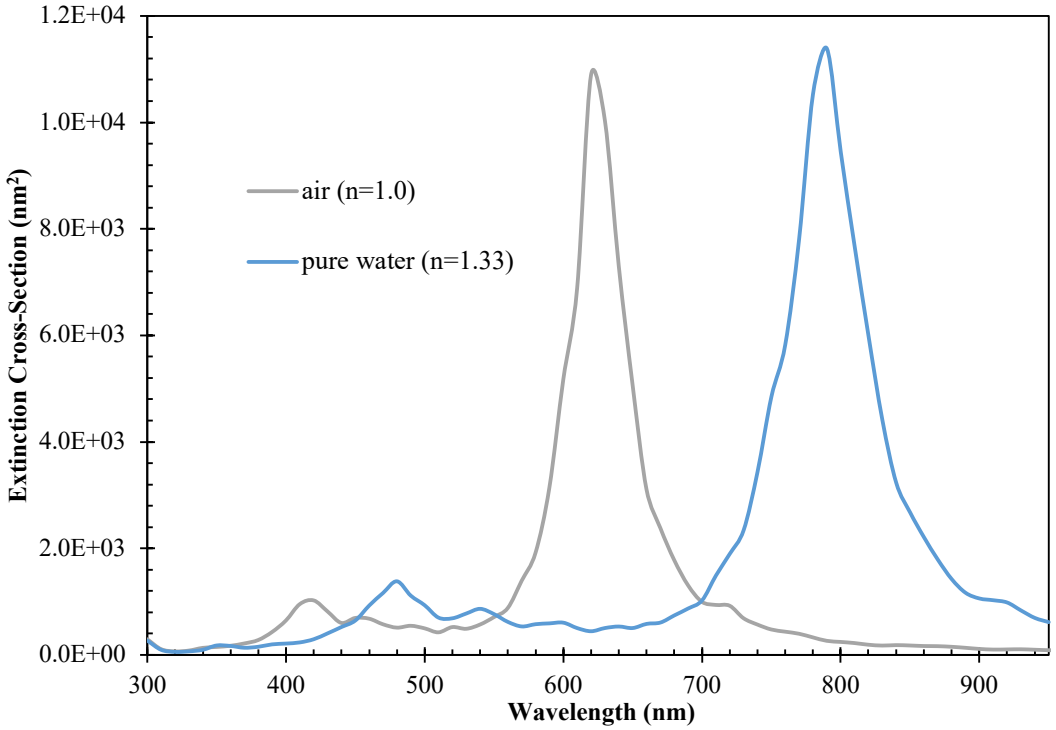

Figure 3.6: Extinction cross-section of a triangular AgNP 57.5 nm in edge length and 7 nm thick with a refractive index of the medium of pure water, 1.33, (blue) compared to air, 1.0, (gray).

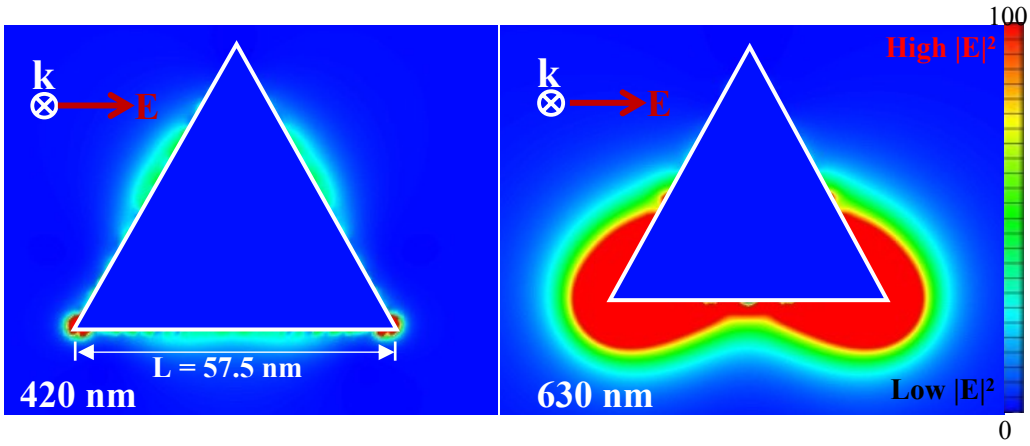

Figure 3.7: Calculated $|E|^2$ contours for a 57.5 nm edge length triangular AgNP of thickness 7 nm using air (n =1.0) as the surrounding refractive index medium. Shown are (left) out-plane quadrupole at 420 nm and (right) in-plane dipole at 630 nm. The location of the AgNP is shown as a blue rectangle.

3.4 Effect of Changing the Polarization of Incident Light

For this portion of the project, we wanted to see the effect of changing the polarization direction of the incident light. In the previous calculations, the incident light was polarized along the edge of the AgNP (y-direction) in the corresponding axis. Since the coordinates in DDSCAT can get complicated, due to having a lab and target frame, two polarizations directions A and B were assigned to a direction of the AgNP. Figure 3.8 shows the AgNP with its axis and both polarization directions A and B.

The general trend in the extinction spectrum, illustrated in Figure 3.8 was that changing the polarization of the light from the A to the B directions led to a decrease in the amplitude of the 630 nm peak but little change in the 420 nm peak (without shifting the peaks significantly) and a splitting of the 630 nm peak.

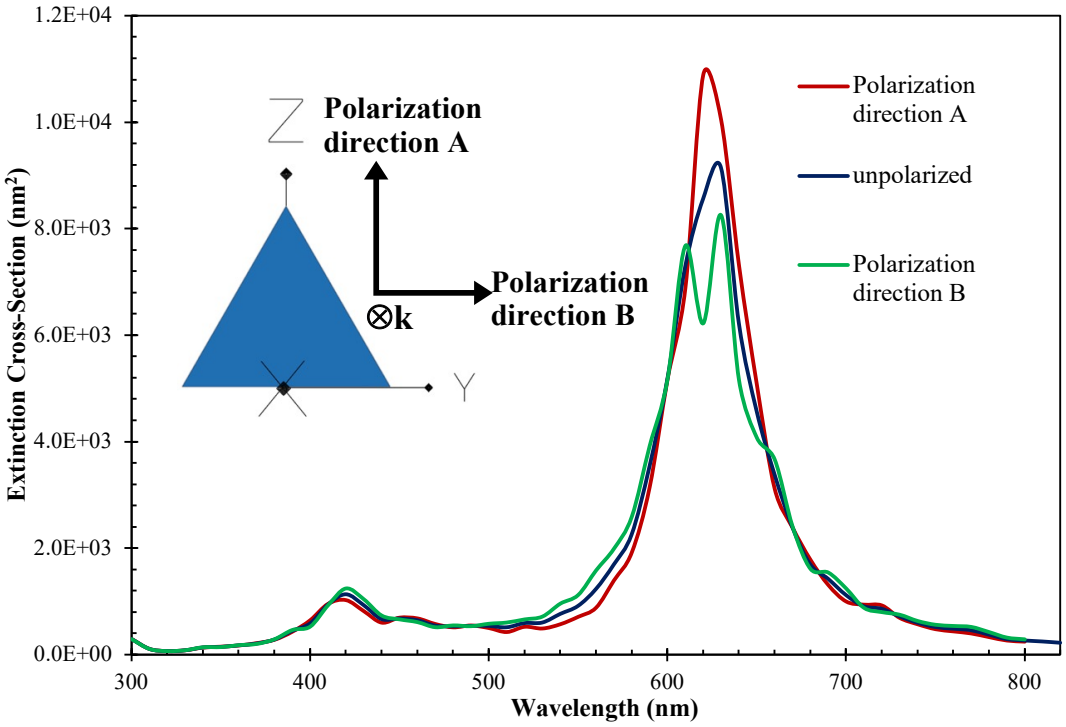

Figure 3.8: Extinction cross-section results of changing the incident of light from polarization direction A (red), polarization direction A (green) and unpolarized (blue). Also, shown is a AgNP that shows both polarization directions in respect to k vector.

3.5 Silver Nanoparticle and Silicon Surface Simulations

Once the simulations of a single isolated nanoparticle were done, we used DDSCAT to determine the electric field enhancement of a nanoparticle on a silicon surface. The size of the triangular nanoparticle used was the same as the previous calculation, 57.5 nm in edge length and 7 nm in thickness. To ensure that the entire nanoparticle was interacting with the silicon surface and not with neighboring nanoparticles, the silicon was modeled as a large, 120 nm by 120 nm rectangular slab with a thickness of 10 nm. Other sizes of 150, 140 and 130 nm silicon surface were investigated but the number of dipoles exceeded the calculation limit.

The silver nanoparticle and silicon surface were repeated along the y-axis with periodic boundary conditions to take into account the experimental conditions. Additionally, three orien-

tations between nanoparticle and silicon surface were modeled: the silver nanoparticle flat on silicon surface (*orientation 1*), the silver nanoparticle rotated 90° on x-axis in respect to the silicon surface (*orientation 2*) using *orientation 1* as the starting position, and silver nanoparticle rotated 90° on x-axis and 60° on y-axis in respect to the silicon surface (*orientation 3*) using *orientation 1* as the starting position. Figure 3.9 illustrates the top and front view of these three orientations used for simulations of nanoparticle on the silicon surface. Also shown are coordinates and direction of the k vector.

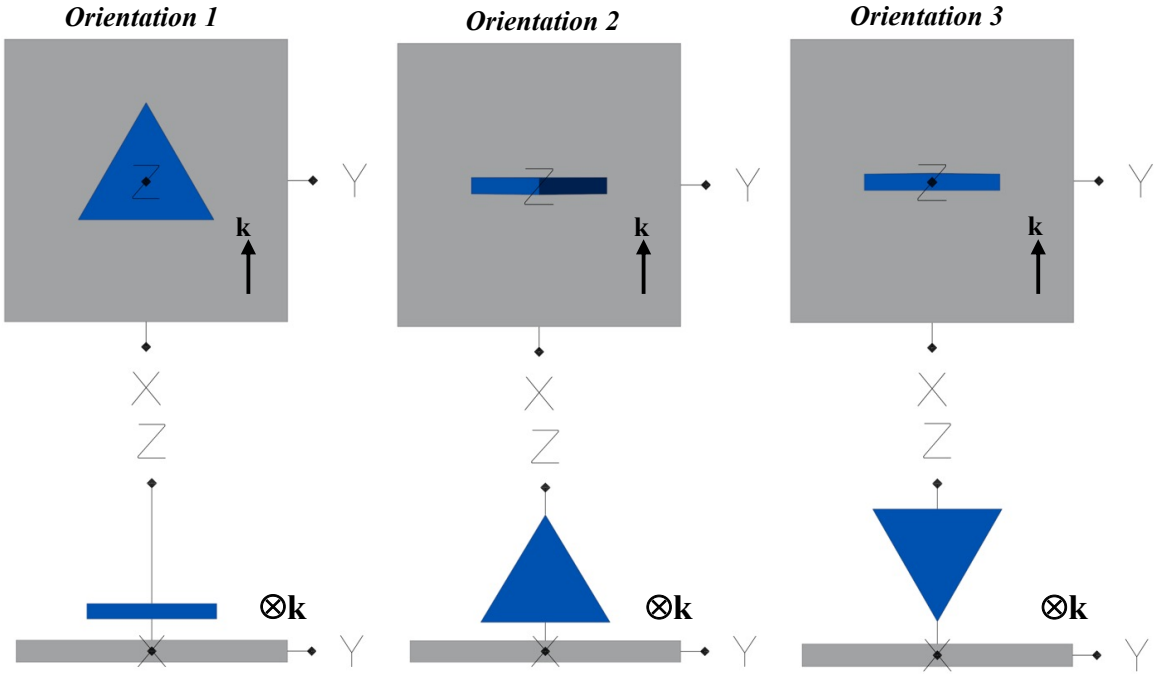

Figure 3.9: Top view (top) and side view (bottom) of various orientations of a silver nanoparticle bound to a surface. The program, Blender, was used to generate the images.

3.6 Effect of Changing Nanoparticle-to-Silicon Distance

Shown in Figure 3.9 is a silver nanoparticle flat on a silicon surface (*orientation 1*) as one of the possible orientations between nanoparticle and silicon surface. Using this orientation, the electric field enhancement was calculated as the distance between the silver nanoparticle and the

silicon surface was increased. The distances used were 0 nm, 1 nm, 2 nm, 3 nm, 5 nm and 20 nm, chosen to take into consideration the size of possible linker molecules. Some of these possible linker molecules were pentanoic acid, decanoic acid, and hexadecanoic acid for 1 nm, 2 nm and 3 nm respectively.

Figure 3.10 shows the results for the extinction cross-section of a of a triangular AgNP 57.5 nm in edge length and 7 nm thick lying flat on a silicon surface as the distance between them was increased with a refractive index of the medium of air (n=1.0). The general trend shown in Figure 3.10 is that as the nanoparticle-to-silicon distance increases, the peak wavelength shifts to lower wavelengths. This makes sense because as the distance becomes large, one would expect the spectrum to approach that for an isolated nanoparticle, and as shown previously in this chapter, the peak for the isolated nanoparticle occurs at 630 nm.

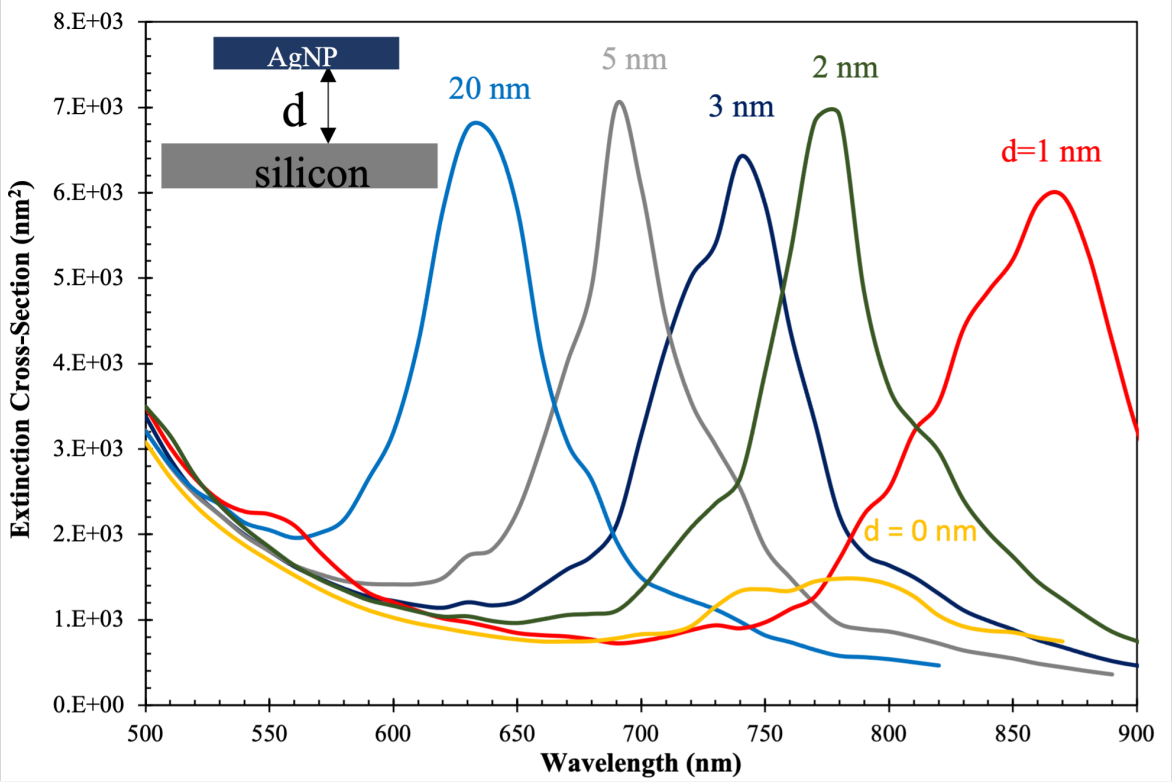

Figure 3.10: Extinction cross-section spectra of a triangular AgNP 57.5 nm in edge length and 7 nm thick lying flat on a silicon surface as the nanoparticle-to-silicon surface distance, d, increases. Here, d is defined as the distance between the bottom of the nanoparticle and the top of the silicon slab. Refractive index of the medium was air (n=1.0).

Table 3.1 shows the peak wavelength and extinction cross-section as a function of nanoparticle-to-silicon distance, d. The lowest extinction cross-section was the result of having the nanoparticle and silicon surface in direct contact (d= 0 nm). The resonance peak occurs at 780 nm and suggests that adding silver nanoparticles directly onto thin solar cells would lead to the least improvement in the solar cell efficiency. As mentioned in Chapter 1, previous studies using silver nanoparticles added silver nanoparticles directly onto solar cells saw little to no improvement in solar cell efficiency. This lack of absorbance is a possible explanation as to why this led to little to no increase in photoefficiency. In contrast, the peak corresponding to d =2 nm (nanoparticle -to-silicon distance) also occurred at 780 nm with an extinction cross-section value that was more than 4 times higher that nanoparticle and silicon surface in direct contact (d= 0

nm). All of this confirmed that having a set distance between the nanoparticle and silicon was fundamental in enhancing the electric field.

Table 3.1: Table summarizing the results of the extinction cross-section spectra of a nanoparticle lying flat on a silicon surface as the nanoparticle-to-silicon surface distance, d, increases.

Nanoparticle-to-silicon distance, d (nm)	**Wavelength (nm)**	**Extinction Cross- Section (nm^2)**
0	780	1.48E+03
1	870	5.96E+03
2	780	6.91E+03
3	740	6.42E+03
5	690	7.03E+03
20	630	6.76E+03

The electric field intensity ($|E|^2$)calculated for nanoparticle-to-silicon distances of d = 1 nm, 3 nm, and 20 nm is shown in Figure 3.11 as the front view (yz plane) of the nanoparticle on the silicon surface. The electric field was calculated at the wavelength of the highest extinction cross-section peak shown in Figure 3.10. The nanoparticle-to-silicon distance of 2 nm showed the highest electric field enhancement in the region between the nanoparticle and silicon surface. At this distance, the peak extinction cross-section occurs at 780 nm, within the desired wavelength region of 700 to 1100 nm. The nanoparticle-to-silicon distance of 20 nm, with an extinction cross-section peak at 630 nm, was located at the infinite distance where the isolated silver nanoparticle (infinite distance) had an extinction cross-section peak at 630 nm. Along with the results shown on Figure 3.11 of the electric field enhancement, we determined that linker molecules larger than 20 nm would be too long to provide an electric field enhancement. Using the results of these calculations, we concluded that shorter linker molecules between 1 to 5 nm in length would provide the highest enhancement of the electric field.

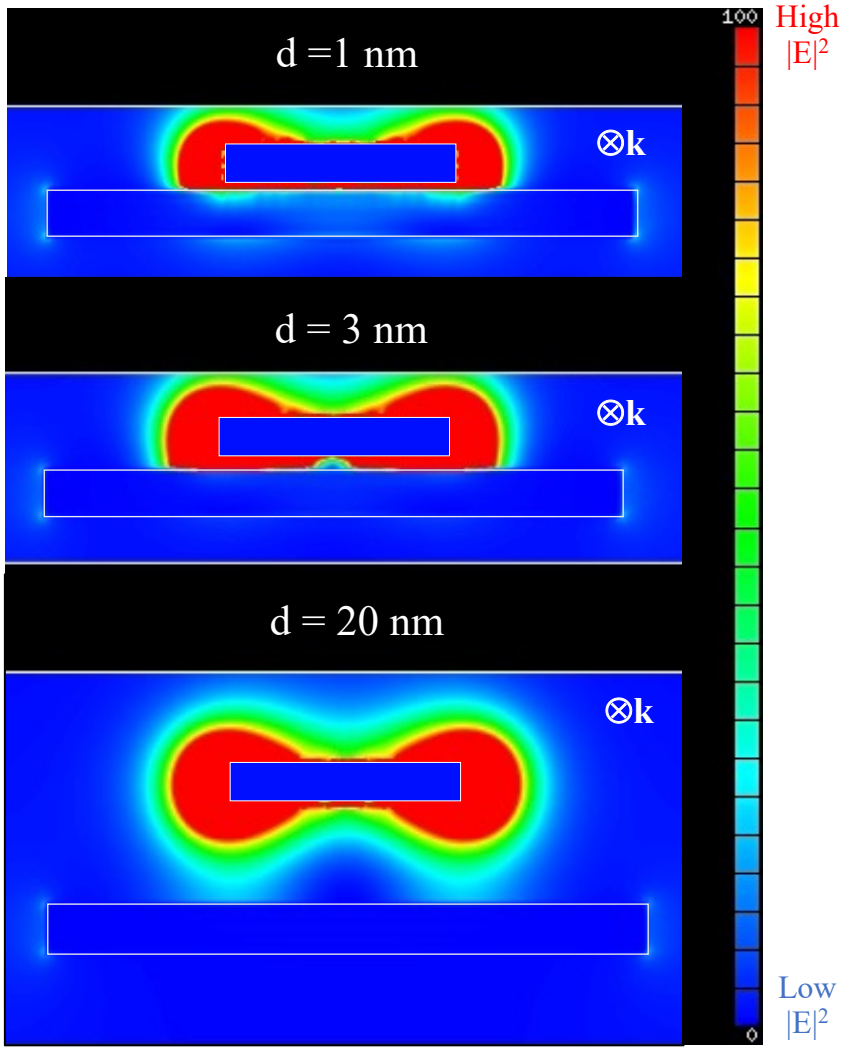

Figure 3.11: Calculated $|E|^2$field contours for a 57.5 nm edge length triangular AgNP of thickness 7 nm flat on a silicon surface with 120 nm side and 10 nm thickness. Shown are the results of nanoparticle-to-silicon surface distance (top) 1m (middle) 3 nm and (bottom) 20 nm. The silicon surface is outlined while the location of the AgNP is shown as a blue rectangle.

3.7 Effect of Nanoparticle Orientation on Extinction Cross-Section

The effect of orientation of the silver nanoparticle with respect to the silicon surface was modeled using 3 nm as the silver-to-silicon surface distance, The three orientations between

nanoparticle and silicon surface modeled were: silver nanoparticle flat on surface (*orientation 1*), silver nanoparticle rotated 90° on x-axis in respect to the silicon surface (*orientation 2*) using *orientation 1* as the starting position, and silver nanoparticle rotated 90° on x-axis and 60° on y-axis in respect to the silicon surface (*orientation 3*) using *orientation 1* as the starting position, illustrated in Figure 3.9. In addition, the light was unpolarized to resemble experimental conditions. The results of these calculations are shown in Figure 3.12.

Figure 3.12 illustrates the effect of a triangular silver nanoparticle orientation on a silicon surface on the extinction spectrum. From this graph you can observe that changing the orientation of the nanoparticle on the silicon surfaces decreases and shifts the cross-sectional extinction peak compared to the previous simulation (*orientation 1*) shown earlier in the chapter.

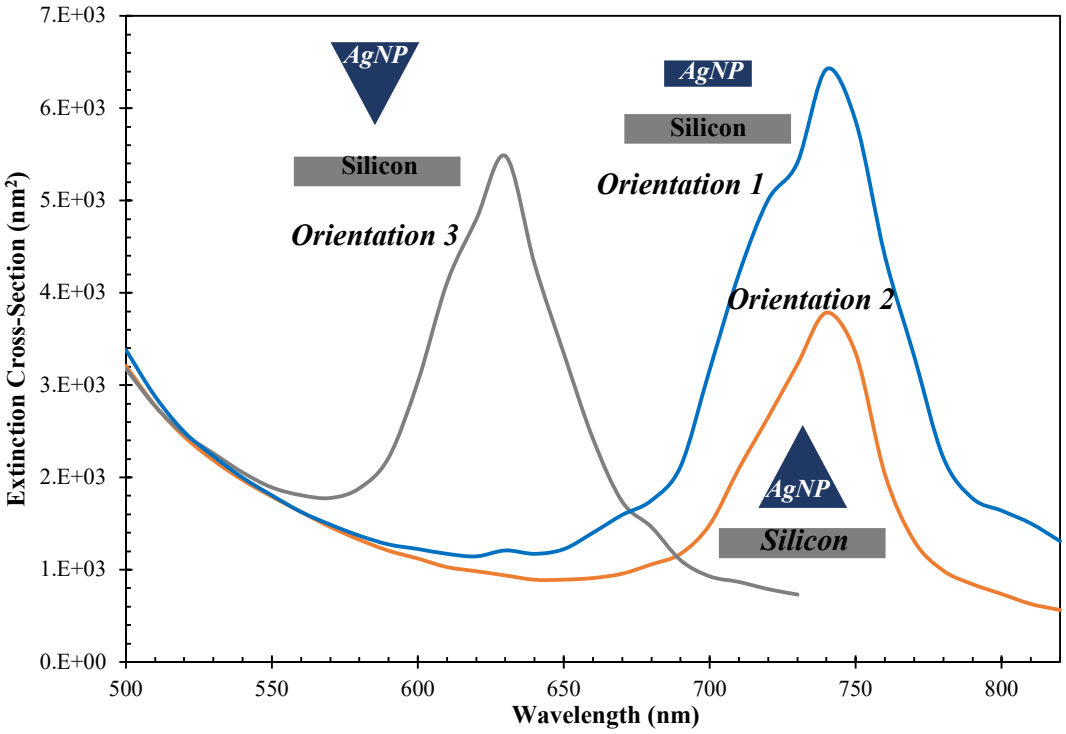

Figure 3.12: Extinction cross-section spectra of the three orientations of the AgNP orientation over the silicon surface with the incident of light being unpolarized.

For the remaining of the calculations, we used *orientation 1*. The reason for this was that based on the TEM image, this orientation seems to be the most probable out of all three.

3.8 Effect of Linker Molecules on Extinction Cross-Section

The next part of the project was to simulate the effect of having linker molecules interact with the silver nanoparticle and the silicon surface. This was done by using rough estimates of the dielectric constant of possible linker molecules that would fit in the vicinity of the silver-to-nanoparticle distances. The chosen linker molecules were hexadecanoic acid, decanoic acid and pentanoic acid for 3 nm, 2 nm, and 1 nm respectively. The refractive index values were 1.4309 for hexadecanoic acid[10], 1.4288 for decanoic acid[11] and 1.4086 for pentanoic acid.[12]

The results of these calculations are shown in Figures 3.13 and 3.14. Figure 3.13 illustrates the cross-sectional extinction of a linker molecule compared to their corresponding nanoparticle-silicon distance. Adding the liker molecule red shifted the cross-sectional extinction peak wavelength and broadening this peak. A plausible explanation for the peaks to red shift could be due to the difference in dielectric constant. The chosen linker molecules had a dielectric constant higher than air, when the incident light from the top interacted with the linker layer, it had a higher optical density to pass through. This led to the light being scattered in more directions and eventually shifting and broadening the extinction peak.

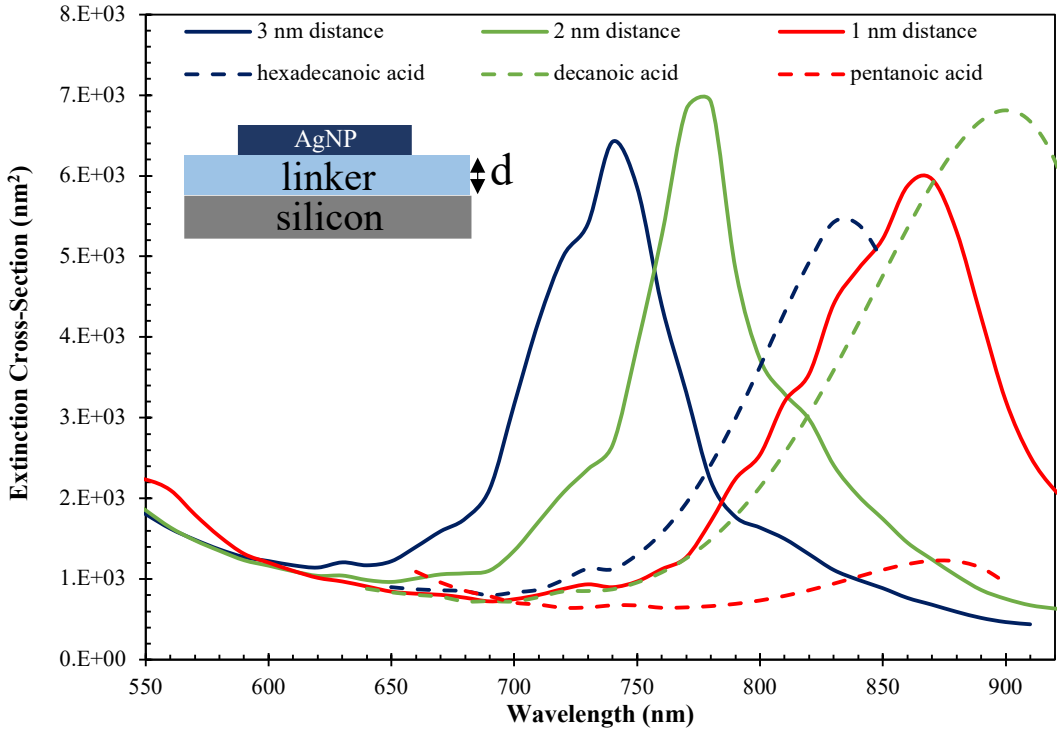

Figure 3.13: Extinction cross-section spectra comparing nanoparticle-to-silicon distance of 3 nm (blue), 2 nm (green) and 1 nm (red) to the corresponding linker molecule. Here, d is defined as the distance between the bottom of the nanoparticle and the top of the silicon slab where light blue slab corresponds to the linker molecule. Refractive index of the medium was air (n=1.0).

Figure 3.14 displays the electric field results of using the nanoparticle-to-silicon distance of 3 nm compared to having a 3 nm hexadecanoic acid layer in the space between the nanoparticle and silicon surface. Shown in Figure 3.14 is the front view (yz plane) of the nanoparticle on the silicon surface. The electric field enhancement shown in the vicinity of the nanoparticle and silicon surface did not decrease with the hexadecanoic acid layer.

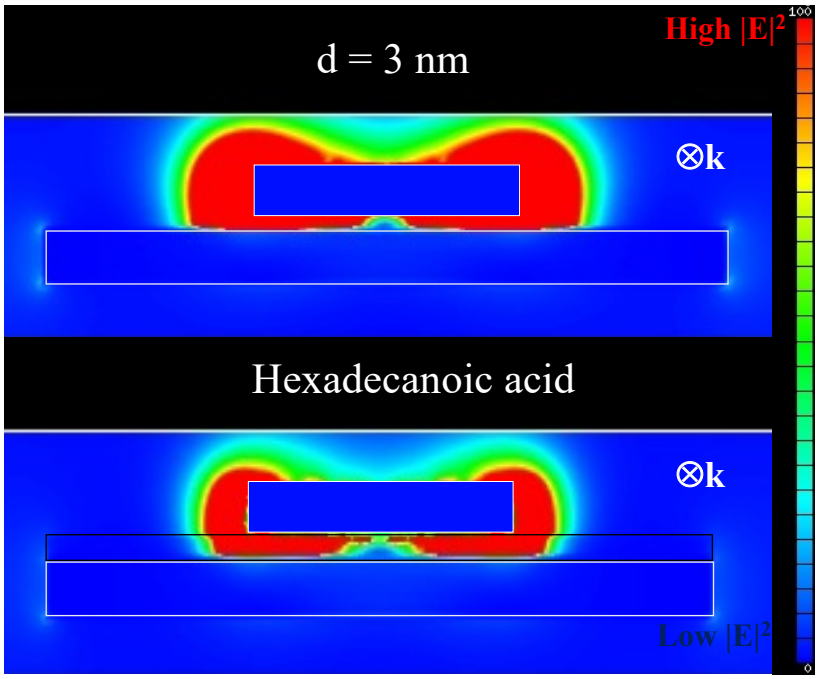

Figure 3.14: Calculated $|E|^2$ field contours for a nanoparticle-to-silicon surface distance of 3 nm (top) compared to a hexadecanoic layer(bottom). The silicon surface is outlined while the location of the AgNP is shown as a blue rectangle.

From these results, we concluded that the addition of the linker molecule layer to the nanoparticle and silicon spacing would not have negative effects on the extinction of the silver nanoparticles.

3.9 Conclusion

In conclusion, using the DDA computational simulations as implemented in the DDSCAT program, we determined that linker molecules with lengths in the range from 1 to 5 nm would provide the highest electric field enhancement, with smaller linker molecules preferred. Also, these calculations provided an insight as to why having a linker molecule could be essential in enhancing the photoefficiency of thin solar cells compared to previous studies of adding silver nanoparticles directly onto solar cells. Ultimately modeling the interaction of silver nanoparticles on a silicon surface with the dielectric constant of some of the possible linker molecules with

their corresponding silicon-to-nanoparticle distance led to us to the conclusion that the electric field would not be negatively affected by these linker molecules.

3.10 References

1. Zhao, G.; Kozuka, H.; Yoko, T. Sol—Gel Preparation and Photoelectrochemical Properties of TiO2 Films Containing Au and Ag Metal Particles. *Thin Solid Films* **1996**, *277* (1–2), 147-154.

2. Tian, Y.; Tatsuma, T. Plasmon-Induced Photoelectrochemistry at Metal Nanoparticles Supported on Nanoporous TiO_2. *Chemical Communications* **2004**, *16*, 1810-1811.

3. Tian, Y.; Tatsuma, T. Mechanisms and Applications of Plasmon-Induced Charge Separation at TiO2Films Loaded with Gold Nanoparticles. *The Journal of the American Chemical Society* **2005**, *127* (20), 7632-7637.

4. Draine, B. T.; Flatau, P. J. Discrete-Dipole Approximation For Scattering Calculations. *The Journal of Optical Society of America A* **1994**, *11* (4), 1491-1499.

5. Purcell, E. M.; Pennypacker, C. R. Scattering and Absorption of Light by Nonspherical Dielectric Grains.*Astrophysical Journal*, **1973**, *186*, 705-714.

6 Sobh, A.; White, S.; Smith, J.; Sobh, N.; Jain, P. NanoDDSCAT+; nanoHUB, 2019.

7. Green, M. A. Self-Consistent Optical Parameters of Intrinsic Silicon at 300K Including Temperature Coefficients. *Solar Energy Materials and Solar Cells*, **2008**, *92* (11), 1305-1310.

8. Jiang, Y.; Pillai, S.; Green, M. A. Realistic Silver Optical Constants for Plasmonics. *Scientific Reports*, **2016**, *6* (1), 30605

9. Hao, E.; Schatz, G. C. Electromagnetic Fields around Silver Nanoparticles and Dimers. *The Journal of Chemical Physics* **2004**, *120* (1), 357-366.

10. Larranaga, M. D.; Lewis, S. R. J.; Lewis, R. In Hawley's Condensed Chemical Dictionary; John Wiley & Sons: Hoboken, New Jersey, 2016; pp 1027.

11. Lide, D. R. In CRC Handbook of Chemistry and Physics; CRC: Boca Raton, Florida, 2005; 3134.

12. Merck. In The Merck index: an Encyclopedia of Chemicals, Drugs, and Biologicals; Budavari, S., Heckelman, P. E., Smith, A., O'Neil, M. J., Eds.; The Royal Society of Chemistry: Cambridge, UK, 2013; 1764.

Chapter 4

Modifying Silicon Surfaces with Silver Nanoparticles

4.1 Introduction

We began by working with silicon (100) wafers, whose surfaces are well-defined, before using thin silicon solar cells. The general procedure involved the etching and hydrogenation of the silicon surface, followed by the binding of a bifunctional linker molecule, and the final step was attachment of the synthesized silver nanoparticles (AgNPs). There were several methods in the literature that we explored to attach organic molecules onto the silicon surfaces. Some of these methods involved the use of silanes[1], carbonyls,[2] and N-Bromosuccinimide-based bromination.[3] Our search of the literature led us to using terminal alkenes and UV light as the reaction starter since this method proved to be relatively simple and successful in creating uniform layers. Ultimately, the method of Cicero *et al* [4] was chosen because we could easily replicate it using our laboratory equipment.

Once we selected the method to attach organic molecules onto silicon, we had to decide

which particular linker molecules to use. Since we were using the procedure of Cicero *et al* one of the requirements was a terminal alkene because the terminal double bond is essential to binding to the silicon surface. The other requirement for the linker molecule is a terminal amine, thiol, or carboxylate group on the other end that would bind to the AgNPs. Attachment of the linker molecules to the silicon was done by immersing the wafers into a solution of the linker molecules and exposing the system to ultraviolet light. A possible mechanism of attachment will be described in the Discussion section(4.5.4). To test the attachment process before attaching the desired linker molecule, a trial molecule of 1-octadecene was used according to the method of Cicero *et al*. The binding of the trial linker molecule to silicon was confirmed by contact angle measurements and attenuated total reflectance Fourier transform infrared (ATR-FTIR) spectroscopy. Contact angle measurements involve measuring the contact angle between a droplet of water and the surface. This is a semi-quantitative method which determines the hydrophobicity of the surface, a property that is expected to change during the various steps of processing the silicon. ATR-FTIR is a quantitative method that enables identification of the actual compounds bound to the surface. Both analytical methods will be explained in more detail in the following section.

Once the binding of the trial linker molecule to silicon was confirmed, two different linker molecules were investigated: allylamine and undecylenic acid. Figure 4.1 shows these linker molecules.

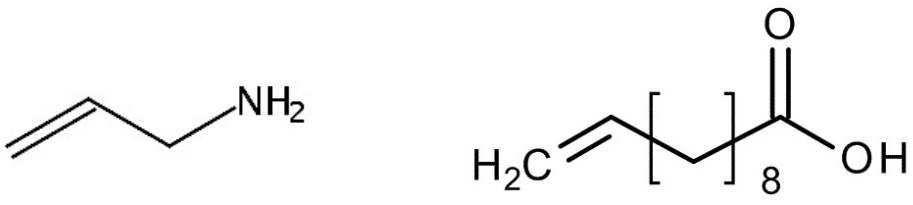

Figure 4.1: The chemical structures of allylamine (left) and undecylenic acid (right) linker molecules.

As with the test linker molecule, the attachment of the linker molecules in Figure 4.1 onto the silicon surface was monitored using contact angle measurements and ATR-FTIR.

4.2 Contact Angle Measurement

The contact angle between a liquid droplet and a surface gives a simple indication of the interfacial forces. If the liquid is water, the contact angle is determined by the hydrophobicity of the surface. The contact angle is defined such that the larger the value, the more hydrophobic the surface, while the smaller the value, the more hydrophilic the value as illustrated in Figure 4.2. In other words, less wetting of the surface indicates that it has less contact with the water droplet and thus is more hydrophobic. To do this measurement, the sample was placed in a homemade apparatus that consists of a flat, horizontal stage (a Newport optical mirror mount) situated directly in front of a computer-controlled digital microscope (Dino-Lite, model AM4111T). To allow proper alignment of the sample and microscope, the mirror mount has two angular degrees of freedom and can be translated vertically, and the microscope is mounted on a 3-dimensional translation stage. The sample is illuminated from the backside by a white LED. A 20 μL droplet of DI water is pipetted onto the surface, the system is aligned manually, and the microscope is focused on the droplet. A picture is then taken of the droplet for subsequent analysis. The angle of the water droplet to surface can be measured either in the Dino-Lite software or in other standard graphics software packages. Figure 4.2 shows the set-up and illustrates the shape of a water droplet and the contact angle for a hydrophobic surface compared to a hydrophilic surface. We measured contact angles before and after each stage of attaching the linker molecules and nanoparticles.

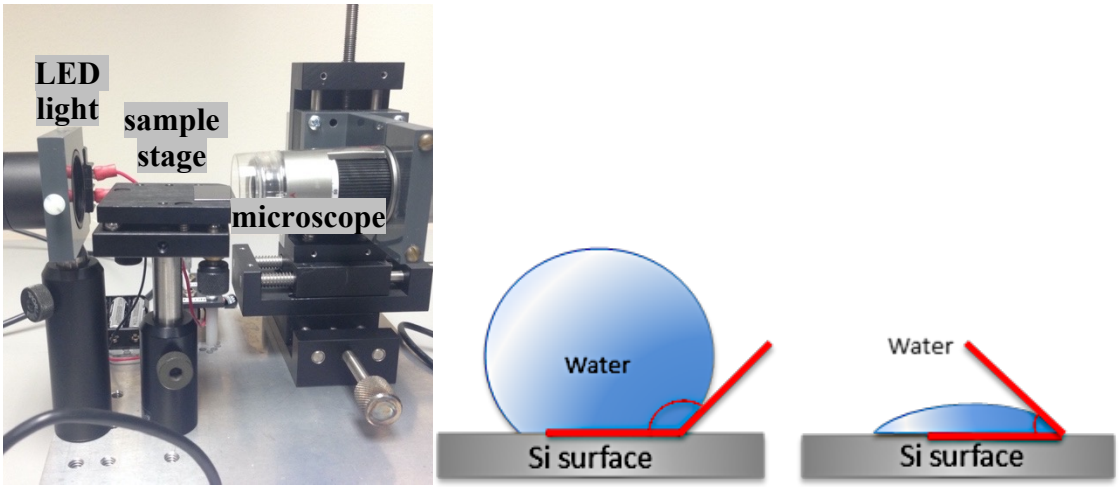

Figure 4.2: Pullman Lab contact angle apparatus (left). The contact angle of a hydrophobic (middle) and of a hydrophilic (right) surface.

4.3 Attenuated Total Reflectance Fourier Transform Infrared Spectroscopy

Attenuated Total Reflectance Fourier Transform Infrared Spectroscopy (ATR-FTIR) is a technique capable of measuring the infrared absorption spectrum of species bound to a surface.[5] The spectrum enables the chemical bonds to be determined, which in turn provides information about the identity and possibly the orientation of the surface-bound species. A schematic diagram of the sample cell in an ATR-FTIR spectrometer[6] is shown in Figure 4.3. The instrument operates by measuring the changes that occur in a totally internally reflected infrared beam when the beam comes into contact with a sample. An infrared beam is directed onto the surface of a high refractive index crystal (the ATR crystal) at an angle such that total internal reflection occurs. This internal reflectance creates an evanescent wave that extends beyond the surface of the crystal into the sample held in contact with the crystal. For this measurement, we use a germanium crystal because it has the highest refractive index of all the ATR materials available, which in turn means that the effective depth of penetration into the sample is approximately 1 micron.[7] Due to

the thin linker molecule layers (0.5-5 nm) on the surfaces, obtaining spectra with peaks that were sufficiently intense and well resolved was a challenge. To help with the resolution of the peaks, we used a clean silicon wafer for the background spectra.

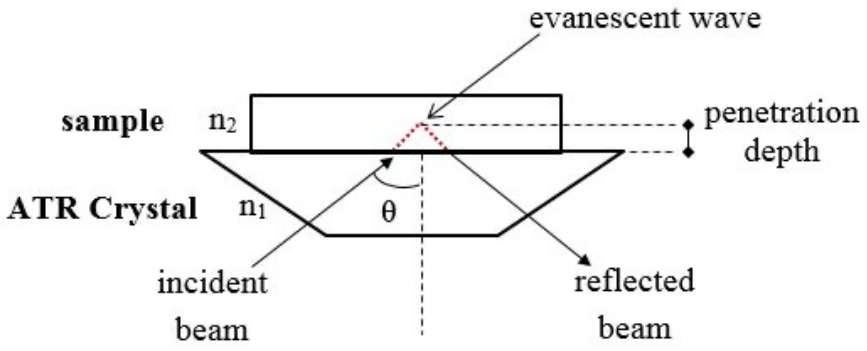

Figure 4.3: ATR-FTIR schematic diagram. n_1 and n_2 are the indices of refraction of the ATR crystal and of the sample.

4.4 Etching/ Hydrogenation of Silicon

To attach the linker molecule to the silicon surface, the first step was to etch and hydrogenate the silicon surface with hydrofluoric acid. The purpose of doing this was to make the surface reactive to the alkene in the presence of UV light.

4.4.1 Materials and Preparation

48 to 52% hydrofluoric acid was purchased from Acros Organics. Silicon crystals with a resistivity of 1-30 Ω cm, a thickness of 290-310 μm, and an orientation of (1 0 0) were purchased from Ultrasil. A 10% w/w solution of hydrofluoric was prepared in a PFA container by diluting 5.0 ml of hydrofluoric acid in 23.0 ml of DI water. PFA was used for the container material due to the corrosiveness of hydrofluoric acid toward glass. The silicon crystal was cut into rectangles that were 1.5 cm in width by 4.5 cm in length using a diamond scribe. Once cut, the silicon rectangles were cleaned using trichloroethylene, acetone, and methanol by rinsing for 3 minutes

each and rinsed with DI water at the end.

4.4.2 Experimental Procedure

After the silicon wafers were cleaned and air dried, they were etched using the 10% hydrofluoric acid solution. The etching process involved dipping the cleaned wafer into the 10% hydrofluoric acid solution for 2 minutes, then rinsing in DI water multiple times and air drying.

4.4.3 Results

As mentioned before, the hydrogenation of the silicon surface was monitored using two analytical methods: contact angle measurements and ATR-FTIR spectroscopy. The results of both methods are shown below. In Figure 4.4, the first image (left) shows the contact angle for a water droplet on a clean silicon wafer. From the small angle of 17 degrees, we determined that it was a hydrophilic surface. The next image (right) shows the same silicon wafer after it was etched. Figure 4.5 shows the ATR-FTIR spectrum of an etched silicon wafer.

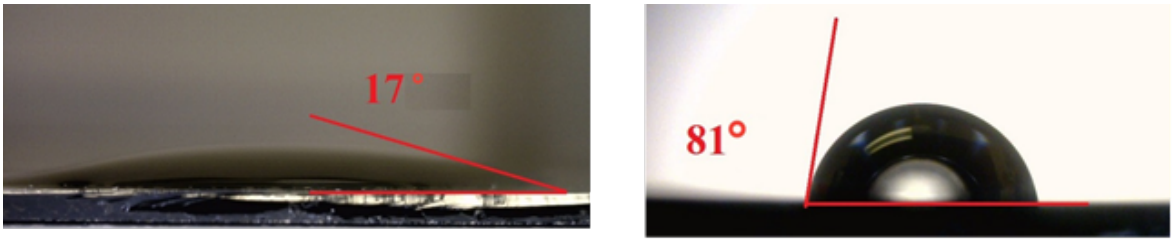

Figure 4.4: Contact angle of a water droplet on a clean silicon wafer (left) and etched silicon wafer (right).

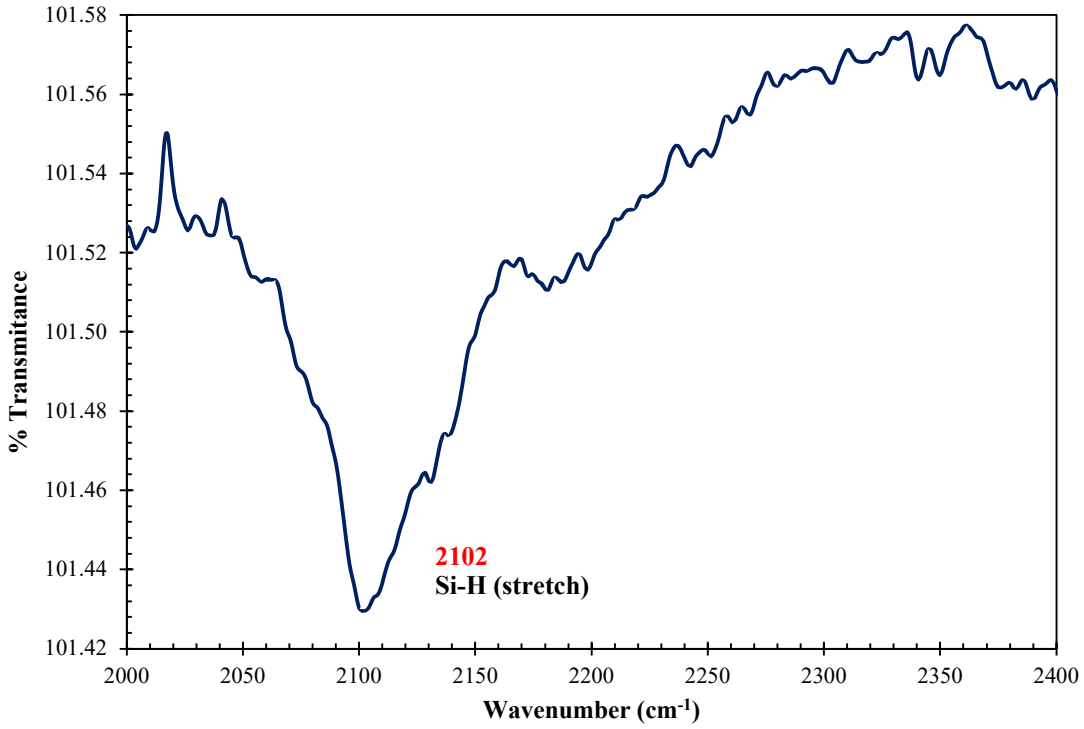

Figure 4.5: ATR-FTIR spectrum of the silicon hydride stretch region of a silicon wafer etched for 10 minutes in 10% hydrofluoric acid.

4.4.4 Discussion

The surface of a clean silicon wafer has Si-O and Si-OH bonds, and after it is etched by HF, they are replaced by Si-H bonds. This reaction is widely used, but the formation of Si-H bonds instead of Si-F bonds is in fact surprising because Si-F bonds are significantly stronger than Si-H bonds (140 kcal mole^{-1} vs. 76 kcal mol^{-1}).[8] One possible mechanism, described by Higashi and Chabal[9] of how the silicon surface is hydrogenated, is shown in Figure 4.6. The first step is the formation of a hydrogen bond involving the hydrofluoric acid molecule and the silicon oxide surface. Then water leaves, leaving a Si-F bond that then attracts another hydrofluoric acid molecule due to the partial charges on silicon and fluoride. In the final step, the silicon difluoride species desorbs, leaving behind the Si-H bond on the surface.

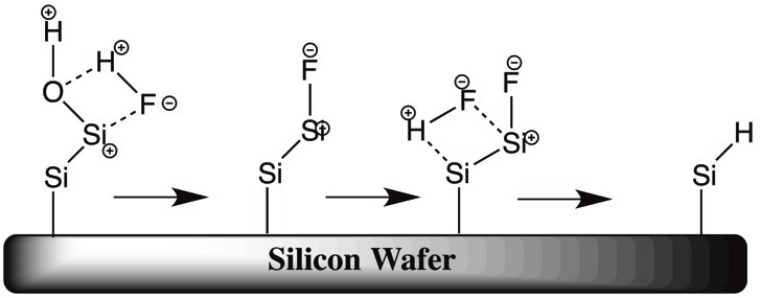

Figure 4.6: A schematic of the hydrogenation mechanism of a silicon wafer by Higashi and Chabal.[9]

In our work, evidence for the formation of Si-H bonds comes from the contact angle measurements of the etched silicon as shown in Figure 4.4. The difference in contact angle from 17° on a clean silicon wafer to 81° on an etched silicon wafer led us to conclude that the surface changed from hydrophilic to hydrophobic. This is expected because the Si-H bond is non-polar (electronegativity is 2.4 for silicon and 2.1 for hydrogen) compared to Si-OH, which is a polar bond (electronegativity of oxygen is 3.5). Additionally, consistent with the contact angle results is the ATR-FTIR spectrum in Figure 4.5 which shows a peak at 2102 cm^{-1}. This peak is indicative of the Si-H bond-stretching mode.[10] We were unable to see the other Si-H peak at 630 cm^{-1} corresponding to the bending mode due to the spectral range limitations of the germanium ATR-FTIR crystal (cutoff is 780 cm^{-1}). Once the silicon surface was hydrogenated, the next step was to attach the linker molecule.

4.5 Attachment of Linker Molecules

The chosen linker molecules had two main properties: a terminal double bond that was essential for binding to the silicon surface and an amine or carboxylate group that has an affinity towards silver. Before we tried the linker molecules, we used 1-octadecene as a trial molecule to test our method. 1-octadecece has a terminal double bond and has been attached to silicon surfaces before as described by Cicero *et al*.[4] Using their procedure, we attached the 1-octadecene

molecule to a silicon surface. Once we confirmed that we attached this trial molecule, we went on to attach the chosen linker molecules. The actual process of how we did this is illustrated in this section.

4.5.1 Materials and Preparation

1-octadecene, undecylenic acid, allylamine were all purchased from Sigma Aldrich. 10% (v/v) solutions of these compounds were made using acetonitrile as the solvent. Allylamine was stored in a glove box due to its potential for hazardous polymerization.

4.5.2 Experimental Procedure

To start the reaction, the hydrogenated surface was submerged in a quartz vial containing a 10% (v/v) solution of the linker molecule. Acetonitrile was used as the solvent and quartz as the vial material since they do not absorb in the ultraviolet region above 200 nm. The UV photochemical reactor was built in-house and used a small 12V UV-C 254 nm germicidal lamp as the irradiation source (Figure 4.7). The silicon wafer (1.5 cm in width by 4.5 cm in length) rested on a Teflon ring that enabled a magnetic stir bar to mix the solution without striking the wafer. While being stirred, the solution with the silicon wafer was exposed to the 254 nm UV light for 60 minutes to 90 minutes. After the silicon wafer was reacted with the linker molecule, it was rinsed in tetrahydrofuran (THF) for 4 minutes following the same procedure as Yamada *et al.*[11] and placed in the oven (150 °C) to dry for 4 minutes.

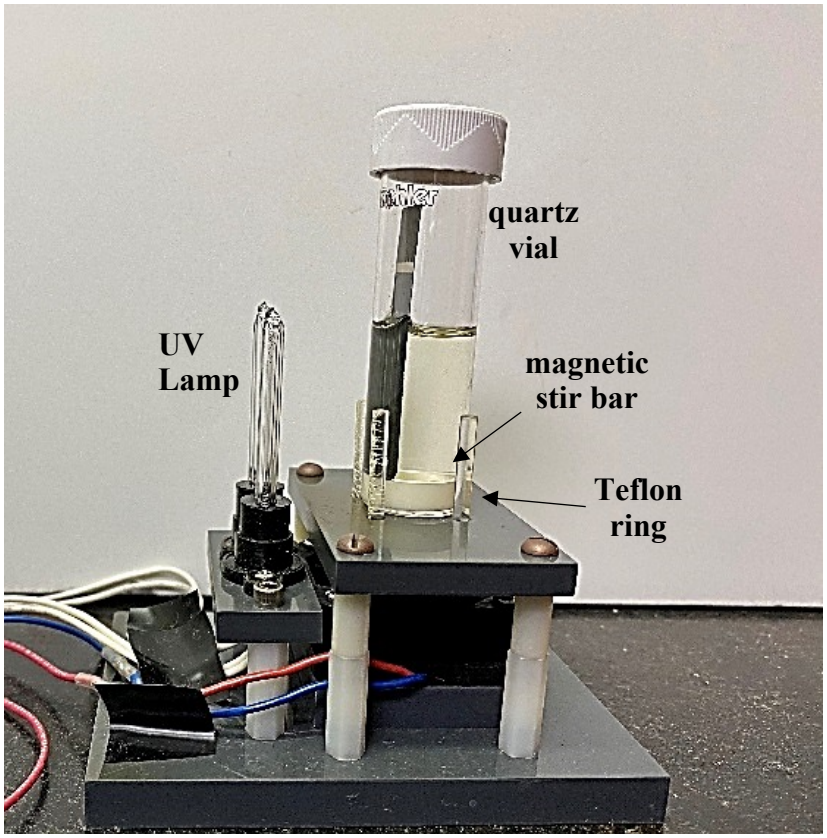

Figure 4.7: In-house UV photochemical reactor made using a germicidal lamp.

4.5.3 Results

The functionalization of the silicon surface with linker molecules was monitored using contact angle measurements and ATR-FTIR spectroscopy. The results of both methods are shown in Figures 4.8 and 4.9.

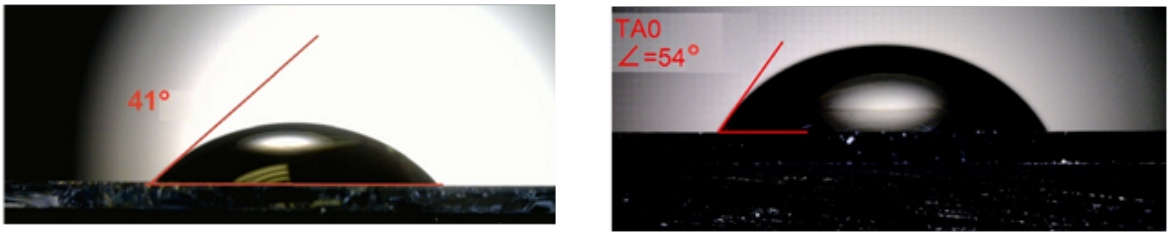

Figure 4.8: Contact angle of a water droplet on an allylamine terminated silicon surface (left) and an undecylenic acid terminated silicon surface (right).

The left panel of Figure 4.8 shows the contact angle of a water droplet on the silicon surface terminated with allylamine. The reduction from 81 degrees in the Si-H case (Figure 4.4) to an angle of 41 degrees demonstrates that the Si-H surface has been converted to a more polar surface, as one would expect if allylamine, with its polar amine group, now terminates the surface. However, there are also C-H bonds in the linker molecule, perhaps explaining why the angle is not as low as in the case of the clean silicon surface. The right panel in Figure 4.8 shows the contact angle after adding the undecylenic acid linker molecule. The contact angle of 54 degrees corresponds to a surface that is hydrophilic due to the polar end of the carboxylic acid but since there are many C-H bonds, one can expect this angle to be larger than for allylamine. The value of 54 degrees is comparable to the contact angle of 58 degrees found by Coffinier *et al.*[12]

The next method to determine monolayer identities bonded to the silicon surface was ATR-FTIR spectroscopy. Figure 4.9 shows the ATR-FTIR spectrum of the silicon wafer modified with the allylamine linker compared with neat allylamine. Both spectra show percent transmittance as a function of wavenumber. For the neat allylamine spectrum, air was used as background whereas for the silicon wafer modified with allylamine linker, a clean silicon wafer was used as the background to get resolved peaks of the attached linker molecule. Comparing the spectra, both show the N-H stretch along with sp^3 C-H stretches. The wavenumbers of both stretches are comparable to those found by Yamada *et al*. Notably, the Si-allylamine spectrum is missing the alkene sp^2 C-H stretch found above 3000 cm^{-1} that is observed in the neat spectrum. Only alkenes and aromatics show sp^2 C-H stretches above 3000 cm^{-1}, this result is consistent with the linker molecule attaching to the surface via the formation of the Si-C bond.

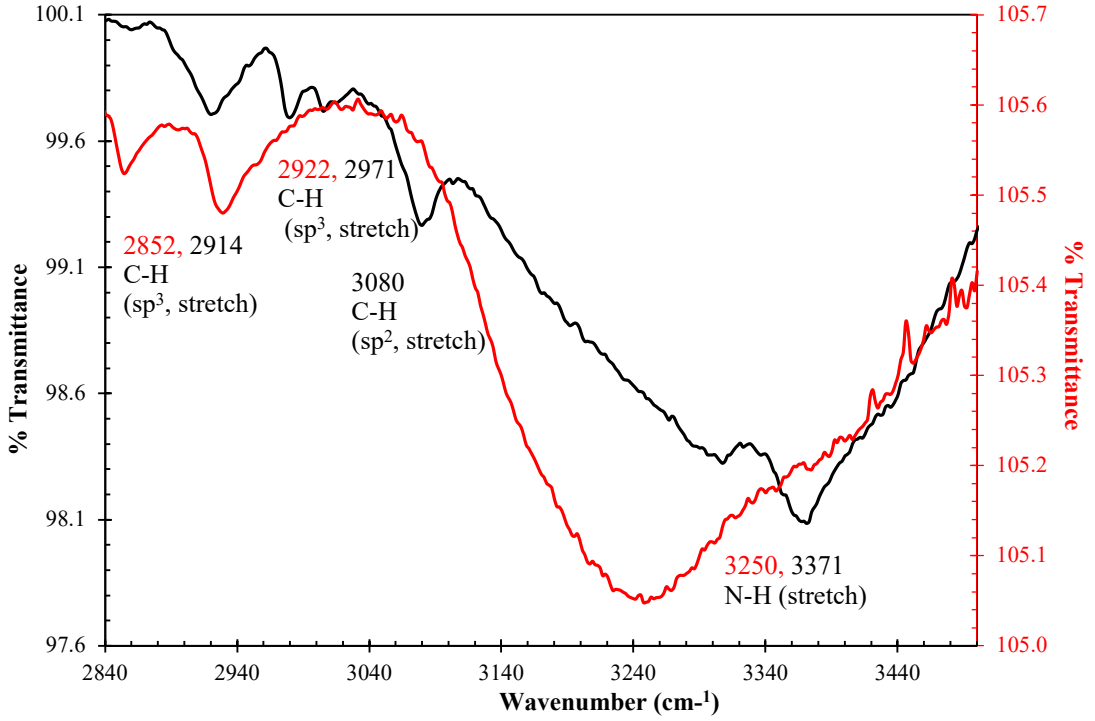

Figure 4.9: ATR-FTIR spectra of allylamine neat (black) and allylamine modified silicon wafer (red).

Figure 4.10 compares the ATR-FTIR spectrum of the silicon wafer modified with undecylenic acid linker to undecylenic acid neat. Both spectra show the alkane sp^3 C-H stretches, along with the carbonyl stretch. In contrast, the alkene C=C stretches along with the C=C bending were missing from the silicon wafer modified with undecylenic acid linker spectrum. This is anticipated, as explained in the next section. Also, the spectrum of the silicon wafer modified with undecylenic acid shows the emergence of a strong peak at 1278 cm^{-1}, which may be due to the Si-C stretch, although it could also have a contribution from undecylenic acid's C-O stretch, which appears at 1285 cm^{-1} in neat undecylenic acid. The values of the stretches were comparable to the values reported in the literature by Voicu *et al.*[13] The missing C=C peaks and appearance of the strong 1278 cm^{-1} peak are consistent with the linker molecule attaching to the surface via the alkene. From this information, we concluded that the linker molecules could be attached to the silicon surface. The attachment mechanism of how this occurs will be discussed in detail in the

following section.

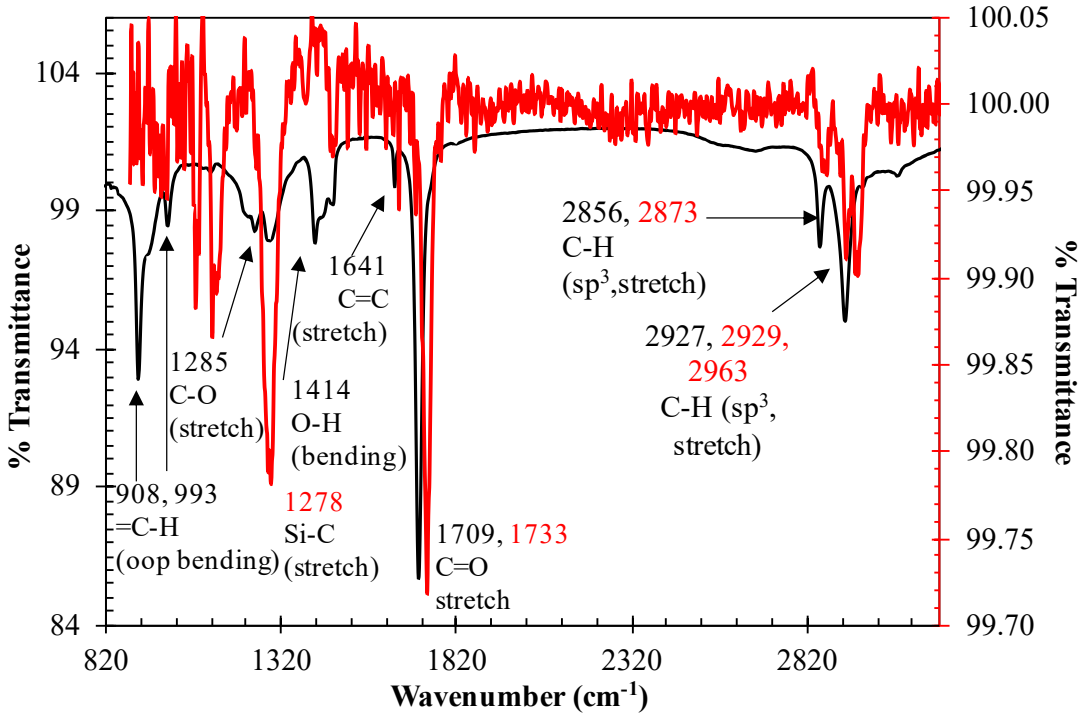

Figure 4.10: ATR-FTIR spectra of undecylenic acid neat (black) and undecylenic acid modified silicon wafer (red).

4.5.4 Discussion

The proposed mechanism of how allylamine attaches to the silicon surface is shown in Figure 4.11. The same mechanism likely operates in the case of undecylenic acid. This closely follows the proposed pathway by Cicero *et al.*[14] of how a terminal alkene linker molecule passivates a silicon surface. The first step is the formation of a silicon radical when the solution is exposed to UV light. This silicon radical then attacks the terminal alkene of the linker molecule, forming a more stable radical. Next, due to the proximity of hydrogens on nearby Si-H bonds, the silicon radical attacks a hydrogen, thus forming another silicon radical. The radical propagation continues until the entire surface has been covered with the linker molecule, in this case allylamine. The result is a silicon surface covered with a linker molecule.

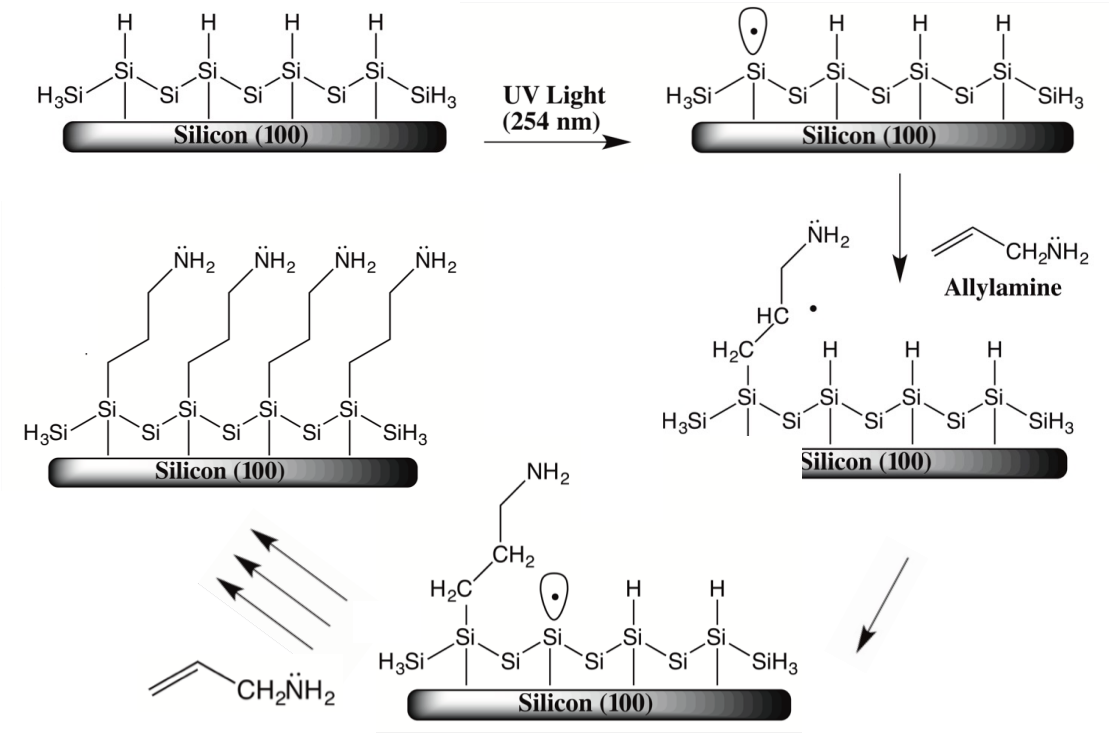

Figure 4.11: Possible mechanism for the functionalization of silicon wafer with allylamine that closely follows the proposed pathway by Cicero *et al.*[14]

As shown in this mechanism, there are two key factors in the successful attachment of the linker molecule to the silicon surface: a complete hydrogenated silicon surface and excess terminal alkene linker molecule. The contact angle measurement helped us determine whether the silicon surface was saturated with Si-H bonds. To ensure excess linker molecule, the reaction was run using a 10% (v/v) linker molecule solution.

4.6 Attachment of Silver Nanoparticles to Linker Molecule

4.6.1 Materials and Preparation

The nanoparticles that were used to bind to the modified silicon surface were triangular AgNPs prepared by the borohydride-reduction/peroxide-oxidation method described in Chapter

2. As mentioned there, this method is fast and provides nanoparticles that absorb in the desired region between 600 nm to 1100 nm.

4.6.2 Experimental Procedure

The AgNPs were attached to the functionalized silicon surface by submerging the functionalized silicon surface into the aqueous AgNPs solution. To ensure that there were enough AgNPs that covered the modified silicon surface, we calculated the total nanoparticle surface area. We did this by making a few assumptions. First, we used the average size of the triangular nanoparticles of 50 nm in edge length. Assuming a thickness of 7 nm (determined by TEM) and edge length of 50 nm, each triangular nanoparticle would have 4.5 x 10^5 Ag atoms. A vial of 20 mL of nanoparticle solution contains about 2.7 x 10^{19} Ag atoms using the concentration of 0.1 M $AgNO_3$ and the amount added of 444 μL of $AgNO_3$. Therefore, assuming all the nanoparticles were 50 nm in edge length and 7 nm in thickness, there should be 6.0 x 10^{13} triangular nanoparticles per 20 ml vial. The surface area (area of a flat face) of each triangular nanoparticle was 1.08 x 10^3 nm^2 giving a total nanoparticle surface area of 6.5 x 10^{16} nm^2. This total nanoparticle surface area should be enough to cover each silicon wafer, which has an area of 6.8 x 10^{14} nm^2.

The procedure was to use a 20 mL glass vial containing the triangular AgNPs solution and submerge the functionalized silicon surface in it. The functionalized silicon surface was submerged multiple times in 15-minute increments. After each 15-minute increment, the surface was cleaned using running deionized (DI) water multiple times to rinse off loosely bound nanoparticles and ensure that the remaining nanoparticles were strongly bound to the surface. Once the surface was cleaned, a UV-Visible scattering spectrum was taken. From this procedure, we determined that after 90 minutes of submersion, there was no change in the scattering of the surface. Consequently, the remaining experiments used 90 minutes of submersion in the AgNPs solution. Figure 4.12 schematically shows the bound nanoparticles of an allylamine modified

silicon wafer.

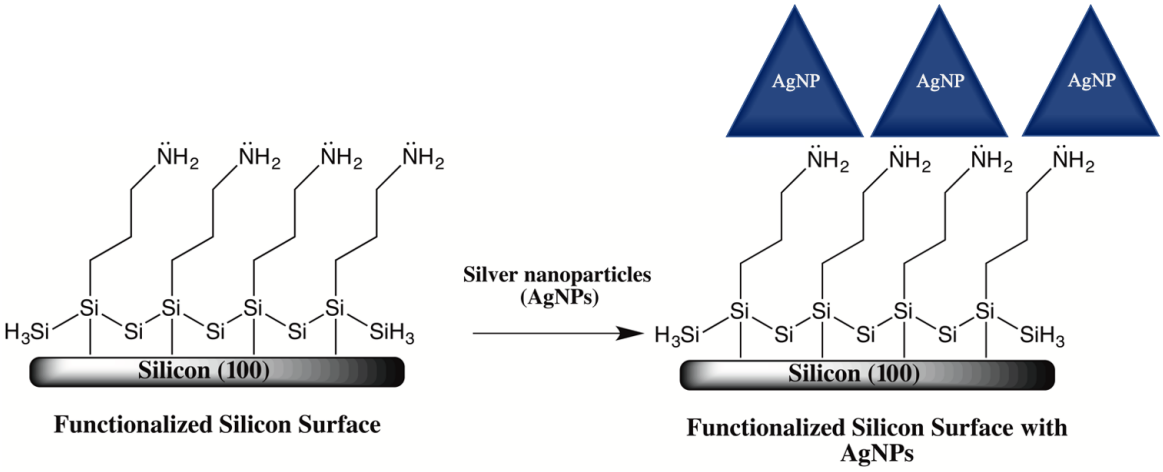

Figure 4.12: Schematic of an allylamine modified silicon wafer exposed to blue AgNPs. Shown is the reaction before and after the AgNPs were bound to the surface.

To determine that the nanoparticles were bound to the linker molecule, we used a method called UV-Visible scattering spectroscopy. This was done after the AgNPs were attached to the linker molecule to determine the amount of scattering. How this works is by having a simple set-up where the sample is exposed to a broadband UV-Visible light source (a homemade xenon lamp) and then detecting the backscattered light with a CCD array (Stellarnet, model Black Comet). A dark spectrum is taken before the sample is added, and then a reference spectrum is taken of a clean silicon surface before the sample is analyzed. A schematic diagram of this type of spectroscopy is shown in Figure 4.13. To compare the scattering of nanoparticles bound to the linker-modified silicon surface, we took scattering spectra of AgNPs solution using a fluorometer. The comparison of these spectra is shown in the next section.

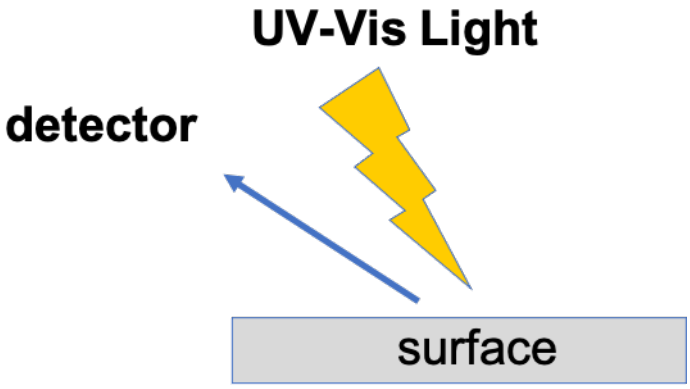

Figure 4.13: Schematic of the simple set-up UV-Visible scattering spectroscopy. Shown is a surface being exposed to UV-Visible light.

4.6.3 Results and Discussion

Figure 4.14 shows the scattering spectrum of a modified silicon wafer with the allylamine and AgNPs (green) along with an unmodified silicon wafer (gray). Both spectra are plotted as the log of the ratio of intensity of the sample to the intensity of the reference, as a function of the wavelength.

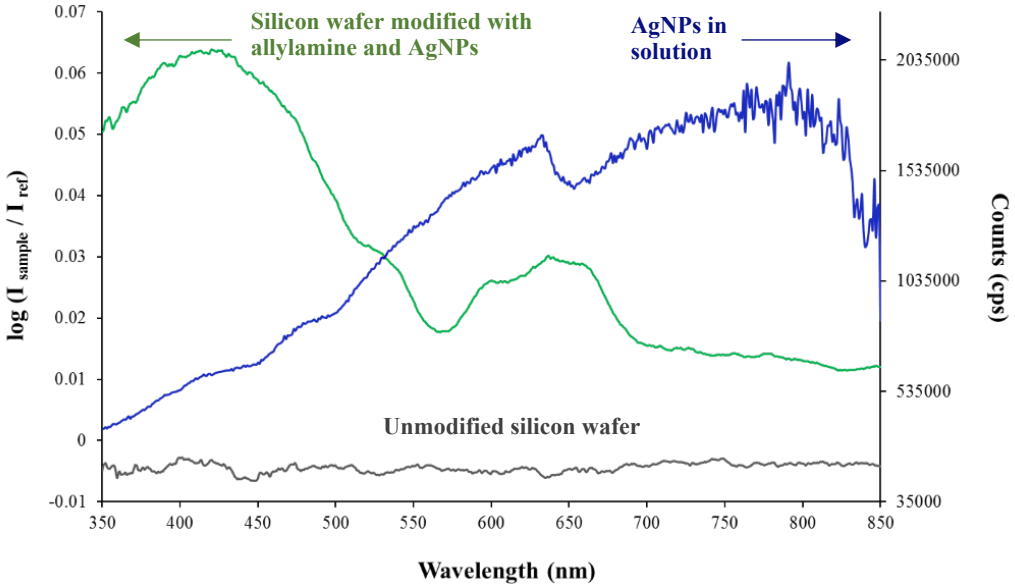

Figure 4.14: UV-Visible scattering spectra of allylamine modified silicon wafer with attached AgNPs (green), AgNPs in solution (blue), and an unmodified silicon wafer (gray). The arrows show the corresponding y-axis of the silicon modified wafer and with AgNPs and AgNPs in solution

Figure 4.14 also shows the scattering spectrum of the AgNPs (blue) in solution (as a point of reference, the corresponding UV-visible absorption spectrum is shown in Figure 2.1). This was done to compare the expected scattering. Note that this spectrum has a different y-axis, with units of counts, and is shown to the right. The largest peak in the spectrum of the modified silicon wafer occurs near 400 nm while the peak for the solution-phase AgNPs peaks near 780 nm. This difference in scattering spectra was unexpected. One possible explanation why we were detecting a higher amount scattering from the modified wafer at the 400 nm region instead of the 780 region is that perhaps smaller silver nanoparticles were preferentially binding instead of larger nanoparticles. Another possible explanation has to do with the vertical selection rule, in which only dipole resonances that are perpendicular to the surface will be excited. For resonances parallel to the surface (left part of Figure 4.15), the induced dipole moments of the nanoparticle and the image charges cancel out. For resonances perpendicular to the surface (right part of Figure 4.15), the induced dipole moments add and give a net scattering signal. This is illustrated

in the schematic diagram in Figure 4.15.

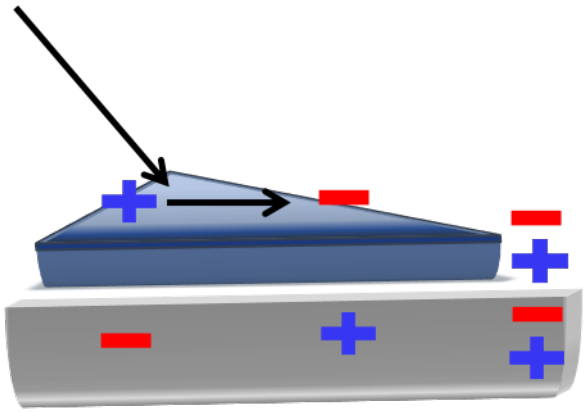

Figure 4.15: Schematic diagram illustrating the vertical selection rule of triangular nanoparticle on a silicon surface.

In conclusion, the goal of using linker molecules to attach AgNPs to silicon surfaces was accomplished. This was verified using the analytical methods of ATR-FTIR, contact angle and UV-Visible scattering spectroscopy. Once this was done, the next step was to repeat the process using thin silicon solar cells.

4.7 References

1. Maboudian, R.; Ashurst, W. R.; Carraro, C. Self-Assembled Monolayers as Anti-Stiction Coatings for MEMS: Characteristics and Recent Developments. *Sensors and Actuators A: Physical* **2000**, *82* (1-3), 219-223.

2. Armstrong, J. L.; White, J. M.; Langell, M. Thermal Decomposition Reactions of Acetaldehyde and Acetone on Si (100). *Journal of Vacuum Science & Technology A: Vacuum, Surfaces, and Films* **1997**, *15* (3), 1146–1154.

3. Bell, J. P.; Cloud, J. E.; Cheng, J.; Ngo, C.; Kodambaka, S.; Sellinger, A.; Ratanathanawongs Williams, S. K.; Yang, Y. N-Bromosuccinimide-Based Bromination and Subsequent Functionalization of Hydrogen-Terminated Silicon Quantum Dots. *RSC Advances* **2014**, *4* (93), 51105-51110.

4. Cicero, R. L.; Linford, M. R.; Chidsey, C. E. D. Photoreactivity of Unsaturated Compounds with Hydrogen-Terminated Silicon (111). *Langmuir* **2000**, *16* (13), 5688-5695.

5. Atitar, M. F.; Belhadj, H.; Dillert, R.; Bahnem, D. W. *The Relevance of ATR-FTIR Spectroscopy in Semiconductor Photocatalysis. In Emerging Pollutants in the Environment - Current and Further Implications;* InTech, 2015.

6. Sarau, G.; Bochmann, A.; Lewandowska, R.; Christiansen, S. *From Micro- to Macro-Raman Spectroscopy: Solar Silicon for a Case Study;* INTECH Open Access Publisher, 2012.

7. Vigano, C.; Ruysschaert, J.; Goormaghtigh, E. Sensor Applications of Attenuated Total Reflection Infrared Spectroscopy. *Talanta* **2005**, *65* (5), 1132-1142.

8. Lippert, E. The Strengths of Chemical Bonds, von T. L. Cottrell. Butterworths Publications Ltd., London 1958. 2. Aufl., X, 317 S., geb.t-32-. *Angewandte Chemie* **1960**, *72* (16), 602-602.

9. Higashi, G. S.; Chabal, Y. J.; Trucks, G. W.; Raghavachari, K. Ideal Hydrogen Termination of the Si (111) Surface. *Applied Physics Letters* **1990**, *56* (7), 656-658.

10. Lucovsky, G.; Nemanich, R. J.; Knights, J. C. Structural Interpretation of the Vibrational Spectra Ofa-Si: H Alloys. *Physical Review B* **1979**, *19* (4), 2064-2073.

11. Yamada, T.; Noto, M.; Shirasaka, K.; Kato, H. S.; Kawai, M. Photoassisted Adsorption of Allylamine and 1-Butene on H:Si(111) Studied by Surface Vibrational Spectroscopies. *The Journal of Physical Chemistry B* **2006**, *110* (13), 6740-6749.

12. Coffinier, Y.; Piret, G.; Das, M. R.; Boukherroub, R. Effect of Surface Roughness and Chemical Composition on the Wetting Properties of Silicon-Based Substrates. *Comptes Rendus Chimie* **2013**, *16* (1), 65-72.

13. Voicu, R.; Boukherroub, R.; Bartzoka, V.; Ward, T.; Wojtyk, J. T. C.; Wayner, D. D. M. Formation, Characterization, and Chemistry of Undecanoic Acid-Terminated Silicon Surfaces: Patterning and Immobilization of DNA. *Langmuir* **2004**, *20* (26), 11713-11720.

14. Cicero, R. L.; Chidsey, C. E. D.; Lopinski, G. P.; Wayner, D. D. M.; Wolkow, R. A. Olefin Additions on H-Si (111): Evidence for a Surface Chain Reaction Initiated at Isolated Dangling Bonds. *Langmuir* **2002**, *18* (2), 305-307.

Chapter 5

Modifying Solar Cell Surfaces with Silver Nanoparticles

5.1 Introduction

After we successfully modified the silicon surfaces with AgNPs, we moved on to solar cells. Solar cells, specifically thin film silicon solar cells, have been a research topic of interest in the last decade because they are inexpensive and have attractive properties, such as being lightweight and the ability to be flexible. An issue with thin film silicon solar cells, however, is that their absorption coefficient for light in the near-infrared (near-IR) region between 700 to 1100 nm decreases by a factor of 500.[1]

The goal of the work presented in this chapter, was to enhance the photoefficiency of thin silicon solar cells, especially in the near-infrared region of the solar spectrum, by sensitizing them with silver nanoparticles that are chemically attached to their surface. This was done by attaching linker molecules of varying lengths to the solar cell surface that had an affinity towards AgNPs. The varying lengths of linkers molecules was the key to tuning the optimal distance

between AgNP and silicon surface. In Chapter 3, we used computational simulations to model the electric field enhancement of this linker-to-nanoparticle distance. Using the results from these computational simulations, we determined that linker molecules in the range from 1 to 5 nm would provide the highest electric field enhancement. To attach the linker molecules to the solar cells we used the method of Cicero *et al.*[2] described in Chapter 4. Finally, to bind the AgNPs to the modified thin silicon solar surface we also use the procedure outlined in Chapter 4.

We began by selecting the linker molecules. To be able to use the procedure outlined by Cicero *et al.*, the linker molecules needed a terminal double bond essential to binding to the silicon surface (in our case the solar silicon surface). The other requirement was terminal amine, thiol, or carboxylic group that would bind to the AgNPs. Using this information as our guideline, we selected linker molecules that meet these requirements while also had carbon chains that vary in size. The linker molecules we used were: allylamine, 4-pentenoic acid, 5-hexenoic acid and undecylenic acid. Also, these linker molecules were within the range of 1-5 nm following the results from Chapter 3.

In Chapter 4, we demonstrated how to successfully attach linker molecules to a silicon surface. The analytical methods we used to determine how successful we were at attaching the liker molecules were: ATR-FTIR spectroscopy and contact angle measurements. Both methods are described in detail in Chapter 4. However, due to the nature of thin silicon solar cells, they are very fragile and taking ATR-FTIR was not possible. Therefore, we were only able to use contact angle measurements to monitor the attachment of linker molecules to solar cells.

The general procedure of how the solar cells were modified is shown as a schematic in Figure 5.1. In this schematic, we used 4-pentanoic acid as the linker molecule. The first step to modify the solar cells, was to remove the antireflective coating that covers all solar cells. This was necessary to expose the silicon surface. As shown in Figure 5.1, we did this using hydrofluoric acid. The next step was to make the solar surface more reactive towards the linker molecule. The hydrofluoric acid was able to also make the surface more reactive and thus the removal of the

antireflective coating and increase hydrophobicity of the solar surface was done in one step. Once the reactivity of the solar cell was confirmed with contact angle measurement, the next step was to attach the linker molecule. This was accomplished by immersing the solar cell into a solution of the linker molecule and exposing this solution to UV light. After we determined the successful attachment of the linker molecule to the solar cell, the final step was to bind the AgNPs.

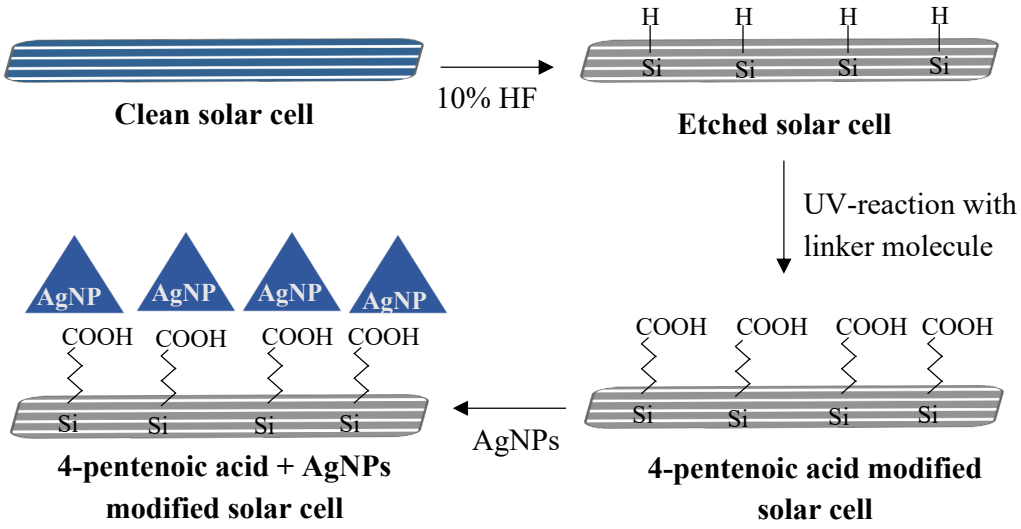

Figure 5.1: Scheme of general procedure of modifying thin silicon solar cells. Shown here is the linker molecule of 4-pentenoic acid being attached to the thin silicon solar cell surface.

The last part was to measure the efficiency of the modified solar cells. In the earliest stages of the project, we used a simple in-house apparatus that consisted of a light source (standard 60-Watt incandescent light bulb) that was placed above the modified solar cell, a voltmeter, and an ammeter to measure the voltage and current of the modified solar cell, and a variable resistor that allowed the load on the solar cell to be varied. Later, we upgraded this set-up by adding 1) a new lamp with a wavelength distribution and power similar to that of the sun, and a computer-controlled Arduino module that automatically varied the resistive load using two relays connected to various discrete resistors. The solar cell efficiency was determined using the photo conversion percentage and fill factor.

5.2 Etching/ Hydrogenation of Silicon Solar Cell

To attach the linker molecule to the thin silicon solar cell surface, the first step was to remove the anti-reflective coating that protects solar cells followed by etching/hydrogenation of the solar cell surface. This was done using hydrofluoric acid. The purpose of doing this was to ensure the solar surface was reactive towards the alkene end of the linker molecule in the presence of UV light. The process of how we accomplished this will be described in this section.

5.2.1 Materials and Preparation

48 to 52% hydrofluoric acid was purchased from Acros Organics. Thin silicon solar cells were purchased from ML Solar in Campbell, CA. A $\sim$10% (w/w) solution of hydrofluoric was prepared in a PFA container by diluting 5.0 ml of hydrofluoric acid in 23.0 ml of DI water. PFA was used for the container material due to the corrosiveness of hydrofluoric acid toward glass. The solar cells were cut into rectangles that were 1.5 cm in width by 4.5 cm in length using an in-lab set-up consisting of a fixed-position diamond blade (mounted in a high-speed Dremel rotary tool) that cuts solar cells firmly held in place on a 3-dimensional translational stage (Figure 5.2). Once cut, the solar cell rectangles were cleaned using trichloroethylene, acetone, and methanol by rinsing for 3 minutes each and then rinsed with DI water at the end.

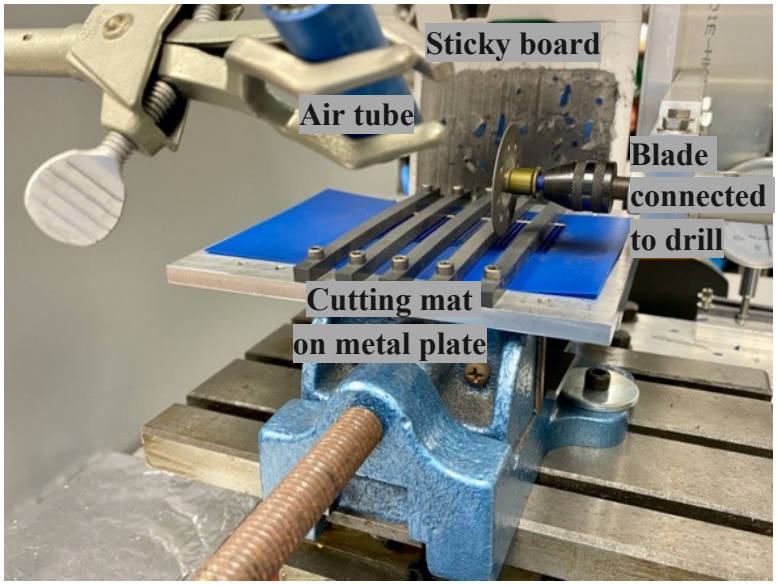

Figure 5.2: In lab set-up for cutting solar cells. Shown here is the air tube, sticky board, blade connected to drill and cutting mat on metal plate.

5.2.2 Experimental Procedure

After the solar cells' rectangles were cleaned and dried, they were etched using the 10% hydrofluoric acid solution. At first, we submerged the solar cells in the hydrofluoric solution following the same procedure in Chapter 4. Unfortunately, the hydrofluoric acid removed the solar cell backing. This was problem since this backing was essential later to test the photoefficiency. We came up with a solution by adding the hydrofluoric acid only to the surface of the solar cell. This was accomplished by placing the solar cell on top of the cap of a PFA bottle. However, this procedure limited the amount of hydrofluoric acid we could use. In the end, the etching process involved adding 400 μL of 10% hydrofluoric acid to the surface of a clean solar cell rectangle for 18 minutes, then rinsing in DI water multiple times and placed in the oven (150 °C) to dry for 3 minutes.

5.2.3 Results and Discussion

The first part of the project was to cut the solar cell into rectangles that would fit into the cleaning and reaction set-up. The main problem was that we could not use a diamond scribe, as previously done with silicon wafers, since the thin silicon solar cells were fragile and shattered with any force. We solved this problem by using cutting blade attached to a drill (see Figure 5.2). The solar cell was placed on top of a cutting mat that rested on a flat aluminum plate. To ensure that the solar cell did not move during the cutting, we applied downward pressure by carefully screwing down plastic rectangular strips (thin gray objects in Figure 5.2). In this set-up, we also placed a tube with air to ensure that dust and any small solar cell fragments would flow to the back of the apparatus, where a sticky board caught them.

Once we had the thin silicon solar cells in the desired size, the next step was to remove the anti-reflective coating. This was done using a 10% hydrofluoric acid solution. The reason why we use hydrofluoric acid was because it served three purposes: 1) removed the anti-reflective coating, 2) did not react with the thin silver electrodes on the front surface, and 3) hydrogenated the surface for the next step. Other methods we found to remove the anti-reflective coating, also removed the silver electrodes.

As an aside, before we figured out that the hydrofluoric acid did not removed or damaged the silver electrodes, we developed a silver paint that could potentially be reapplied to the etched solar cell to test its efficiency. In the end it was not necessary, but we had it available in case the silver electrodes were damaged with the subsequent reactions.

We conducted an experiment to determine the optimal time to remove anti-reflective coating to ensure we did not damage the solar cells. The experiment consisted of adding 400 μL of 10% hydrofluoric acid solution to 10 clean solar cells rectangles (cut from the same solar cell) and measured the contact angle of the solar cell etched surface. We measured the contact angle 3 times and averaged the results. The results are shown in Figure 5.3.

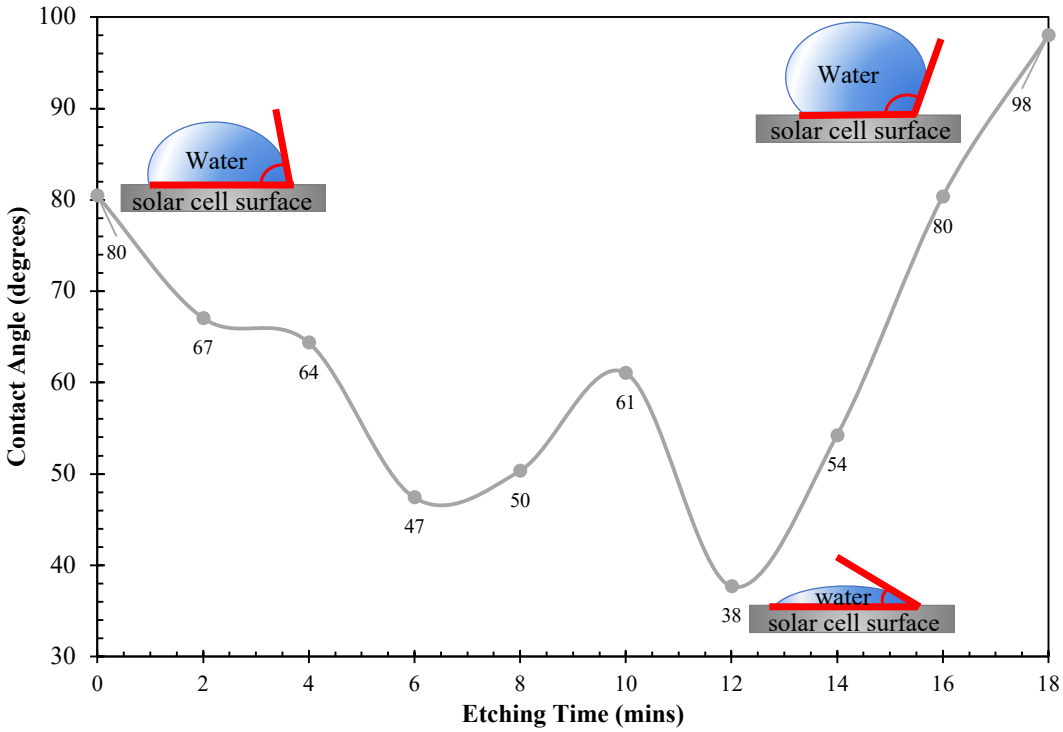

Figure 5.3: Contact angle measurements taken at 2, 4, 6, 8, 10, 12, 14, 16, and 18 minutes of etching time of 10 different solar cell rectangles to determine the optimal anti-reflective coating removal and etching time. Also, shown are schematic images of the water in contact with solar cell surface.

The starting contact angle of 80° established the nature of the anti-reflective coating covering the thin silicon solar cells as hydrophobic. As etching time progressed, the surface became more hydrophilic (contact angle decreased). After 6 minutes of etching the contact angle increased. A plausible explanation for this increase in hydrophobicity was the removal of a second layer of coating. From this experiment, we determined that it took 12 minutes to remove the anti-reflective coating. At 12 minutes the contact angle was the most hydrophilic (38°). As explained in Chapter 4, the nature of clean silicon surface is hydrophilic due to its Si-O and Si-OH bonds. After 12 minutes the surface became more hydrophobic (contact angle increased). This led to us to conclude that the Si-O and Si-OH were being replaced by Si-H bonds.

We also tested 20 minutes of etching time (not shown in Figure 5.3) which decreased the contact angle and damaged the solar cell. After 20 minutes of etching time, solar cell became

more fragile leading to breakage and decrease in photoefficiency. Once the anti-reflective coating was removed from the solar cell surface and silicon at the surface etched using the optimal time of 18 minutes, the solar cells were modified with the linker molecule.

5.3 Attachment of Linker Molecules to Solar Cell Surfaces

The chosen linker molecules had two main properties: a terminal double bond that was essential for binding to silicon surface of solar cell and an amine or carbonyl group that has an affinity towards silver. Using Cicero *et al.* procedure, we attached the chosen linker molecules: allylamine, 4-pentenoic acid, 5-hexenoic acid and undecylenic acid. The actual process of how we accomplished will be described in this section.

5.3.1 Materials and Preparation

Allylamine, 4-pentenoic acid, 5-hexenoic acid and undecylenic acid were all purchased from Sigma Aldrich. 10% (v/v) solutions of these compounds were made using acetonitrile as the solvent. Allylamine was stored in a glove box due to its potential for hazardous polymerization.

5.3.2 Experimental Procedure

The functionalization of the thin silicon solar cell followed the same procedure outlined in Chapter 4. The hydrogenated thin silicon solar cell rectangle was submerged in a quartz vial containing a 10% (v/v) solution of the linker molecule then placed into the UV photochemical reactor (see Figure 4.7). The solar cell rectangle rested on a Teflon ring that enabled a magnetic stir bar to mix the solution without striking the thin solar cell rectangle. While being stirred, the solution with the silicon wafer was exposed to the 254 nm UV light for 60 minutes to 90 minutes. Once the reaction was done, the solar cell was rinsed in tetrahydrofuran (THF) for 4 minutes following the same procedure as Yamada *et al.*[3] and placed in the oven (150 °C) to dry for 4

minutes.

5.3.3 Results and Discussion

As mentioned earlier, we were only able to use contact angle measurements to monitor the attachment of linker molecules. A schematic of the general procedure of attaching 5-hexenoic acid to the solar surface along with the measured contact angle is shown in Figure 5.4.

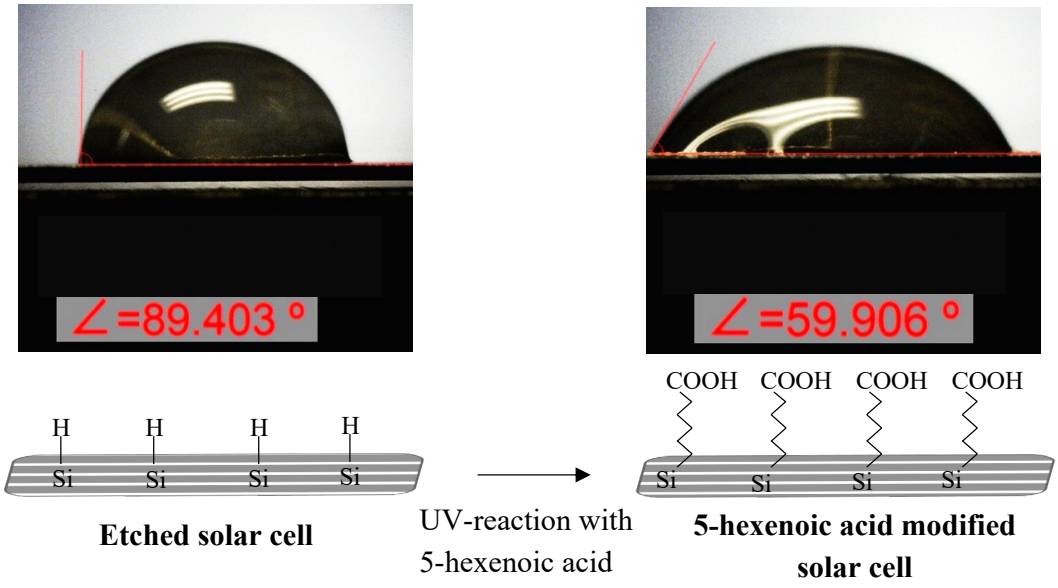

Figure 5.4: Contact angle of a water droplet on a etched silicon solar surface (left) and modified with 5-hexenoic acid (right). (bottom) Also shown is a schematic of the solar surface corresponding to each contact angle.

The top left panel of Figure 5.4 shows the contact angle of a water droplet on the solar surface etched or specifically terminated with Si-H bonds. The top right panel shows the contact angle of a water droplet on the solar surface terminated carboxylic acid group. The reduction from 89 degrees in the Si-H case to an angle of 60 degrees demonstrates that the surface has been converted to a more polar surface, as one would expect if 5-hexanoic, with its polar carboxylic acid group, now terminates the surface. However, there are also C-H bonds in the linker molecule, possibly explaining why the angle is not as low as in the case of the clean silicon surface. The

value of 60 degrees is comparable what is found on the literature for carboxylic acids on silicon surfaces found by Coffinier *et al.*[4]

5.4 Attachment of Silver Nanoparticles to Linker Molecule

5.4.1 Materials and Preparation

The nanoparticles used to bind to the modified thin silicon solar surface were triangular AgNPs prepared by the borohydride-reduction/peroxide-oxidation method described in Chapter 2. The AgNPs solutions were centrifuged (see Chapter 2 for procedure), and the pellet was resuspended in DI water.

5.4.2 Experimental Procedure

Initially, to attach the AgNPs to the modified thin silicon solar surface, we used the same procedure described in Chapter 4, where we submerged the modified thin silicon solar rectangle into a 20 mL glass vial containing the triangular AgNPs solution. Unfortunately, the AgNPs solution damaged the backing of the solar cell. Therefore, we only added 750 μL of AgNPs solution to the surface at 60-minute increments. The total nanoparticle surface area of 4.29 x 10^{15} nm^2 for 750 μL of AgNPs, based on the calculations in Chapter 4, was enough to cover the surface area of each thin solar cell surface (6.75 x 10^{14} nm^2).

After each 60-minute increment, the surface was cleaned by rinsing with DI water for 4 minutes. Afterwards, the modified silicon solar cell was dried in the oven (150° C) for 4 minutes. Once the surface dried, we took a UV-Visible scattering spectrum and measured the photoefficiency.

5.4.3 Results and Discussion

Figure 5.5 shows the UV-Visible-near IR scattering spectrum of a solar cell modified with allylamine and AgNPs compared to the spectrum of an unmodified solar cell as a reference. Both spectra are plots of the log of the ratio's intensity of the sample and the intensity of the reference plotted over the wavelength. The spectrum of modified solar cell shows an increase in the scattering of the AgNPs in the desired region of 700 nm to 1100 nm. Note that this behavior contrasts with the silicon wafer study in Chapter 4, in which the peak in the scattering spectrum occurred near 400 nm. We are not sure of the reason for the different scattering behavior, but a possible explanation has to do with the difference in surface quality. Looking at images of silicon surfaces compared to solar cells under the Scanning Electron Microscope SEM), one can see that silicon surfaces tend to be more uniform compared to solar cells which have more crevices. It is possible that in these crevices is where the AgNPs could be oriented at an angle to the surface. Thus, the vertical selection rule that prevented the near-IR peak from being observed could be overcome. After the UV-Visible scattering was taken of the solar cells the next step was to measure the photoefficiency of the modified solar cells.

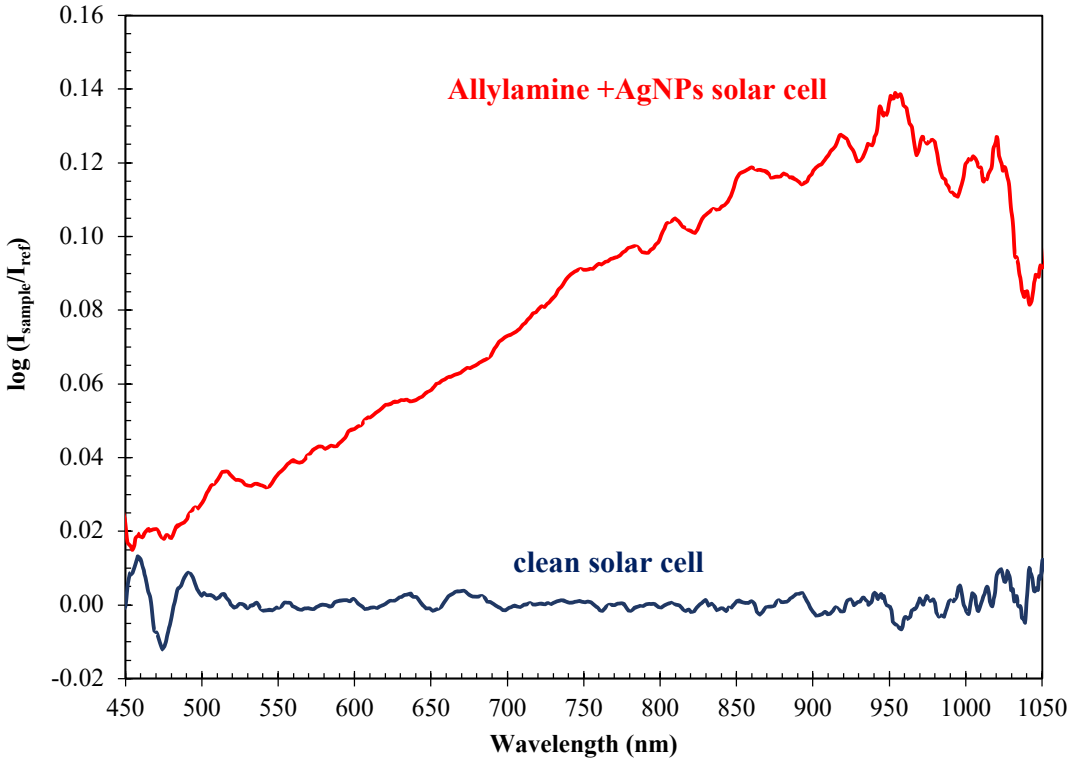

Figure 5.5: UV-Visible scattering spectra of a clean solar cell compared to a solar cell modified with allylamine linker and silver nanoparticles.

5.5 Solar Cell Efficiency

5.5.1 Simple Solar Simulator

The solar cell photoefficiency was measured using a set-up built in our lab. The first version of this set-up consisted of a light source that was placed above the modified soar cell, a voltmeter, a variable resistor, and an ammeter (see Figure 5.6).

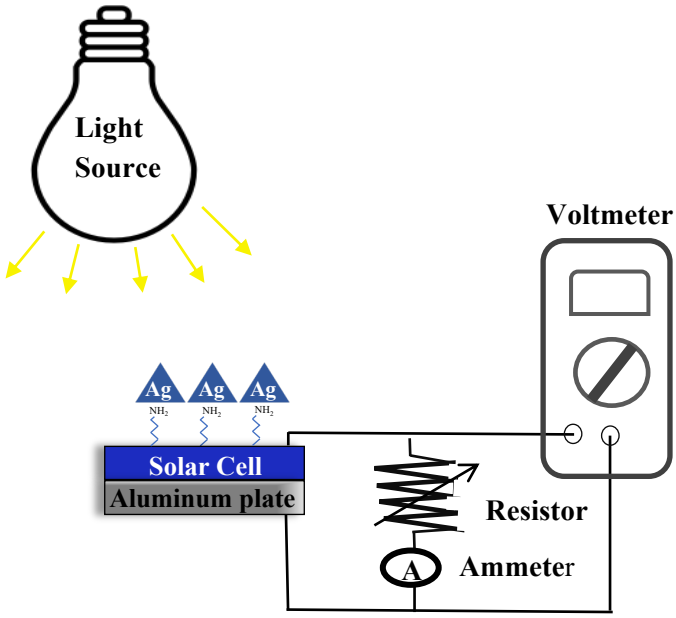

Figure 5.6: Schematic of our simple lab set-up to measure photoefficiency of solar cells. Shown is a solar cell modified with allylamine and AgNPs.

The modified solar cell was placed on an electrically-isolated aluminum plate that was connected to a voltmeter and the other side was connected to a variable resistor along with an ammeter. Using this set-up, we measured, the voltage of the open (V_{oc}) and short (V_{sc}) circuit, current of short circuit (I_{sc}) and then we manually varied the resistance from 1-100 ohms and recorded both voltage (V) and current (mA). We took 3 separate measurements for each solar cell.

The measured current in mA, I, is then plotted with corresponding voltage in volts, V. The obtained I-V Curves of the modified solar cells are shown in Figure 5.7. These were the preliminary results of the modified allylamine and undecylenic acid solar cells compared with a solar cell that has been etched and a clean solar cell. The plots show the current (mA) over the voltage in volts (V). Both modified solar cells were exposed to the AgNPs solution made the same day for only two hours. From these plots, at the start of the curve allylamine modified cell shows a slight increase in the current compared to the etched solar cell. However, the overall current and voltage for the modified solar cells are lower than the etched and unmodified solar cell. From these I-V plots, the efficiency of the solar cells was determined.

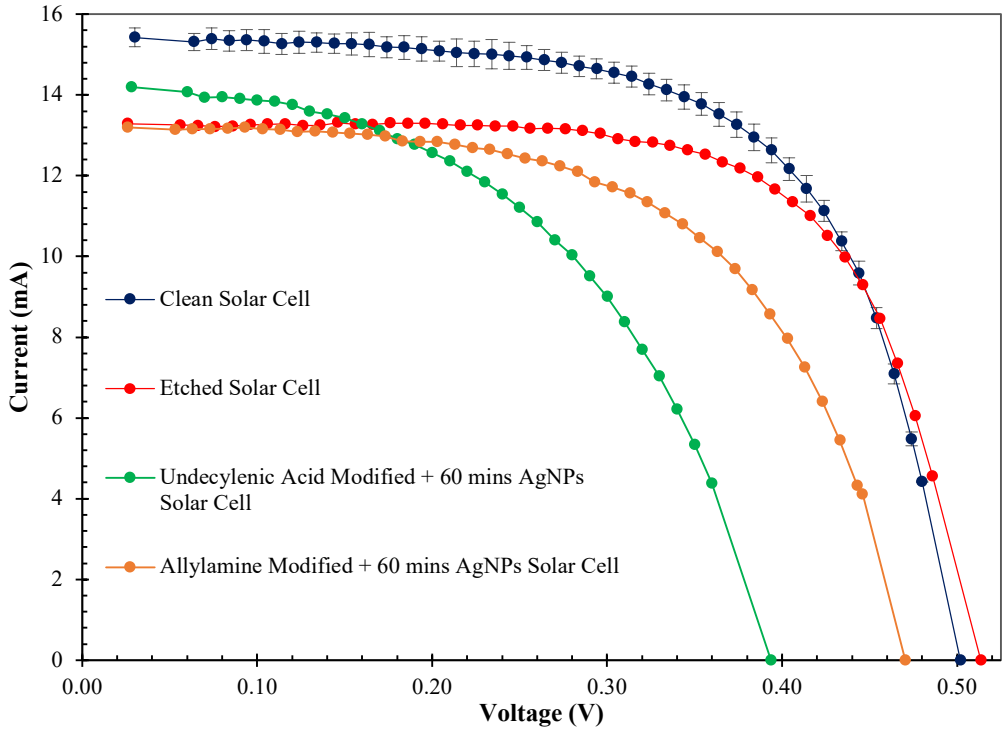

Figure 5.7: I-V curve of modified solar cells compared to an etched and clean solar cell. The modified solar cells were reacted with two linker molecules: undecylenic acid and allylamine. Then these modified soar cells were exposed to AgNPs.

5.5.2 Improved Solar Simulator

This set-up was improved by adding two modules for Arduino (8-Channel 5V relay) where various resistors were connected and a new lamp with a wavelength range and power closer to that given by the sun. We connected resistors of increasing resistance (1 Ω, 2 Ω, 4 Ω, 8 Ω, 16 Ω, 32 Ω, 64 Ω, and 128 Ω) to each relays channel of one of the Arduino modules. The other module was short circuited and connected to the module with resistors. This created a closed circuit which we connected to a voltmeter. First, we measured the voltage of the open (V_{oc}) and short (V_{sc}) circuit, by turning on and off all the relays. Then by turning on the relay channels with resistors, we increased the resistance with a delay to measure the voltage. The Arduino code used to measure the voltage is found on the Appendix section C. The improved set up is shown in Figure 5.8. Our lab build solar simulator was made with a fraction of the cost of a solar simulator.

This set up could be a good alternative for a lab that does not have the monetary funds to invest on a solar simulator.

This set-up was improved and automated by adding 1) a new lamp (model 150R, Solarlux) with a wavelength distribution and power (1000 W/m2) similar to that of the sun, and 2) a computer-controlled Arduino module that automatically varied the resistive load using two relays connected to various discrete resistors. The relays were 8-Channel 5V relays that allowed resistors of increasing resistance (0 Ω, 1 Ω, 2 Ω, 4 Ω, 8 Ω, 16 Ω, 32 Ω, 64 Ω, and 128 Ω) to be connected in series to obtain load resistances between 0 and 255 Ω.s. The other module was short circuited and connected to the module with resistors. This created a closed circuit which we connected to a voltmeter. First, we measured the voltage of the open (V_{oc}) and short (V_{sc}) circuit, by turning on and off all the relays. Then by turning on the relay channels with resistors, we increased the resistance with a delay to measure the voltage. The Arduino code that we wrote to measure the voltage is found in Appendix section C. The improved set up is shown in Figure 5.8. Our lab-built solar simulator was made for about $800, or 5-10% of the cost of a commercial solar simulator.

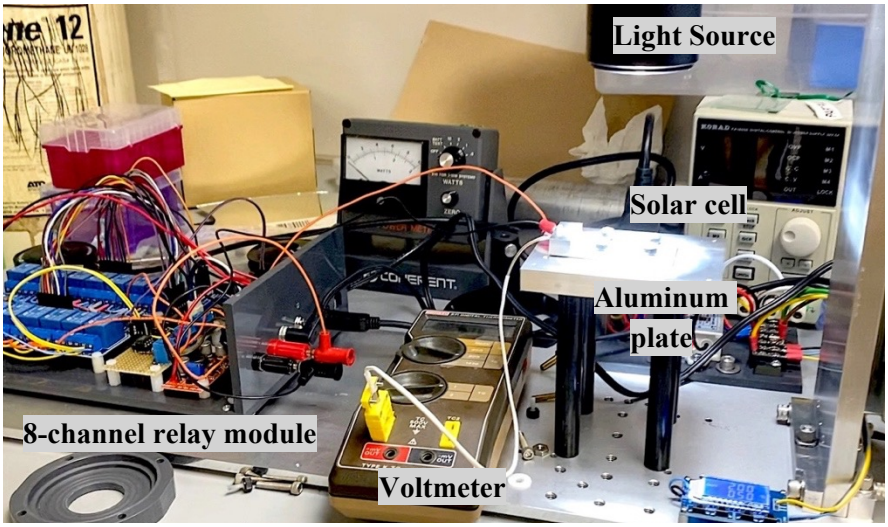

Figure 5.8: Image of improved lab set-up to measure photoefficiency of solar cells. Shown here are the two relays, voltmeter, aluminum plate, and light source.

For the improved set-up the same procedure was followed as in the simple set up. The

only difference was that we increased using the Arduino program instead of manually. After we measured the current and voltage of the modified cells, we calculated the photoefficiency. There were two methods to determine how efficient a solar cell is: fill factor (FF) and energy conversion efficiency.

5.5.3 Fill Factor and Photoefficiency

One method to determine the efficiency of solar cells is Fill Factor (FF). Fill factor is the ratio of the maximum power, P_{max}, obtained from the current-voltage (I-V) curve compared to the P_T, theoretical value. P_{max} is defined as the highest power obtained from the curve whereas the theoretical power, P_T, is the short circuit current, I_{sc}, multiplied by the open circuit voltage, V_{oc} (Equation 5.1). The Fill Factor essentially is a comparison of the maximum power given by the solar cell to the theoretical value. The higher the fill factor the more efficient the solar cell.

$$Fill\ Factor\ (FF) = \frac{P_{max}}{P_T} = \frac{I_{max} * V_{max}}{I_{sc} * V_{oc}} \tag{5.1}$$

$$\mathbf{P_{max}} = Maximum\ power\ (W)$$

$$\mathbf{P_T} = Theoretical\ power\ (W)$$

$$\mathbf{I_{max}} = Maximum\ current\ (A)$$

$$\mathbf{V_{max}} = Maximum\ voltage\ (V)$$

$$\mathbf{I_{sc}} = Short\ circuit\ current\ (A)$$

$$\mathbf{V_{oc}} = Open\ circuit\ voltage\ (V)$$

Figure 5.9 shows a visual of the fill factor (FF) in respect to an I-V curve. The I-V curve shown here is of the unmodified solar cell from Figure 5.7.

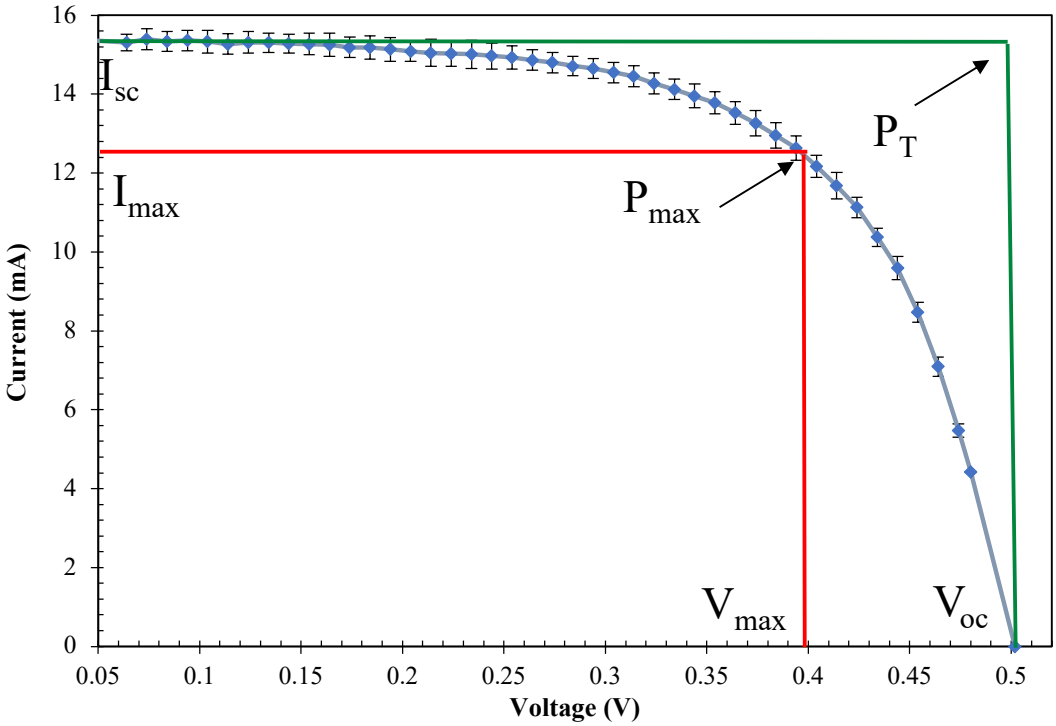

Figure 5.9: I-V curve of a clean solar cell showing a visual representation of the fill factor and its parameters.

The other method to determine the efficiency of solar cells is photoefficiency. Photoefficiency is the ratio of the maximum power, P_{max}, obtained from the current-voltage (I-V) curve compared to the P_{in}. P_{in} is defined as the highest power obtained from the curve whereas the power in, P_{in}, is the incident radiation flux (W/m^2), E, multiplied by the area of collection, A_c or power going in from the solar simulator (Equation 5.2). In other words, photoefficiency is a comparison of the maximum power given by the solar cell to the power going into the solar cell. The higher the value of photoefficiency, the more efficient the solar cell is at converting the power going in into electricity. For the modified solar simulator, the incident radiation flux or E was equal to 1000 W/m^2 and the area of collection or A_c was equal to 1.13 x 10^{-4} m^2.

$$Photoefficiency = \frac{P_{max}}{P_{in}} = \frac{P_{max}}{E * A_c} \tag{5.2}$$

$$\mathbf{P_{max}} = Maximum\ power\ output\ (W)$$

$$\mathbf{P_{in}} = Power\ going\ in$$

$$\mathbf{E} = Incident\ radiation\ flux\ (W/m^2)$$

$$\mathbf{A_c} = Area\ of\ collection\ (m^2)$$

5.5.4 Effect of Silver Nanoparticles on Etched Solar Cells

Control experiments were carried out in which I-V curves were measured for etched solar cells-but not functionalized with linker molecules- were exposed to AgNPs. The results are shown in Figure 5.10. The control solar cell consisted of an etched solar cell that was exposed to the AgNPs solution at 60 minutes increments. We started by cleaning a rectangular solar cell using the method outlined in section 5.2.1. Once it was cleaned, both voltage and current were measured using the improved solar simulator (blue curve). This was done to have a baseline of the clean solar cell. The next step was to etch the solar cell following the same procedure as before, 18 minutes with 10% HF (red curve). Once the voltage and current were measured, then the etched solar cell was exposed for an hour with AgNPs (green curve). We followed the same procedure as in Section 5.4.2, where we added 750 μL of AgNPs solution for 60 minutes increments to the top surface of the etched solar cell while being careful that the solution did not react with the solar cell backing. We repeated the process two more times for a total exposure of 180 minutes. Table 5.1 shows a summary of the fill factor and photoefficiency of the control solar cell from Figure 5.10. The results in Table 5.1 show that exposing the etched solar cell to the AgNPs slightly decreased the photoefficiency of the etched solar from 7.1% to 6.9% after being exposed to 180 minutes of AgNPs. However, the fill factor increased from 68.1% of the etched solar cell to 69.7%. Both slight decrease in efficiency and increase in fill factor could be due to instrumental error.

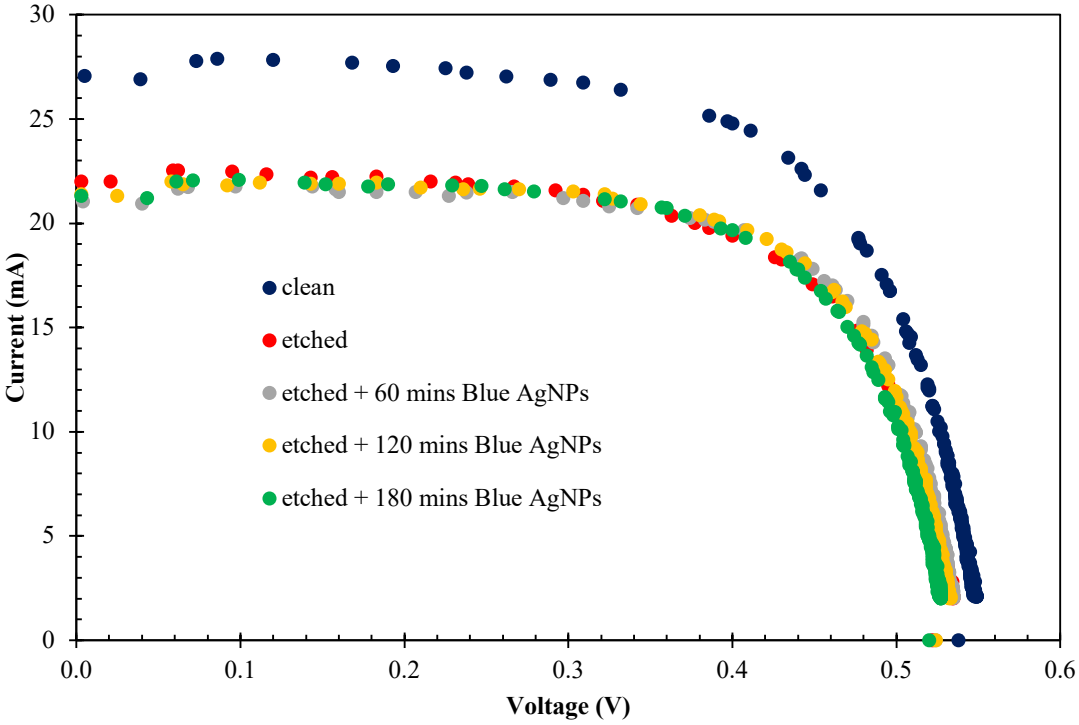

Figure 5.10: I-V Curves of a clean solar cell (blue), an etched solar cell (red), an etched solar cell with 60 minutes of AgNPs exposure (gray), an etched solar cell with 120 minutes of AgNPs exposure (yellow) and an etched solar cell with 180 minutes of AgNPs exposure (green).

Table 5.1: Fill Factor and photoefficiency results of a clean solar cell, an etched solar cell, an etched solar cell with 60 minutes of AgNPs exposure (green), an etched solar cell with 120 minutes of AgNPs exposure and an etched solar cell with 180 minutes of AgNPs exposure.

Solar Cell	**Fill Factor (FF)**	**Photoefficiency**
Clean solar cell	67.6±1.0 %	8.8±0.1 %
Etched solar cell	68.1 %	7.1 %
AgNPs (60 mins)	71.5 %	7.1 %
AgNPs (120 mins)	71.1 %	7.1 %
AgNPs (180 mins)	69.7 %	6.9 %

From the results of the control experiment we determined that adding AgNPs directly on top of the solar cell without a linker molecule did not increase the solar cell efficiency. This agrees with our simulations from Chapter 3, where the AgNP-to-silicon distance of 0 nm had the lowest extinction cross-section in comparison to 1, 2, 3,5 and 20 nm distances.

5.5.5 Effect of Linker Molecule Length on Solar Cell Efficiency

Once we determined that the AgNPs solution did not decrease the efficiency of the etched solar cells, the next step was to calculate the efficiency of the modified solar cells with allylamine, 4-pentenoic acid, 5-hexenoic acid and undecylenic acid exposed to AgNPs. Figure 5.11 and Table 5.2 show the results of the four modified solar cells with the linker molecules after being exposed to 60 minutes of Blue AgNPs solution. The highest efficiency was achieved by the 5-hexenoic acid + Blue AgNPs modified solar cell with a fill factor of 76.5% and 10.5% photoefficiency. Comparing the 5-hexenoic acid + Blue AgNPs modified solar cell to the etched solar cell there was a slight increase of from 10.0% to 10.5%. The lowest efficiency measured was of the 4-pentenoic

acid + Blue AgNPs modified solar cell. It had a fill factor of 68.5% and 8.9% photoefficiency compared to the etched solar cell which had an 8.7% photoefficiency. The difference was 0.2%, and since the photoefficiency uncertainties are 0.1%, the difference is statistically insignificant. However, the lowest conversion efficiency, meaning the efficiency compared to the etched solar cell was the undecylenic acid + Blue AgNPs solar cell. The undecylenic acid + Blue AgNPs solar cell efficiency decreased from 10.4% etched to 9.8%, a difference of 0.6%, which is statistically significant.

A possible explanation for the undecylenic acid solar cell to have the lowest conversation efficiency is the fact that it is the longest linker molecule we tested. Comparing the carbon chain length, undecylenic acid has11 carbons, 4-pentenoic acid has 5 carbons and 5-hexenoic acid has 6 carbons. The 11-carbon chain length could potentially be past the limit of the optimal length for the AgNP to enhancing the photoefficiency (see Chapter 4 for a theoretical discussion of the existence of a non-zero optimal AgNP-surface distance). Using these results as a guideline, we decided to test effect of various AgNPs solutions on the 5-hexenoic acid modified cells since it was the one that had the highest efficiency.

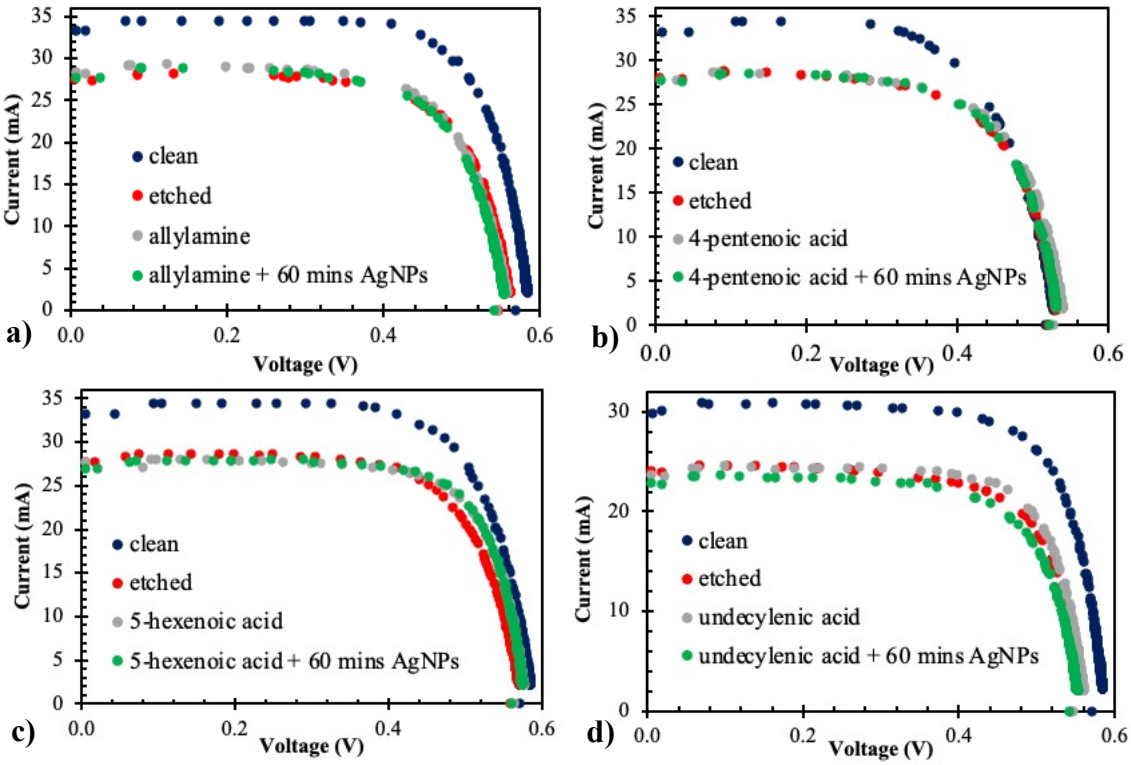

Figure 5.11: I-V Curves of the progression of four modified solar cells exposed to 60 minutes of AgNPs. (a) Allylamine modified solar cell, (b) 4-pentenoic acid modified solar cell, (c) 4-pentenoic acid modified solar cell and (d) undecylenic acid modified solar cell.

Table 5.2: Fill Factor and photoefficiency results of four modified solar cells exposed to 60 minutes of AgNPs. In increasing length, allylamine, 4-pentenoic acid cell, 5-hexenoic acid and undecylenic acid modified solar cells.

Solar Cell	**Fill Factor (FF)**	**Photoefficiency**
Allylamine + Dark Blue AgNPs (60 mins)	71.8±1.0%	9.5±0.1 %
4-Pentenoic Acid + Dark Blue AgNPs (60 mins)	68.5%	8.9 %
5-Hexenoic Acid + Dark Blue AgNPs (60 mins)	76.5 %	10.5 %
Undecylenic Acid + Dark Blue AgNPs (60 mins)	71.7%	9.6 %

5.5.6 Effect of Different Types of Silver Nanoparticle Solutions on Solar Cell Efficiency

In Chapter 2, we discussed in detail two methods to synthesize AgNPs that absorbed light in the infrared region: photochemical method and simultaneous chemical oxidation and reduction. The photochemical method produced AgNPs whose solutions were light blue in color, while the simultaneous chemical oxidation and reduction AgNP solutions were dark blue. To simplify the name from now on, the nanoparticle's solutions are going to be referred to using their color. Also, we are going to be using the AgNPs synthesized by the borohydride reduction method that were yellow in color and spherical in shape. These AgNPs do not absorb in the infrared region and were used as a comparison.

The results of exposing a 5-Hexenoic acid modified solar cell to the various AgNPs solutions are shown in Figure 5.11 and Table 5.3. The first I-V curve (a) shows a 5-Hexenoic acid modified solar cell exposed to dark blue AgNPs. The next curve shown (b) is a 5-Hexenoic acid modified solar cell exposed to light blue AgNPs. The I-V curve shown is the comparison experiment of exposing a 5-Hexenoic acid modified solar cell to the yellow AgNPs. All the modified solar cells were exposed to the AgNPs solutions for 60 minutes following the procedure outlined in section 5.4.

The highest efficiency was achieved by the 5-hexenoic acid modified solar cell exposed to the dark blue AgNPs with a fill factor of 76.5% and 10.5% photoefficiency. Comparing the 5-hexenoic acid modified solar cell exposed to the dark blue AgNPs to etched solar cell there was slight increase of from 10.0% to 10.5%. The lowest efficiency measured was of 5-hexenoic acid modified solar cell exposed to the light blue AgNPs. It had a fill factor of 73.7% and 7.8% photoefficiency compared to the etched solar cell which had an 7.7% photoefficiency. The difference was 0.1%. This difference could be due to instrumental error. The control experiment of using yellow AgNPs had the lowest conversion efficiency from 11.1% to 9.8%, decrease of

1.3%. Since this AgNPs do not absorb in the near infrared region a plausible explanation that led to this decrease are chemicals found in the AgNPs solutions.

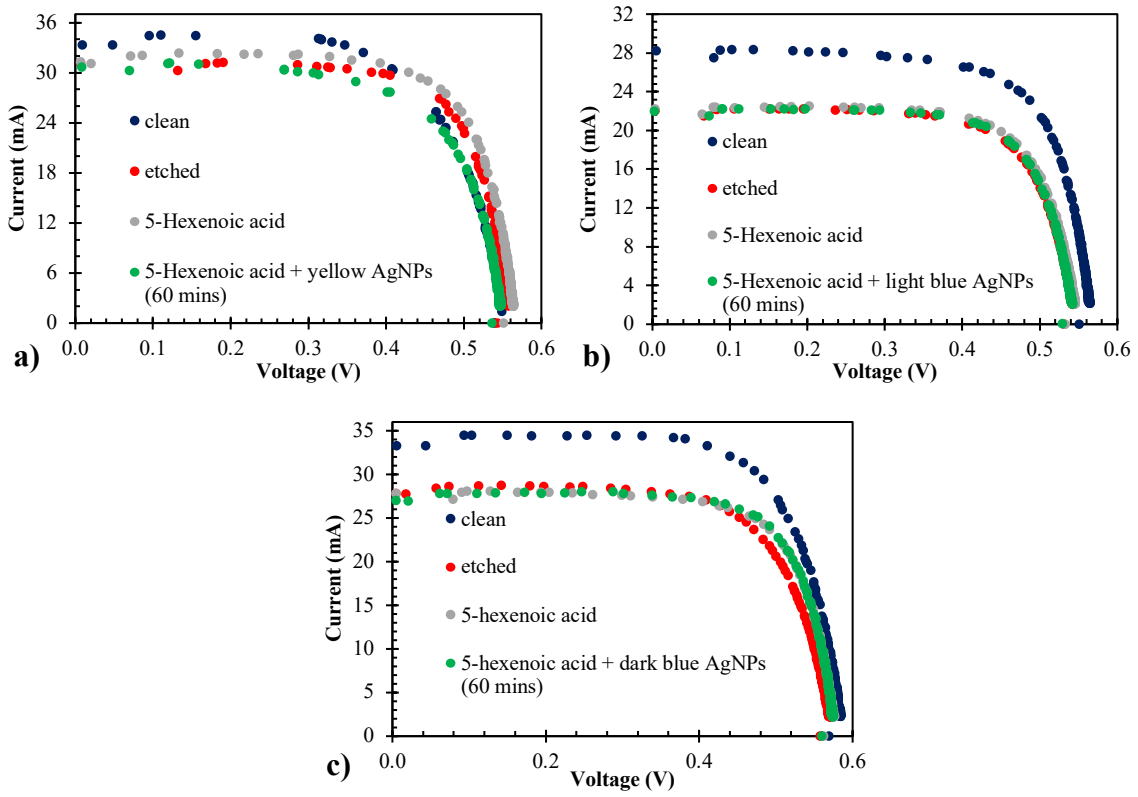

Figure 5.12: I-V Curves of the progression of three 5-hexenoic acid modified solar cells exposed to 60 minutes of (a) Dark Blue (b) Light Blue and (c) Yellow AgNPs.

Table 5.3: Fill Factor and photoefficiency results of a 5-hexenoic acid modified solar cell with 60 minutes exposure to dark blue, light blue and yellow AgNPs.

Solar Cell	**Fill Factor (FF)**	**Photoefficiency**
5-Hexenoic Acid + dark blue AgNPs (60 mins)	76.5±1.0 %	10.5±0.1 %
5-Hexenoic Acid + light Blue AgNPs (60 mins)	73.7 %	7.8 %
5-Hexenoic Acid + yellow AgNPs (60 mins)	66.8 %	9.8 %

5.5.7 Conclusion and Future Work

In conclusion, the results presented are a proof-of-concept that the solar cell efficiency of solar cells can be increased by attaching the blue AgNPs using terminal alkene linker molecules that are 4 to 10 carbons in length. It is important to note that the reference solar cell used in this comparison is the etched cell and not the original solar cell that had an anti-reflection coating. The original cell had a higher photoefficiency, but for this to be the suitable reference cell, we would need to apply an anti-reflection coating to our sensitized cells. Determining a suitable coating and method of application would be a research project in itself. For the linker molecules tested, 5-hexenoic acid, which is 6-carbons in length, was optimal while the least successful linker molecule was undecylenic acid. This led us to conclude that 11 carbons passed the optimal nanoparticle-to-silicon distance for enhancement. Future experiments could study linkers of 7, 8 and 9 carbon atoms to see if they lead to further improvements in efficiency. In addition, different shapes and sizes of the AgNPs could be tested.

5.6 References

1. Shockley, W.; Queisser, H. J. Detailed Balance Limit of Efficiency of p-n Junction Solar Cells. *Journal of Applied Physics* **1961**, *32* (3), 510-519.

2. Cicero, R. L.; Linford, M. R.; Chidsey, C. E. D. Photoreactivity of Unsaturated Compounds with Hydrogen-Terminated Silicon (111). *Langmuir* **2000**, *16* (13), 5688-5695.

3. Yamada, T.; Noto, M.; Shirasaka, K.; Kato, H. S.; Kawai, M. Photoassisted Adsorption of Allylamine and 1-Butene on H:Si(111) Studied by Surface Vibrational Spectroscopies. *The Journal of Physical Chemistry B* **2006**, *110* (13), 6740-6749.

4. Coffinier, Y.; Piret, G.; Das, M. R.; Boukherroub, R. Effect of Surface Roughness and Chemical Composition on the Wetting Properties of Silicon-Based Substrates. *Comptes Rendus Chimie* **2013**, *16* (1), 65-72.

Chapter 6

Modeling Silver Nanoparticles in Solution via the Discrete Dipole Scattering Program

6.1 Introduction

The dramatic and continuous advancement in computer technology over the past few decades, together with advances in theoretical approaches in chemistry and physics, has enabled the nearly routine use of chemical computational simulation methods to predict phenomena and interpret experimental results. The development of the Discrete Dipole Approximation and its implementation in the Discrete Dipole Scattering (DDSCAT) computational program is a good example.[1] In Chapter 3, we discussed the DDSCAT computational program developed by Draine *et al.*[1] as a simulation tool for modeling the optical response of irregularly shaped particles, in our case triangular shaped silver nanoparticles (AgNPs).

The purpose of the project described in the present chapter is to simulate the UV-visible absorption spectra of triangular shaped AgNPs in solution using the DDSCAT computational program. The reason the simulation is important is that it will provide a cross-check or link

between 1) the observed UV-visible absorption spectra of the nanotriangles used in modifying the solar cell surfaces and 2) the observed TEM images of the nanotriangles. In other words, we want to check whether the UV-visible spectra are consistent with the size distribution of the nanotriangles.

The underlying idea of the simulation is that the silver nanoparticles in solution are triangular and have a distribution of sizes. Since each size gives rise to a different spectrum, the observed spectrum will be an average over the spectra from all nanoparticles, weighted by their fractional population. Averaging over the tumbling, rotational motion of the nanoparticles must also be taken into account. In the literature, one can find research articles using DDSCAT to simulate AgNPs.[2−4] However, to the best of our knowledge, there are no reports using the DDSCAT program to simulate triangular shaped AgNPs in solution using rotational averaging.

The first part of the project was to synthesize AgNPs using the method developed by Song[5] and Panzarasa[6] and then modified by our lab. The exact method for this synthesis will be published by our lab in the near future. The next step was to characterize the morphology and optical properties of the nanoparticles by recording Transmission Electron Microscopy (TEM) images of them and UV-Visible absorption spectra of the nanoparticle solutions. This was done by a previous member of our lab Nobuyuki Yamamoto.[7] The images indicated that the AgNPs were predominantly triangular in shape. With the help of the TEM, the sizes of 214 individual particles were measured, and their size distribution is shown in the histogram in Figure 6.1. Also shown in Figure 6.1 is the UV-Visible absorption spectrum of the nanoparticle solution. In the computer simulations that will be descibed in this chapter, the key factors that were taken into consideration in computing the absorption spectrum of these nanoparticles were their size and shape as well as the wavelength-dependent refractive index of silver, and the refractive index of the solution.

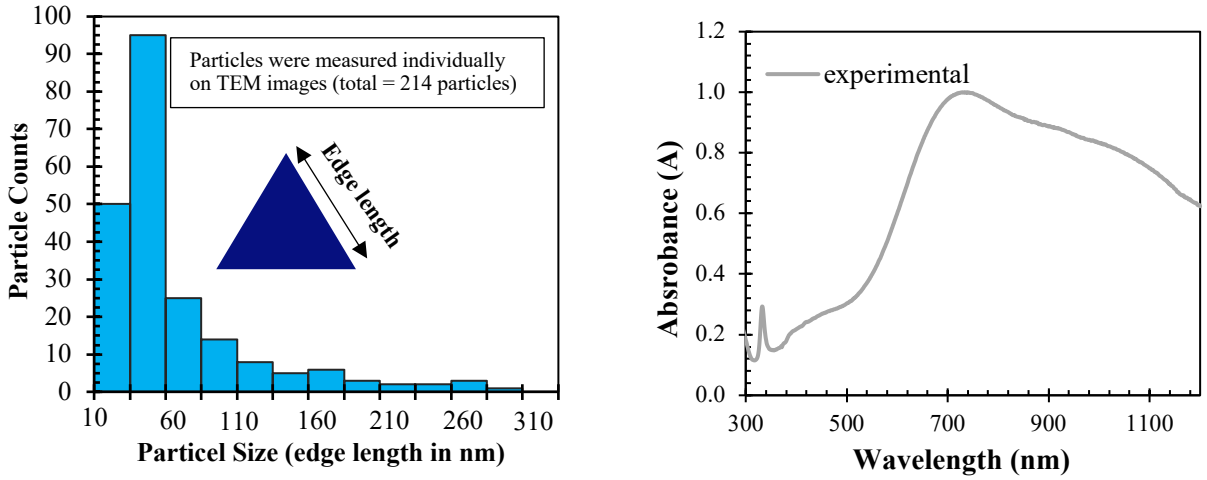

Figure 6.1: TEM histogram of the size distribution of triangular AgNPs, and (right) experimentally-observed UV-Visible absorption spectrum of AgNPs in solution. The particle size is taken as the edge length of the triangular AgNPs.

As explained in Chapter 3, all DDSCAT calculations require three input files: the shape and parameter files, as well as a file containing the complex refractive index (and dielectric function) of the material as a function of wavelength. The first step was to draw the triangular nanoparticle using the program called Blender[8] , Then the triangular nanoparticle was converted into an array of dipoles using a program called Shape Converter,[9] which then created the shape file. For the calculations presented in this chapter, the dipole-to-dipole distance was 0.5 nm. This distance was chosen based on the results of preliminary computations in which the UV-visible absorption and scattering spectra were simulated as a function of dipole-to-dipole distance. The computations indicated that the spectra had converged for a distance of 0.5 nm. This dipole-to-dipole distance is also comparable to the 0.407 nm edge length of silver's face-centered-cubic unit cell.

Following the same process as in Chapter 3, we used the shape and parameter files and the refractive index file, to submit the DDSCAT calculation to one of our lab computers (3.6 GHz quad core-i7, 16GB RAM) where DDSCAT was compiled with the Intel Fortran compiler and linked with the Intel MKL library (Math Kernel Library).

6.2 Effect of Optical Dielectric Function of Silver

A commonly used optical dielectric function for silver in DDSCAT calculations was determined by Lynch and Hunter and is found in the Handbook of Optical Constants of Solids.[10] The other commonly used optical dielectric function for silver is by Johnson and Christy.[11] Figure 6.2 compares these two optical dielectric functions along with a recently published optical dielectric function by Green *et al.*[12] The dashed lines show the imaginary part of the function, ε_2, and the solid curves show the real part of the function, ε_1, where the overall dielectric function, ε , can be written as $\varepsilon = \varepsilon_1 + i\varepsilon_2$. In terms of how the real and imaginary parts are related to the calculated spectra, the real part determines the scattering component of the total extinction cross-section while the imaginary part determines the absorption component.

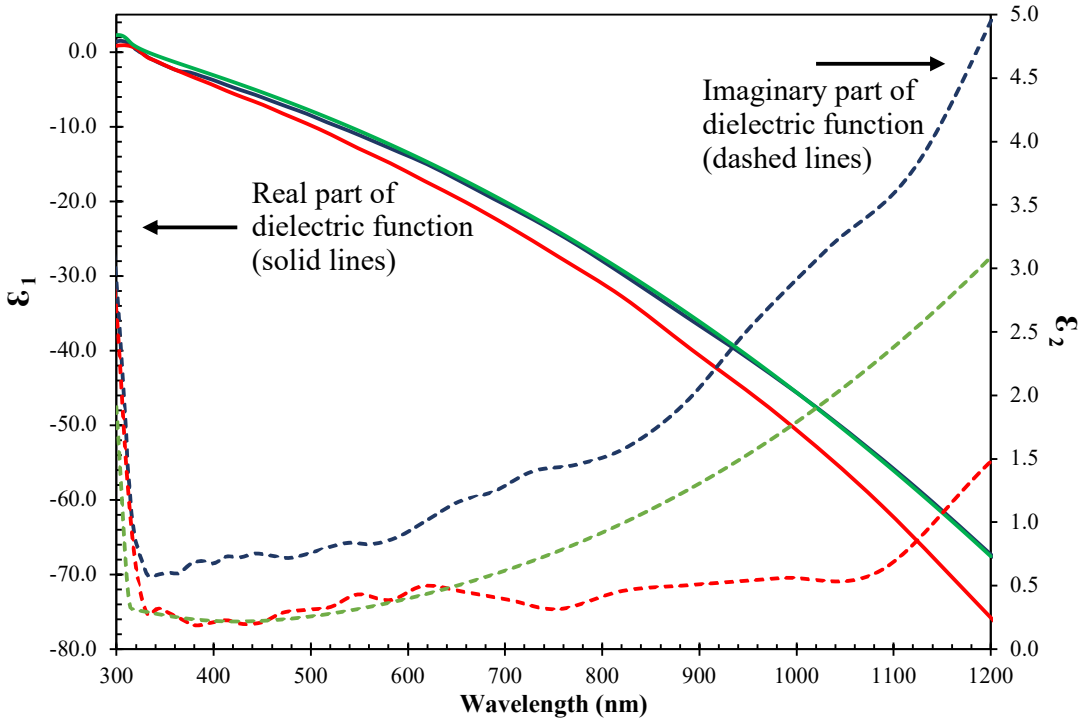

Figure 6.2: Optical dielectric functions of silver by Johnson and Christy (red), Lynch and Hunter (blue), and Green *et al.* (green). The dielectric function, ε, can be written as $\varepsilon = \varepsilon_1 + i\varepsilon_2$.

To illustrate the effect of the optical dielectric function on a DDSCAT calculation, we

determined the extinction cross-section over the wavelength range of 300 nm to 900 nm every 10 nm for a 27.5 nm edge length and 7 nm thickness triangular nanoparticle using the optical dielectric function of Lynch and Hunter compared to that of Green *et al*. The results are shown in Figure 6.3. The index of refraction of the medium in which the nanoparticle is embedded was 1.33, equal to that of water. The calculation was done using rotational averaging to resemble the AgNP being in solution.

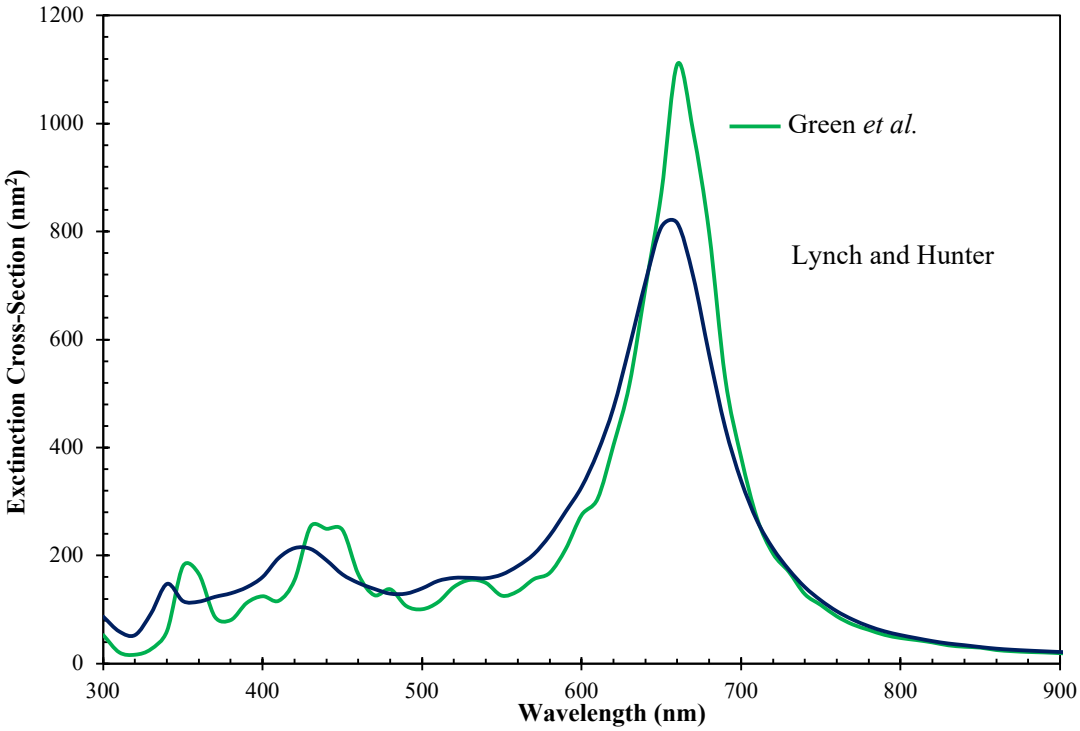

Figure 6.3: Comparison of extinction cross-section of a triangular nanoparticle of edge length of 27.5 nm and thickness of 7 nm using the optical dielectric functions of silver from Hunter and Lynch (blue) and from Green *et al*. (green).

The main resonance peak occurs at about 660 nm and is larger in magnitude for the calculations using the Green et al. optical dielectric function. More specifically the extinction cross-section at 660 nm is 1.4 times greater using the Green et al. compared to Lynch and Hunter optical dielectric function. To understand the effect of the silver dielectric function on the change in the extinction cross-section, we plotted the real and imaginary parts of both the Lynch and

Hunter and Green et al. dielectric functions in Figure 6.4, which is an expansion of the 600-700 nm region of Figure 6.2. The change in the real part of the function is about 0.63 and is 0.65 for the imaginary part of the function at 660 nm. A plausible explanation for the difference in extinction cross-section at 660 nm comes from Eqn. 18 in Harris et al.,[13] which shows that the strength of the extinction is determined mostly by the imaginary part of the dielectric function. This equation is based on the quasistatic approximation for spheres and is rewritten as Equation 6.1 below. Here, Q_{ext} is the extinction efficiency factor and is equal to the extinction cross-section, C_{ext}, divided by the effective cross-sectional area of the nanoparticle: $Q_{ext} = C_{ext} / \pi a^2$. The effective radius, a, is defined such that the actual volume, V, of the nanoparticle is $V = 4/3\ \pi a^3$.

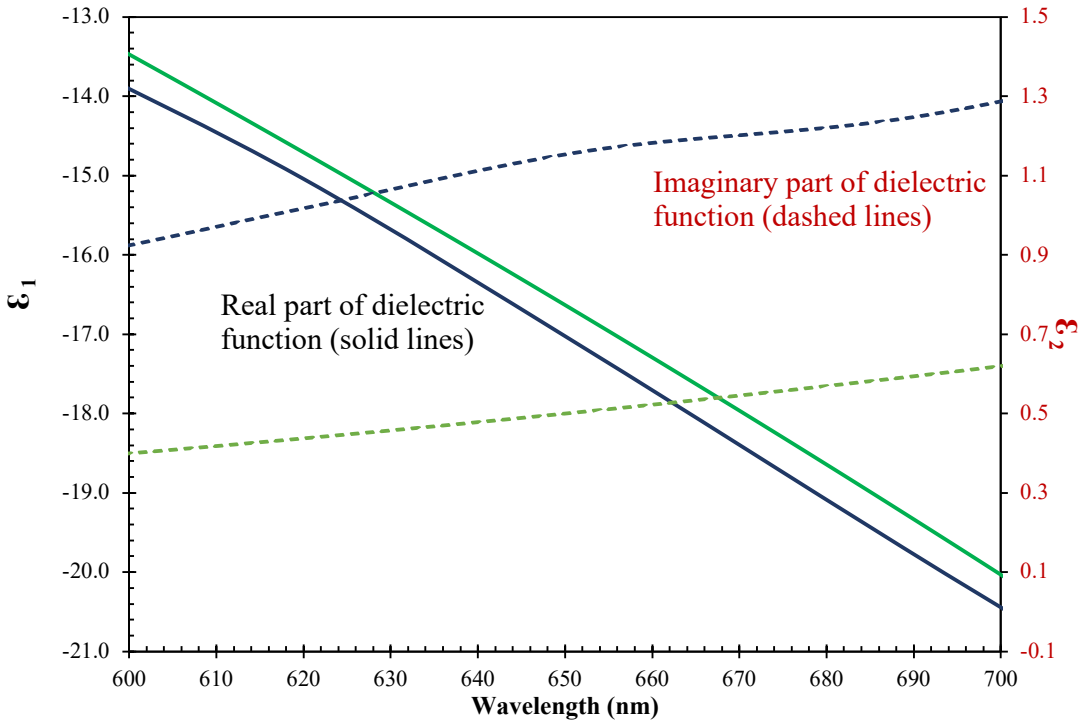

Figure 6.4: Comparison of the imaginary (red) and real (black) parts of the silver optical dielectric function by Lynch and Hunter (blue), and Green *et al.* (green).

$$Q_{ext} = \frac{24\pi a}{\lambda} \frac{\varepsilon_2 \varepsilon_m}{\varepsilon_2^2 + (\varepsilon_1 + 2\varepsilon_m)^2} \tag{6.1}$$

$$\mathbf{Q_{ext}} = Extinction\ efficiency \qquad \mathbf{a} = effective\ radius$$

$$\boldsymbol{\varepsilon_1} = real\ part\ of\ optical\ dielectric\ function\ of\ silver$$

$$\boldsymbol{\varepsilon_2} = imaginary\ part\ of\ optical\ dielectric\ function\ of\ silver$$

$$\boldsymbol{\varepsilon_m} = real\ optical\ dielectric\ function\ of\ medium$$

This expression is for spheres, but it provides a qualitative understanding for other shapes. Equation 6.1 indicates that at resonance (for spheres, ε_1= -2*ε_m), the extinction coefficient is proportional to 1/ε_2 where ε_1= real part and ε_2= imaginary part. Using the values of ε_2=1.17 (Lynch and Hunter) and ε_2= 0.52 (Green *et al.*), the extinction coefficient at 660 nm of the peak using Green e*et al*. optical dielectric function should be about twice as much as using Lynch and Hunter optical dielectric function. Based on these results and the fact that the optical dielectric function of silver by Green *et al*. provides an updated version of the optical dielectric function, we decided to use as it for the rest of the calculations.

6.3 Effect of the Medium's Refractive Index

The synthesis of the triangular AgNPs was done in water. However, it is important to realize that the AgNPs used trisodium citrate as the capping agent, so the medium in which the nanoparticles were embedded was not solely water. This is important since the dielectric constant of the medium affects the optical resonances. This can be understood in an approximate manner by considering the expression, Eqn. 6.1, for the extinction coefficient calculated within the quasistatic approximation for small spheres (diameter ¡¡ wavelength of incident light) by Harris *et al*.

Figure 6.5 shows a schematic diagram of the citrate layer covering a triangular nanoparticle. Using the refractive index of water, 1.33, as the refractive index of the medium for the

calculations would not account for the presence of the capping agent. Unfortunately, there is not an obvious way of knowing the local, effective concentration of citrate near a nanoparticle's surface. Because citrate binds weakly to the surface, its local concentration is probably higher than in the bulk. Therefore, to roughly approximate the physical situation, the refractive index of a highly concentrated (1 M) trisodium citrate solution was measured in our lab, and the value we obtained was 1.41. A 1 M trisodium citrate solution was used to resemble the concentrated capping of trisodium citrate around the surface of the AgNP. To account for the presence of the citrate in an approximate way in the nanoparticle solutions, we used a refractive index of 1.37 for the medium, the average value of 1.33 and 1.41, that would take into consideration that most of the nanoparticle will be surrounded with the capping agent and some water in the solution. Other refractive index values such as 1.39 and 1.40 were investigated to account for more of the capping agent relative to water.

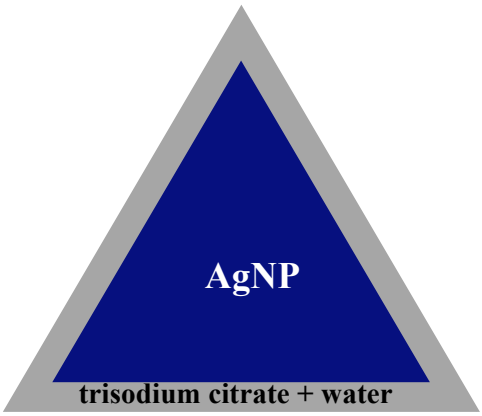

Figure 6.5: Diagram of a triangular AgNP with a capping agent layer of trisodium citrate. The triangular AgNP is shown in blue whereas the capping agent layer is shown in gray.

Figure 6.6 shows the results of changing the refractive index of the medium for a triangular nanoparticle with 27.5 nm edge length and 7 nm thickness. From this graph, the effect of increasing the medium's refractive index from pure water (n=1.33) to water and trisodium citrate (n=1.37) red shifts the extinction cross-section peak by 10 nm and increases the magnitude very slightly by 5%. The red shift is consistent with Eqn.6.1for spheres and the more negative value

of ε_1 with increasing wavelength shown in Figure 6.4. Specifically, if we use Eqn.6.1 as a very qualitative guide for understanding the optical behavior of triangles, then as n increases (and therefore ε_m increases since $\varepsilon_m = n^2$), ε_1 must become more negative to maintain the resonance condition of $\varepsilon_1 = -2\varepsilon_m$. For ε_1 to become more negative, the resonance wavelength must increase (see Figure 6.4). In subsequent calculations, we decided to use the refractive index value of 1.37 since this would account for the presence of the capping agent on the AgNPs and thus more closely resemble the experimental conditions in solution.

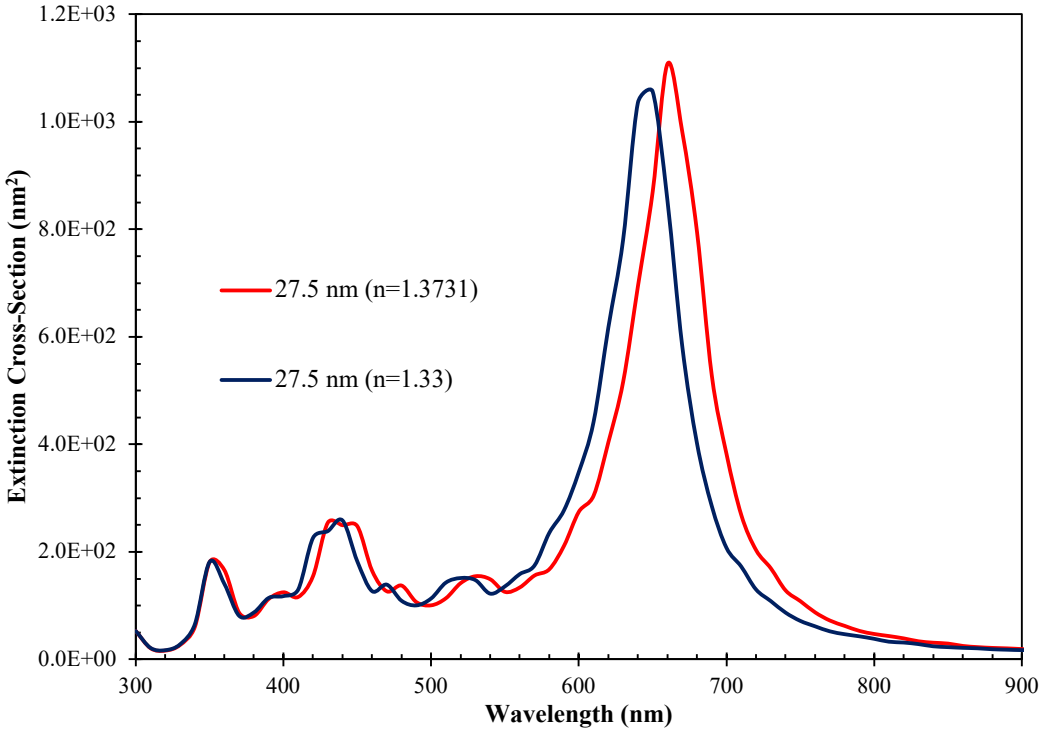

Figure 6.6: Effect of the medium's refractive index on the extinction cross-section spectra of a triangular AgNP with 27.5 nm edge length and 7 nm thickness.

6.4 Effect of Rotational Averaging

Because of the tumbling motion of AgNPs in solution, the direction of the electric field vector and the propagation vector of the incident light are constantly changing from the perspective of the nanoparticle. This motion can have a significant effect on the observed

extinction spectrum. Thus, the DDSCAT simulated spectra should be orientationally averaged to account for the experimental conditions of the AgNPs being in solution. Figure 6.7 shows a triangular nanoparticle with the three angles, θ, ϕ, and β, used in the DDSCAT program to define the orientation of the nanoparticle. In this figure, the lab coordinate system is defined by the x, y, and z axes, with the propagation direction of the incident light always taken to lie along the x direction. The target frame (i.e., the coordinate system that is fixed in the nanoparticle) is specified by the unit vectors $\hat{a}_2$, $\hat{a}_2$, and $\hat{a}_3$ ($\hat{a}_2$ is required to be perpendicular to $\hat{a}_1$, while $\hat{a}_3 \equiv \hat{a}_1$ x $\hat{a}_2$ and is not shown in the figure in order to reduce congestion). As the nanoparticle tumbles in solution, so does the target frame. With respect to the lab frame, the direction of â1 is determined by specifying the angles θ and ϕ, where $0 \leq \theta \leq 180$ and $0 \leq \phi \leq 360$. Note that in DDSCAT, θ is defined with respect to the x axis, so ϕ is the azimuthal angle in the yz plane. The orientation of the nanoparticle is then fully determined by specifying the angle, β, which is the azimuthal angle of rotation about the $\hat{a}_1$ axis ($0 \leq \beta \leq 360$).

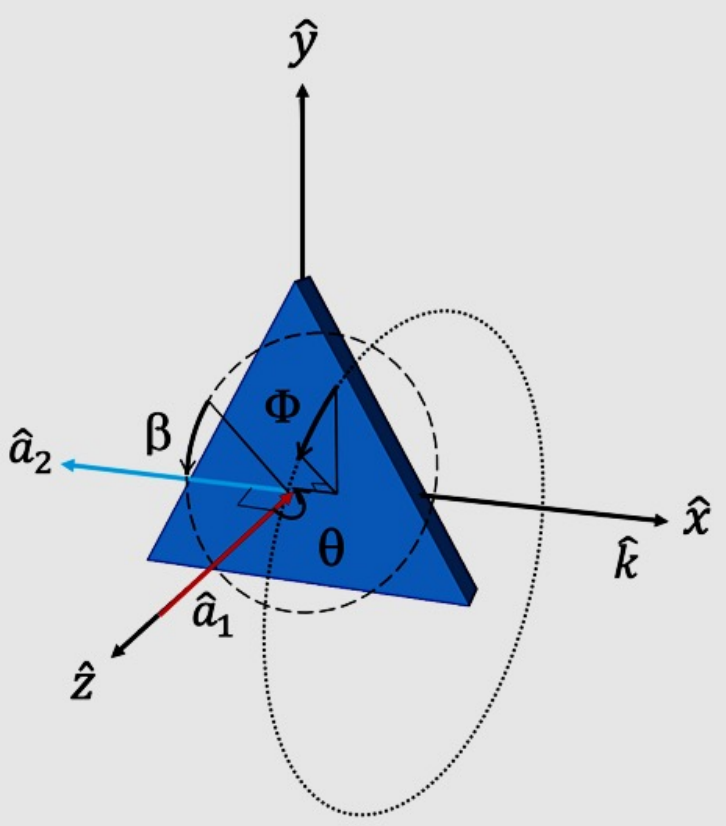

Figure 6.7: Diagram of a triangular AgNP shown in the lab frame. In this coordinate system â1, and â2, vectors are shown with corresponding θ, ϕ, and β angles.

An important practical question was how many orientations were needed to accurately calculate the spectra. So, before we started the calculations, we tested three sets of rotations to determine which one to use. The three sets contained 8, 64, and 512 orientations. The 8 rotations consisted of 2 values of β from 0 to 180° (45° and 135°), 2 of θ from 0 to 90° (41.41° and 75.52°), and 2 of ϕ from 0 to 180° (45° and 135°).

The 64 rotations consisted of 4 values of β from 0 to 180° (22.5°, 67.5°, 112.5°, and 157.5°), 4 of θ from 0 to 90° (28.96°, 51.32°, 67.98°, and 82.82°), and 4 of ϕ from 0 to 180° (22.5°, 67.5°, 112.5°, and 157.5°).

The 512 rotations consisted of 8 values of β from 0 to 180° (11.25°, 33.75°, 56.25°, 78.75°, 101.25°,123.75°, 146.25° and 168.75°), 8 of θ from 0 to 90° (20.36°, 35.66°, 46.57°, 55.77°, 64.06°, 71.79°, 79.19° and 86.42°), and 8 of ϕ from 0 to 180° (11.25°, 33.75°, 56.25°, 78.75°,

101.25°,123.75°, 146.25° and 168.75°). Note that symmetry considerations of the triangular shape enabled the ranges of ϕ and β given here to be smaller than the full ranges mentioned above. The results are shown in Figure 6.8 for nanotriangles having an edge length of 27.5 nm. As shown, 64 rotations provided the same results as 512 rotations while decreasing to 8 rotations altered the extinction cross-section. The main difference between 64 and 512 rotations was the time each calculation took, 306 hours for 512 rotations compared to 79 hours for 64 rotations.. The time for each calculation is not linear with the number of orientations because it was dependent on the particular scattering directions, θ and ϕ. Based on this information, we initially decided to use 64 rotations since it provided the same results as 512 rotations but took less time.

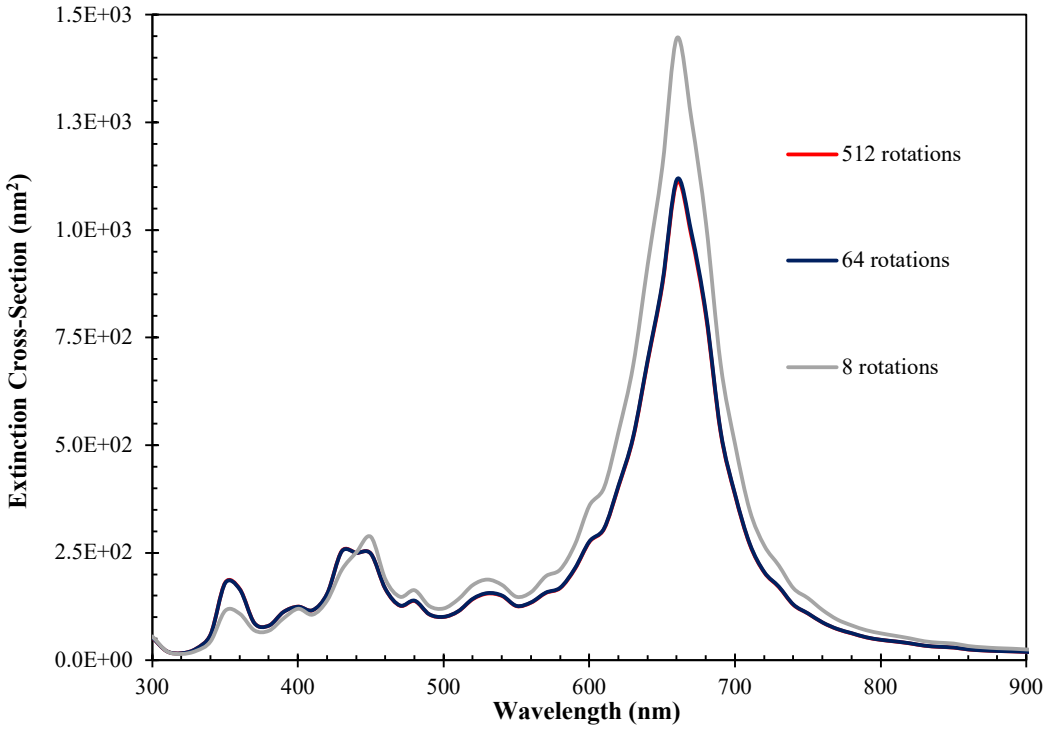

Figure 6.8: Results of changing the number of orientations used in averaging for a 27.5 nm edge length and 7 nm thickness silver nanoparticle. Note that the 64 and 512 rotation cases overlap one another within the resolution of this figure.

Using 64 rotations still proved to be a time-consuming task except for the smallest (12.5 nm edge length) nanotriangles, as each DDSCAT calculation took days to weeks for nanoparticles

with 22.5 nm to 60 nm edge lengths and would take months for edge lengths above 60 nm. As a result, we decided to search for a "magic angle" that would save time by cutting down on the number of angles needed to be sampled while still providing us the same results as using 64 rotations. After some research and trials, we determined that a magic angle of $\theta = 54.74^\circ$ [the root of the second-order Legendre polynomial, $P_2(\cos\theta) = (3\cos^2\theta - 1)/2$] and, because of symmetry considerations, only a single value of $\phi = 22.5^\circ$ was required, while 4 values of β from 0 to 180° were still needed. Thus, we were able to cut down on computation time by a factor of 64/4 = 16.

Figure 6.9 shows the orientationally-averaged spectrum of a 27.5 nm edge length and 7 nm thickness AgNP using 64 rotations compared to using the "magic angle" set of 4 rotations along with three non-orientationally-averaged spectra. These three spectra were computed for three geometries in which the nanotriangle is fixed in position relative to the incident light direction and the electric vector direction. Also, shown here is the effect of polarizing the light (see Figure 6.9 a, b and c), which was discussed in detail in Chapter 3. It is important to note that in DDSCAT, orientationally-averaged spectra automatically use unpolarized light. DDSCAT achieves this by calculating spectra for y- and z-polarized light and then averaging the results. As one can see, these four non-orientationally-averaged spectra are different from the rotationally averaged extinction cross-section spectra, and thus rotational averaging is important for simulating experimental UV-visible absorption spectra of AgNPs in solution.

As shown in Figure 6.9d, the extinction cross-section values in the orientationally-averaged spectrum and in the spectrum using the "magic angle" set of 4 rotations are almost identical, indicating that use of the magic angles does indeed work. Given that the results were favorable, we continued using this "magic angle" set to complete the calculations. This was particularly useful for the larger nanoparticles, 120 nm and above, as the calculation took days to weeks after applying the "magic angles". In the future, this "magic angle" could be used for irregularly shaped objects, especially to model large shapes as a time saving feature.

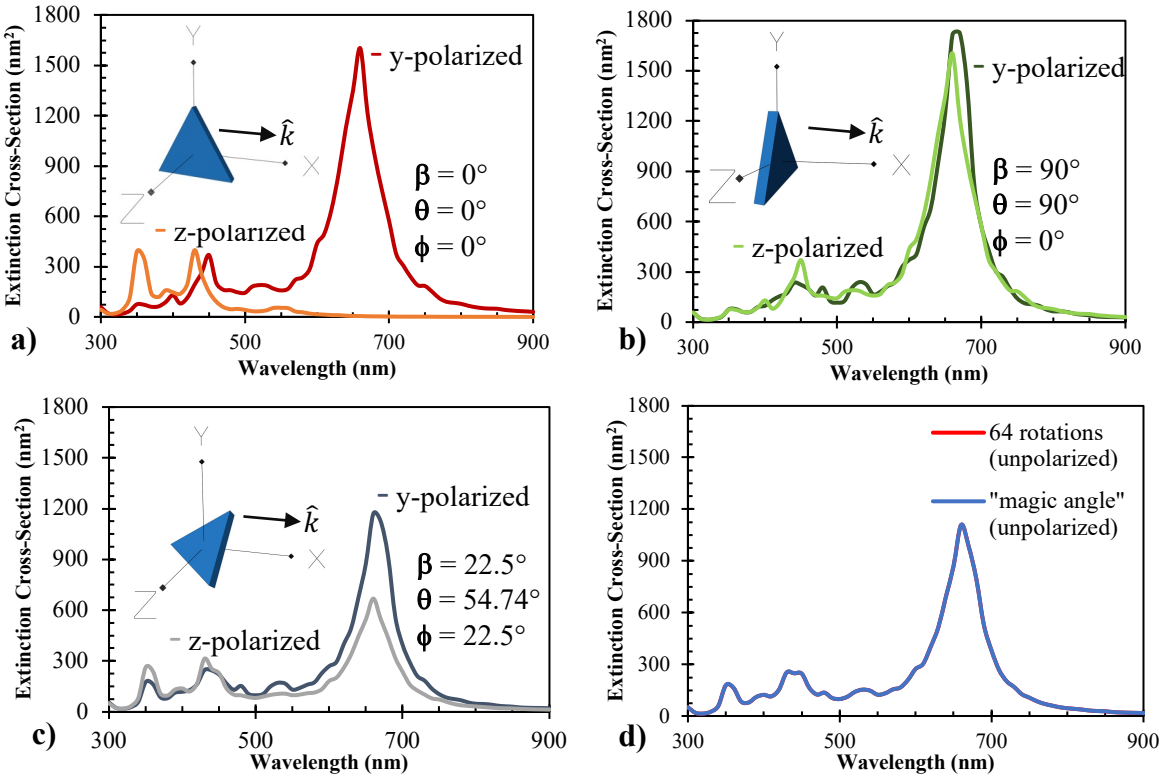

Figure 6.9: Results of using four non-orientationally-averaged spectra (a, b, and c) and 64 rotations compared to the "magic angle" set (d) on a 27.5 nm edge length and 7 nm thickness AgNP. Note that the 64 rotations and "magic angle" set cases overlap one another within the resolution of this figure.

6.5 Effect of Varying the Thickness and of "Snipping"

To determine the effect of thickness of a AgNP on the extinction cross-section, we simulated spectra for thicknesses of 6.0, 7.0 and 8.0 nm since the TEM images indicated a range of about 6 to 8 nm. The edge length chosen for these nanoparticles was 27.5 nm. Also, we simulated a snipped a AgNP of thickness 7.0 nm and 26 nm edge length since AgNPs found in solution are not perfectly triangular. A 27.5 nm AgNP was snipped, at the vertex, with small triangle of edge length 0.75 nm decreasing the edge length to 26 nm but keeping the thickness at 7.0 nm.

The results of having various thicknesses and of snipping are presented in Figure 6.10.

From the graph, the trend is that as the thickness of the nanoparticle decreases, the maximum extinction peak red shifts. As mentioned in Chapter 3 and by Hao and Schatz[14], the increase of aspect ratio (edge length / thickness) leads to the maximum extinction peaks to shift to higher wavelength, or in other words to red shift. As the thickness of the nanoparticle decreases, the aspect ratio increases. The aspect ratio when the thickness is 8.0 nm is 3.44 compared to 4.58 for a thickness of 6.0 nm. The trend may at first seem counterintuitive because typically, a peak will red shift as a molecule or nanoparticle becomes *larger*. The trend observed here can be crudely rationalized since the particle is "becoming more spherical" as it becomes thicker, and silver nanospheres absorb near 400 nm. Furthermore, this blue shift of the particle by "becoming more spherical" can also be explained with the results from the snipped nanoparticle. The snipped AgNP is a "more spherical" version of the 7.0 nm thickness. Comparing the extinction peak of the snipped 7.0 nm thickness (630 nm) with 7.0 nm (660 nm), the 7.0 nm thickness blue shifted by 30 nm. Other trend shown in the graph is the decrease in extinction cross section as the thickness decreases. A plausible explanation for this is that as the thickness decreases, the number of silver atoms (and therefore the number of conduction electrons) decreases, so there are fewer electrons contributing to the transition.

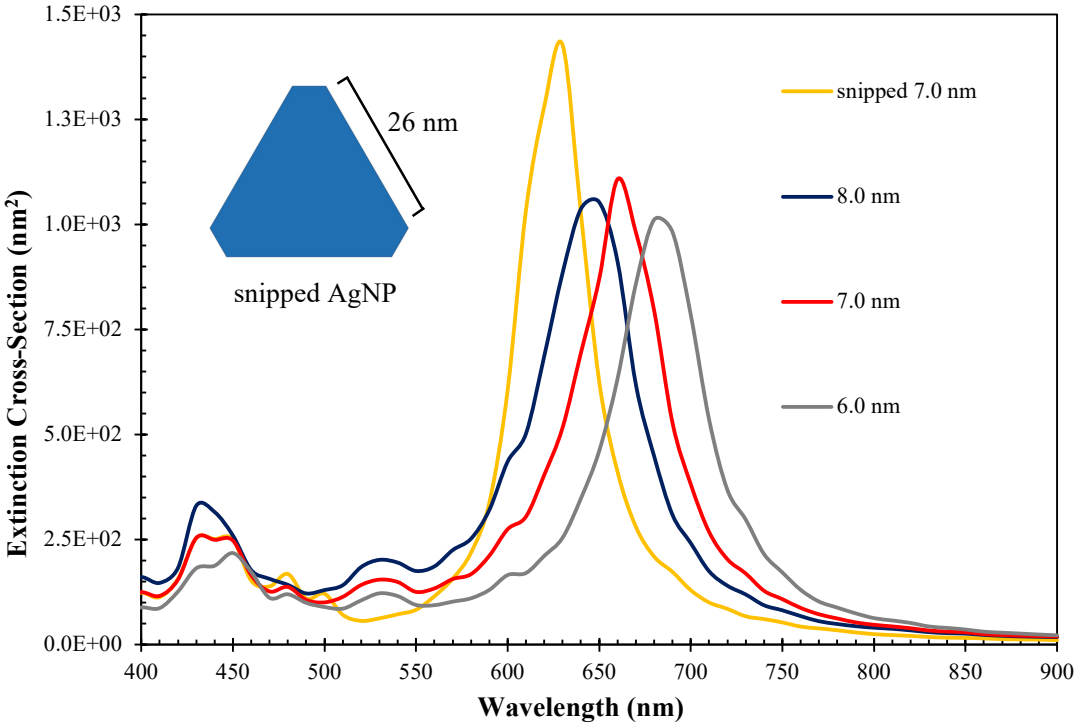

Figure 6.10: Extinction cross-section spectra of three thicknesses 8 nm (blue), snipped 7.0 nm (yellow), 7.0 nm (red) and 6.0 nm (gray) of a 27.5 nm edge length triangular AgNP. The refractive index of the medium was 1.37.

6.6 Extinction Cross-Section Results for Silver Nanoparticles

Using the histogram in Figure 6.1 as a guideline for AgNPs edge length sizes, we calculated the orientationally-averaged extinction cross-section of nanoparticles with edge lengths in the range of 12.5 to 207.5 nm, in increments of 5 nm. The thickness of the nanoparticles was 7 nm. Even though our histogram goes to an edge length of 310 nm, we stopped at 207.5 nm because for larger edge lengths, the number of dipoles exceeded the maximum limit of DDSCAT. The nanoparticles above 207.5 nm accounted for 8 out of the 214 nanoparticles in the histogram, and it will be shown later in the chapter that the limit of 207.5 nm edge length provided enough data to predict the absorption spectrum for edge lengths above 207.5 nm. Figure 6.11 provides the results of the extinction cross-section of the triangular AgNPs ranging from 12.5 nm to 207.5

nm in edge length and thickness of 7 nm. The figure is rather congested, so to show the trends with size more clearly, three specific sizes were selected, and their spectra are displayed in Figure 6.12.

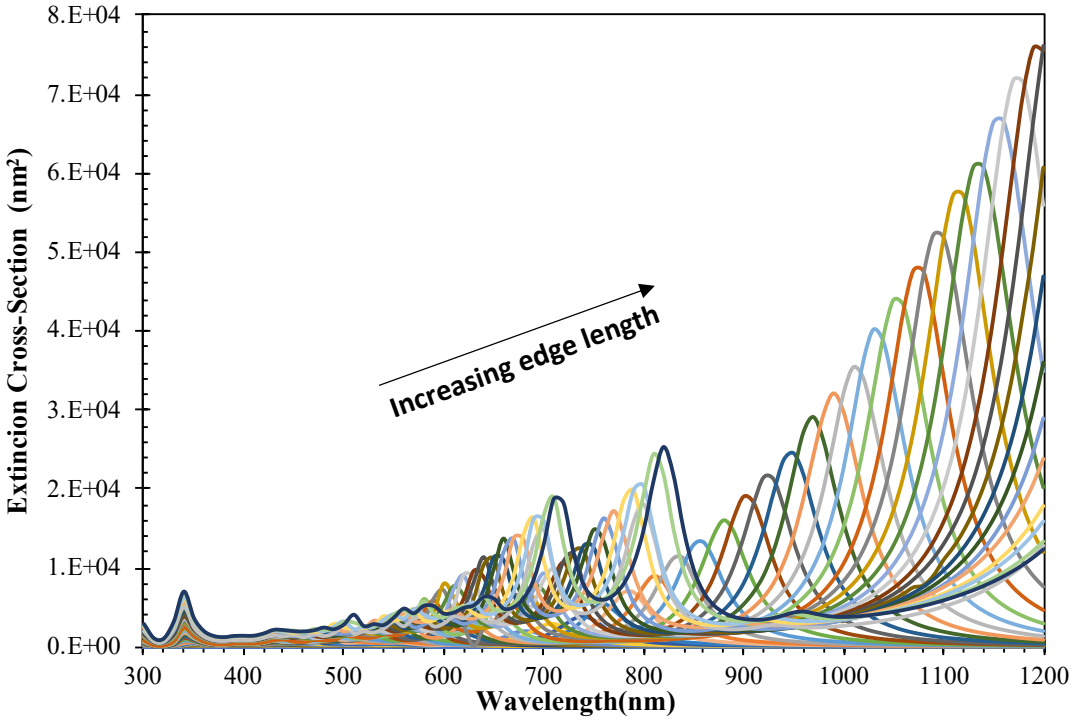

Figure 6.11: Results of extinction cross-section computations for triangular AgNPs having edge lengths of 12.5 to 207.5 nm and a thickness of 7 nm. The increment in size from one spectrum to the next is 5 nm. The refractive index of the medium was 1.37.

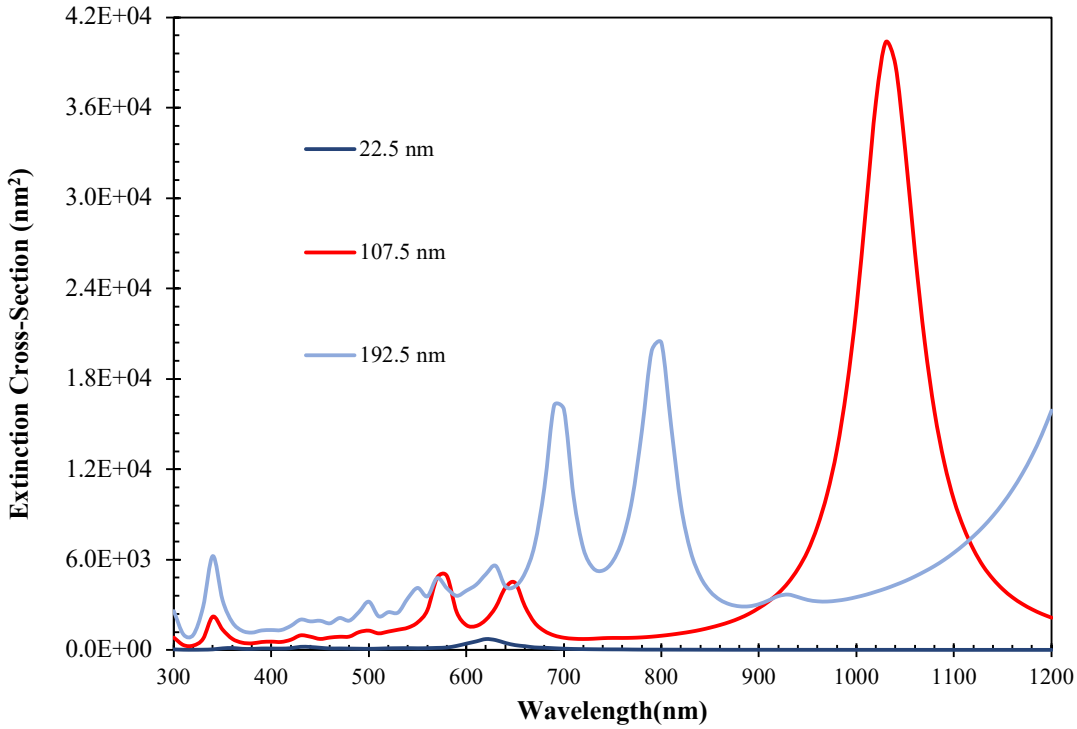

Figure 6.12: Results of extinction cross-section computations for triangular AgNPs having edge lengths of 22.5, 107.5 and 192.5 nm and a thickness of 7 nm. The refractive index of the medium was 1.37.

6.7 In-Plane and Out-of-Plane Dipole, in-Plane and Out-of-Plane Quadrupole Resonance Peaks

As mentioned in Chapter 3, in larger triangular AgNPs, in-plane and out-of-plane dipole and in-plane and out-of-plane quadrupole resonance peaks are excited and appear in the extinction cross-section spectrum. An example of a spectrum that contains these peaks is shown in Figure 6.13. Shown here are the three resonance peaks of a 97.5 nm edge length and 7 nm thickness AgNP. Using the extinction cross-section spectra for nanoparticles of edge lengths 12.5 to 207 .5 nm we wanted to determine trends in the magnitude, location, and widths of these peaks. Doing so allows the extinction spectra of very large nanoparticles (210 to 310 nm in edge length) to be estimated. These sizes were found in solution but are too large for DDSCAT to handle.

Using the multi-peak function of the data analysis program Igor Pro[15] and fitting the peaks with Lorentzian peak shapes, we were able to fit the four main peaks: in-plane and out-of-plane dipole and in-plane and out-of-plane quadrupole peaks. Equation 6.2 below gives the Lorentzian distribution function with the three fitting parameters: peak height, peak location and full width at half maximum (FWHM).

$$Lorentzian\ Distribution = I[\frac{\gamma^2}{(x-x_0{}^2)+\gamma^2}] \tag{6.2}$$

$$\mathbf{I} = Peak\ height$$

$$\boldsymbol{\gamma} = Half\ width\ at\ half\ maximum$$

$$\mathbf{x_0} = Peak\ location$$

An example of a spectrum in which the fours peaks are fitted with a Lorentzian is shown in Figure 6.13. In Figure 6.14, the best-fit values of the peak height, I, are plotted as a function of nanoparticle edge length for the in-plane and out-of-plane dipole, in-plane quadrupole, and out-of-plane quadrupole resonances. Similarly, Figure 6.15 shows the best-fit values of the peak locations, x0, while Figure 6.16 shows the best-fit values of the peak widths, FWHM.

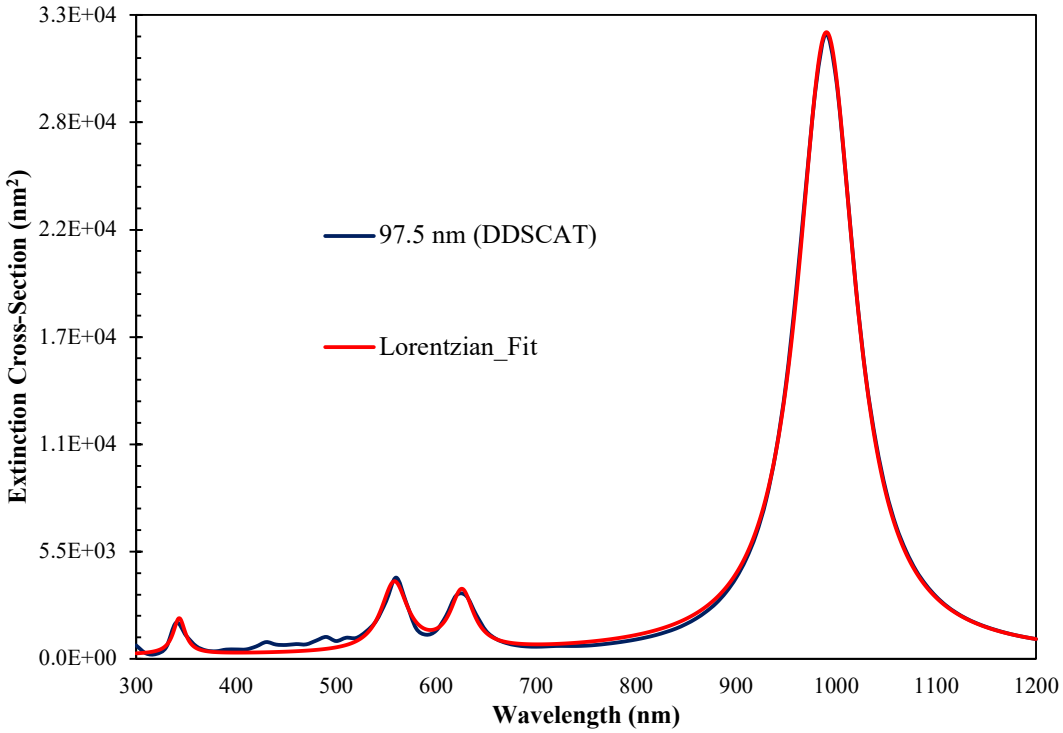

Figure 6.13: Extinction cross section spectrum of a 97.5 nm edge length and 7 nm thickness AgNP in solution compared to Lorentzian fit of spectrum.

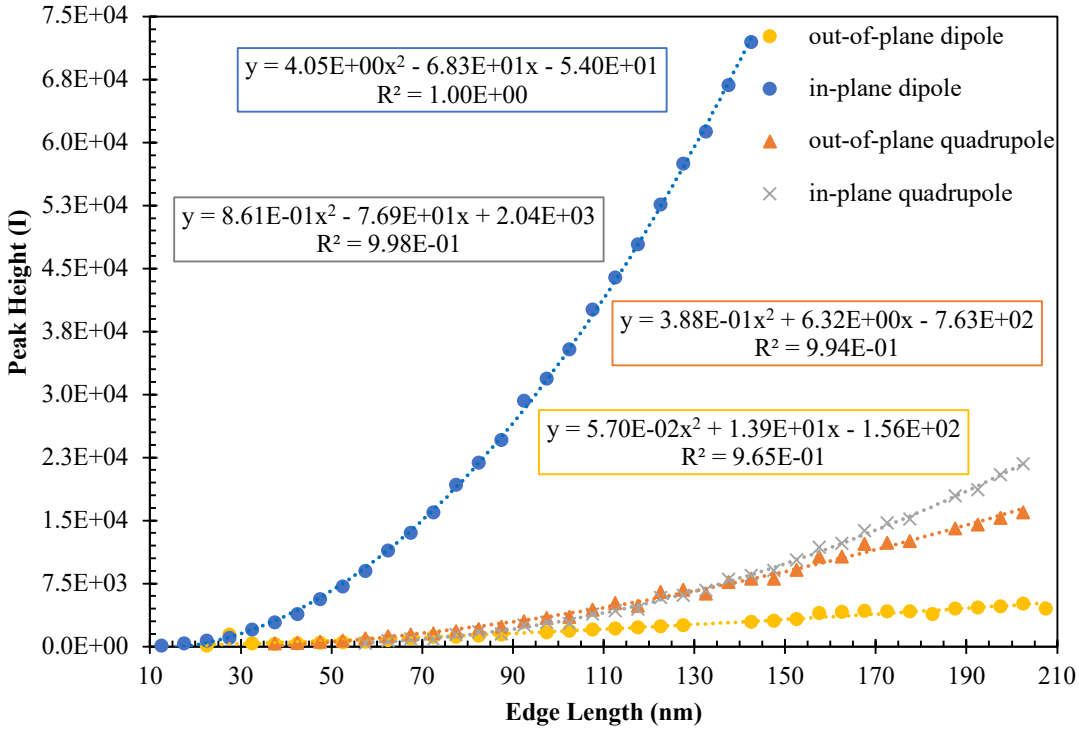

Figure 6.14: Extinction cross section peak heights for in-plane and out-of-plane dipole, in-plane quadrupole, and out-of-plane quadrupole resonance peaks of various sized silver nanoparticle in solution plotted as a function of edge length.

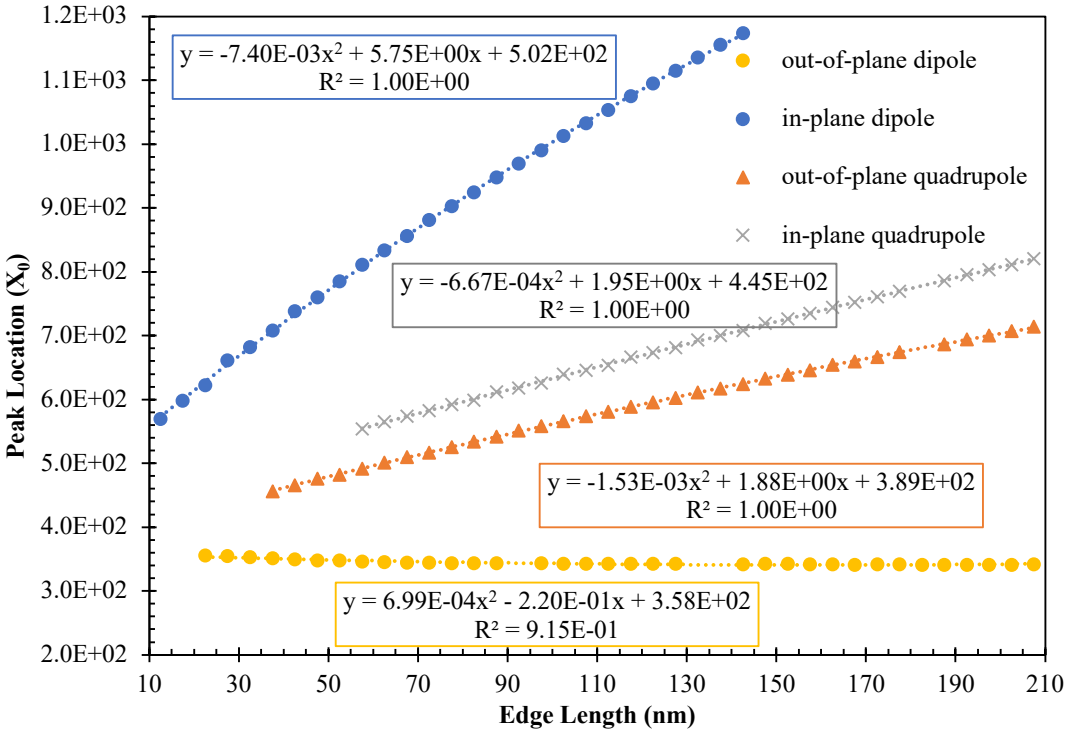

Figure 6.15: Extinction cross section peak heights for in-plane and out-of-plane dipole, in-plane and out-of-plane quadrupole resonance peaks of various sized silver nanoparticle in solution plotted as a function of edge length.

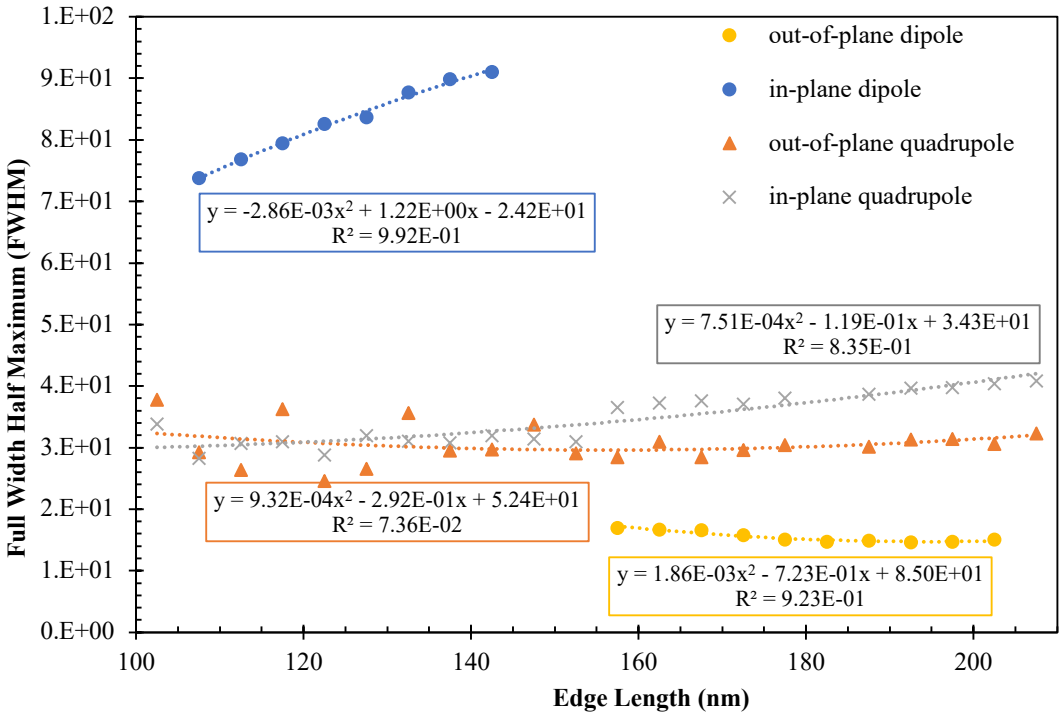

Figure 6.16: Full width half maximum of in-plane and out-of-plane dipole, in-plane quadrupole, and out-of-plane quadrupole resonance peaks of various sized silver nanoparticle in solution plotted as a function of edge length.

For each plot in Figures 6.14, 6.15 and 6.16, the trend in the data is quadratic. The functions with the best-fit coefficients and the coefficients of determination, R^2, are shown next to their corresponding data. As one can see, the R^2 values for the fits of peak height and position in Figures 6.14 and Figure 6.15 are > 0.97. Similarly, the R^2 values for the fit of peak width for the in-plane and out-of-plane dipole resonance in Figure 6.16 is > 0.92; however, the R^2 value was much lower for the widths of the out-plane and in-plane quadrupole resonances. The in-plane dipole plot for Figure 6.16 does not extend past the edge length size of 140 nm since cross-section peak after this edge length extends past the wavelength of 1200 nm. Using the quadratic functions, we were able to extrapolate the peak height, location, and width parameters to larger AgNPs (>207 nm) and thus estimate the spectra of these nanoparticles.

Once we obtained the extinction spectra for all the sizes, the next step was to use these spectra along with the histogram of the size distribution in Figure 6.1 to replicate the experimental

UV-visible absorption spectrum. The simulated spectrum was obtained by calculating the average over the computed spectra from all nanoparticles, weighted by their fractional population. Since the bin size of 25 nm in the histogram is rather coarse and, as Figure 6.11 indicates, the simulated spectra show a significant change when the size of the nanoparticle is changed by 25 nm, we decided to create an interpolated histogram by fitting the experimental histogram with a suitable function. In particular, we wanted values every 5 nm because we had computed spectra every 5 nm. The histogram was fitted with a Voigt function using the data analysis program Igor Pro. Other functions such as a Gaussian and Lorentzian were tested, but the Voigt function, which is a convolution of a Lorentzian distribution and a Gaussian distribution, provided the closest fit to the distribution values. The Voigt function in Igor has the form(Equation 6.3):

$$y_0 + \frac{2Area}{G_{fwhm}} \sqrt{\frac{ln(2)}{\pi}} * Voigt\ [\ \frac{2\sqrt{ln(2)}}{G_{fwhm}}(x - {x_0}^2),\ L_w/G_w * 2\sqrt{ln(2)}\ ] \quad (6.3)$$

$$\mathbf{Area} = The\ area\ under\ the\ peak\ excluding\ the\ vertical\ offset$$

$$\mathbf{y_0} = The\ vertical\ offset$$

$$\mathbf{G_{fwhm}} = The\ Gaussian\ full\ width\ at\ half\ maximum\ (FWHM)$$

$$\mathbf{Voigt} = Igor\ Pro's\ built-in\ function\ for\ calculating\ Voigt\ profiles$$

$$\mathbf{L_w/G_w} = The\ ratio\ of\ the\ Lorentzian\ and\ Gaussian\ components\ W_L/W_G$$

The best-fit values of the coefficients are: y_0= 0.0089 $\pm$ 0.0234, Area =5.9 $\pm$ 0.2, x_0 =25 $\pm$ 1, G_{fwhm} =3.7 $\pm$ 23 and L_w/G_w =4.2 $\pm$ 29. A plot of the fitted function is shown in Figure 6.17.

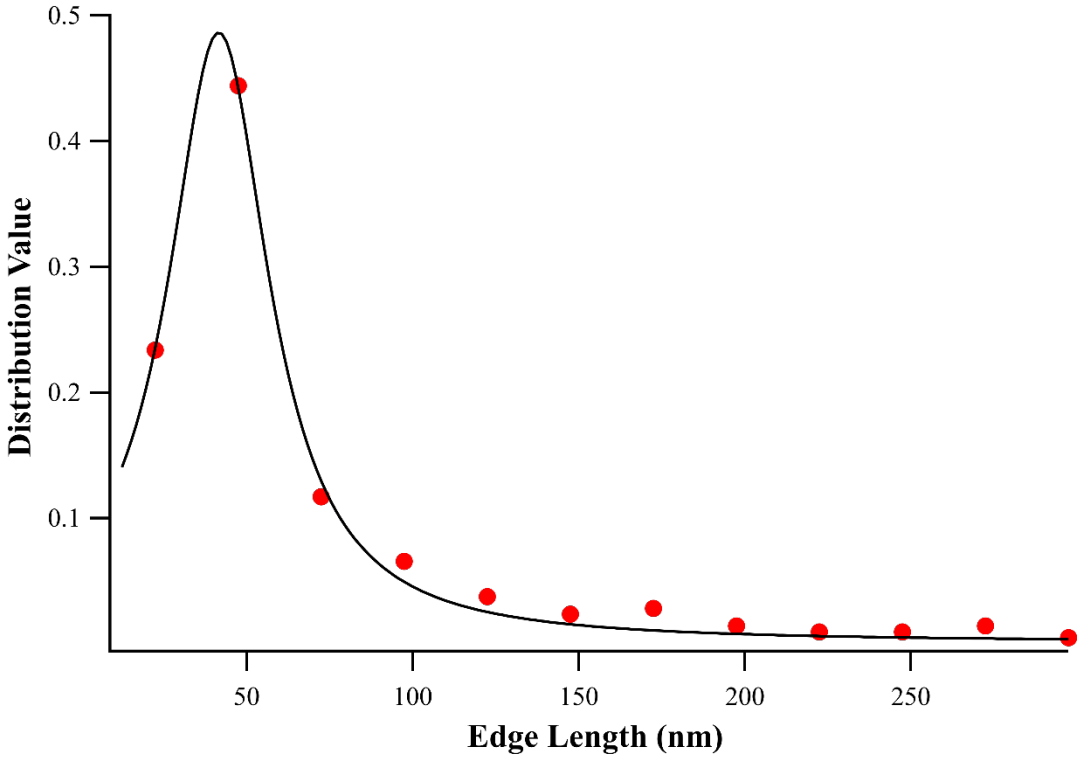

Figure 6.17: Plot of the distribution of number of nanoparticles over the edge length fitted using the data analysis program Igor.

The next step was to multiply the calculated extinction cross-sectional value for each edge length from 300 to 1200 nm by the corresponding Voigt distribution value for that edge length. The final step was to add the obtained extinction cross-section value at every 10 nm as shown in Equation 6.4.

$$Total\ Extinction\ Cross-Section = \sum_{size=12.5}^{307.5} C_{ext(DDSCAT)} * D \qquad (6.4)$$

$$\mathbf{C_{ext(DDSCAT)}} = DDSCAT\ extinction\ cross-section$$

$$\mathbf{D} = Voigt\ distribution\ for\ each\ edge\ length$$

The result is shown in Figure 6.18 along with the experimental UV-visible spectrum of

the solution where the y-axes were scaled so that the peak heights matched. Broadly speaking, the simulation reproduces the experimental spectrum. They both show a peak at about 340 nm. However, the large peak near 700 nm in the DDSCAT plot is red shifted 80 nm and does not decline in intensity as rapidly as the experimental peak. Several factors likely contribute to the differences. 1)For all the calculations, we used a nanoparticle thickness of 7 nm but as shown in Figure 6.10, an increase of 0.5 nm in thickness leads to a blue shift in the peak, 2) The shapes of the nanoparticles are not all perfectly triangular, and some appear to have their vertices "snipped", causing a blue shift as shown in Figure 6.10, 3) The size distribution obtained from TEM data is based on 214 nanoparticles and may not be fully representative of the true size distribution. Larger nanoparticles have increasingly larger extinction cross-sections. Because the graininess of the distribution becomes more pronounced at larger edge lengths, the contribution of these nanoparticles may be misrepresented to some degree and 4) The refractive index of the medium in the vicinity of the nanoparticle surface is not fully known, and 5) the DDSCAT simulation is classical in nature.

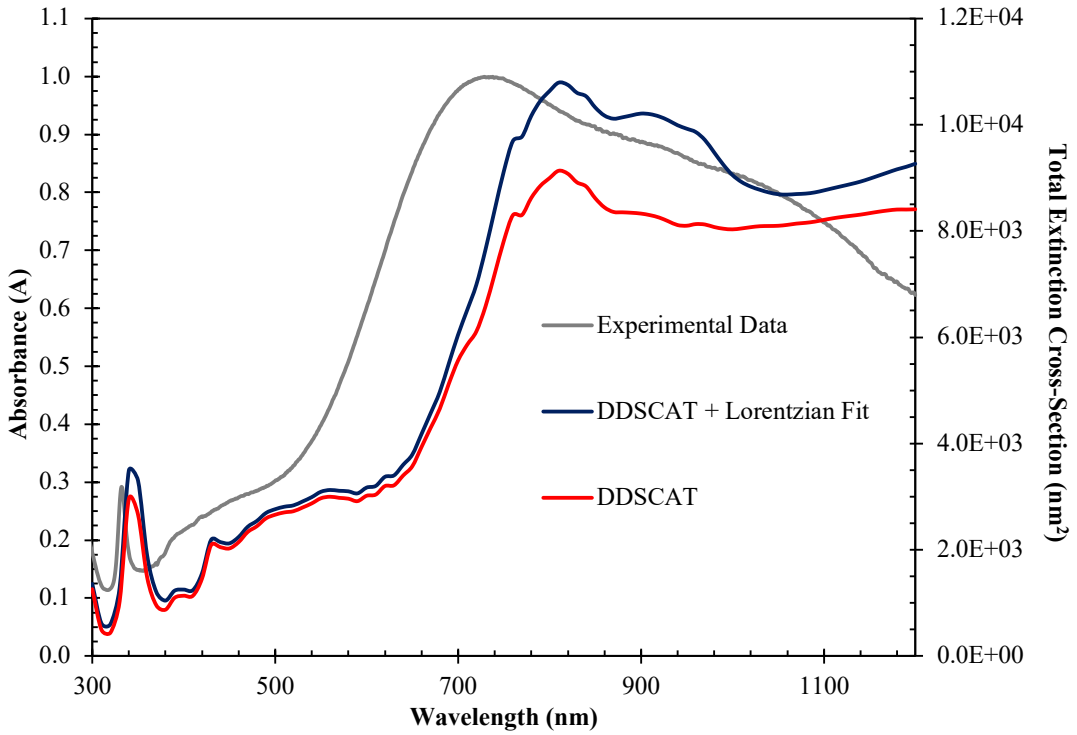

Figure 6.18: DDSCAT and DDSCAT + Lorentzian Fit results for a AgNP solution compared to the UV-Visible spectrum of the same solution.

Based on the spectra in Figure 6.10 showing that increasing the edge thickness from 7 to 8 nm and snipping the vertices by a small amount can blue shift the spectra by several tens of nm, we suspect that these two factors can account for a significant portion of the discrepancy between the experimental and simulated spectra in Figure 6.18. The small variation in thicknesses and in shapes observed in the TEM images lends support to this claim. While the experimental and simulated spectra in Figure 6.18 are in semi-quantitative agreement, including all possible thicknesses and shapes in the simulated spectrum would likely further improve the agreement but at the expense of a large increase in computational resources.

6.8 Conclusion

In conclusion, we successfully used DDSCAT to simulate the UV-visible extinction spectrum of triangular AgNPs that were synthesized in solution in our lab. To ensure that the calculations resembled the experimental conditions, several factors were taken into account: the optical dielectric function of silver, the medium's refractive index, rotational averaging due to the nanoparticles tumbling motion in solution, and the experimentally-determined size distribution.

6.9 Acknowledgements

Chapter 6 contains material that is being prepared for a publication. Yamamoto, N; Torres, M; Harris, D,; Pullman, D.P. "Seedless, one-pot synthesis of infrared-absorbing silver nanoparticles". *Manuscript in preparation*. I would like Nobu Yamamoto for his work on this project.

6.10 References

1. Draine, B. T.; Flatau, P. J. Discrete-Dipole Approximation For Scattering Calculations. *Journal of the Optical Society of America A* **1994**, *11* (4), 1491-1499.

2. Hao, E.; Schatz, G. C. Electromagnetic Fields around Silver Nanoparticles and Dimers. *The Journal of Chemical Physics* **2004**, *120* (1), 357-366.

3. Yang, W.; Schatz, G. C.; Van Duyne, R. P. Discrete Dipole Approximation for Calculating Extinction and Raman Intensities for Small Particles with Arbitrary Shapes. *The Journal of Chemical Physics* **1995**, *103* (3), 869-875.

4. Sureka A.; Santhanam V. Optical Properties of Metal Nanoparticles Using DDA, *Journal of Young Investigators* **2013**, *25* (4), 66-72.

5. Song, K. C.; Lee, S. M.; Park, T. S.; Lee, B. S. Preparation of Colloidal Silver Nanoparticles by Chemical Reduction Method. *Korean Journal of Chemical Engineering* **2009**, *26* (1), 153-155.

6. Panzarasa, G. Just What Is It That Makes Silver Nanoprisms so Different, so Appealing? *Journal of Chemical Education* **2015**, *92* (11), 1918-1923.

7. Yamamoto, N. From Bismuth Nitrogen Molecules to Silver Nanoparticles: A Bottom-Up Approach to Materials Chemistry and Applications. dissertation, San Diego State University: San Diego, CA, 2019, pp 185-245.

8. Community, B. O. (2018). Blender - a 3D modelling and rendering package. Stitching Blender Foundation, Amsterdam. Retrieved from http://www.blender.org

9. Sobh, A. N.; White, S.; Smith, J.; Sobh, N.; Jain, P. K. Nanoddscat+. https://nanohub.org/resources/ddaplus, 2019

10. Lynch, D. W.; Hunter W. in Handbook of Optical Constants of Solids, edited by Palik, E. D., Academic Press, Burlington, 1998, 275-367.

11. Johnson, P. B.; Christy, R. W. Optical Constants of the Noble Metals. *Physical Review B* **1972**, *6* (12), 4370-4379.

12. Green, M. A. Self-Consistent Optical Parameters of Intrinsic Silicon at 300K Including Temperature Coefficients. *Solar Energy Materials and Solar Cells* **2008**, *92* (11), 1305–1310.

13. Harris N., Blaber M. G., and Schatz G. C., Optical Properties of Metal Nanoparticles, in

Encyclopedia of Nanotechnology, Bhushan, B. (ed), Springer; Dordrecht, 2012, pp 1950-1969

14. Hao, E.; Schatz, G. C. Electromagnetic Fields around Silver Nanoparticles and Dimers. *The Journal of Chemical Physics* **2004**, *120* (1), 357-366.

15. Igor Pro, version 6.37; WaveMetrics, Inc., Lake Oswego, OR.

Appendix A

DDSCAT Files

Example Parameter File for DDSCAT

```
' ========= Parameter file for v7.3 ==================='

        '**** Preliminaries ****'
'NOTORQ' = CMTORQ*6 (DOTORQ, NOTORQ) – either do or skip torque calculations
'PBCGS2' = CMDSOL*6 (PBCGS2, PBCGST, GPBICG, QMRCCG, PETRKP) – CCG method
'FFTMKL' = CMETHD*6 (GPFAFT, FFTMKL) – FFT method
'GKDLDR' = CALPHA*6 (GKDLDR, LATTDR, FLTRCD) – DDA method
'NOTBIN' = CBINFLAG (NOTBIN, ORIBIN, ALLBIN) – specify binary output
'**** Initial Memory Allocation ****'
56  48  12 = dimensioning allowance for target generation

        '**** Target Geometry and Composition ****'
'FROM_FILE' = CSHAPE*9 shape directive
0.0  0.0  0.0 = shape parameters 1 - 3
1  = NCOMP = number of dielectric materials
'/home/mzepeda/ddscat/Ag_Green.txt' = file with refractive index 1

        '**** Additional Nearfield calculation? ****'
0  = NRFLD (=0 to skip nearfield calc., =1 to calculate nearfield E)
0.5  0.5  0.5 0.5 0.5 0.5 (fract. extens. of calc. vol. in -x,+x,-y,+y,-z,+z)
'**** Error Tolerance ****'
1e-5 = TOL = MAX ALLOWED (NORM OF |G>=AC|E> −ACA|X>)/(NORM OF AC|E>)
```

```
'**** maximum number of iterations allowed ****'
10000000 = MXITER

        '**** Interaction cutoff parameter for PBC calculations ****'
1e-2 = GAMMA (1e-2 is normal, 3e-3 for greater accuracy)

        '**** Angular resolution for calculation of <cos>, etc. ****'
0.5  = ETASCA (number of angles is proportional to [(3+x)/ETASCA]^2)

        '**** Vacuum wavelengths (micron) ****'
0.3  1.2  91 'LIN' = wavelengths (first,last,how many,how=LIN,INV,LOG)
        '**** Refractive index of ambient medium'
1.3731  = NAMBIENT

        '**** Effective Radii (micron) **** '
0.0148862574751  0.0148862574751  1 'LIN' = aeff (first,last,how many,how=LIN,INV,LOG)

        '**** Define Incident Polarizations ****'
(0,0) (1,0) (0,0) = Polarization state e01 (k along x axis)
2  = IORTH (=1 to do only pol. state e01; =2 to also do orth. pol. state)

        '**** Specify which output files to write ****'
0  = IWRKSC (=0 to suppress, =1 to write ".sca" file for each target orient.

        '**** Prescribe Target Rotations ****'
0.0  180.0  4 = BETAMI, BETAMX, NBETA (beta=rotation around a1)
54.74  54.74  1 = THETMI, THETMX, NTHETA (theta=angle between a1 and k)
22.5  22.5  1 = PHIMIN, PHIMAX, NPHI (phi=rotation angle of a1 around k)

        '**** Specify first IWAV, IRAD, IORI (normally 0 0 0) ****'
0 0 0 = first IWAV, first IRAD, first IORI (0 0 0 to begin fresh)

        '**** Select Elements of S_ij Matrix to Print ****'
6 = NSMELTS = number of elements of S_ij to print (not more than 9)
11 12 21 22 31 41 = indices ij of elements to print

        '**** Specify Scattered Directions ****'
LFRAME = CMDFRM (LFRAME, TFRAME for Lab Frame or Target Frame)
1  = NPLANES = number of scattering planes
0. 0. 180. 1 = phi, thetan_min, thetan_max (deg) for plane A
```

Example Shape File for DDSCAT

```
 >PIPOBJ: point-in-polyhedron: NBX, NBY, NBZ= 55  47  12
15516 = NAT
1.0000 0.0000 0.0000 = A_1 vector
0.0000 1.0000 0.0000 = A_2 vector
1.000000 1.000000 1.000000 = lattice spacings (d_x,d_y,d_z)/d
0.0 0.0 0.0
JA  IX  IY  IZ  ICOMP(x,y,z)
1  -14  1  -5  1 1 1
2  0  -23  -5  1 1 1
3  -13  1  -5  1 1 1
4  -12  1  -5  1 1 1
5  -11  1  -5  1 1 1
6  -12  -3  -5  1 1 1
7  -10  1  -5  1 1 1
8  -11  -3  -5  1 1 1
9  -9  1  -5  1 1 1
10  -10  -3  -5  1 1 1
11  -8  1  -5  1 1 1
12  -9  -3  -5  1 1 1
13  -7  1  -5  1 1 1
14  -8  -3  -5  1 1 1
15  -6  1  -5  1 1 1
16  -7  -3  -5  1 1 1
17  -5  1  -5  1 1 1
18  -6  -3  -5  1 1 1
19  -4  1  -5  1 1 1
20  -5  -3  -5  1 1 1
21  -3  1  -5  1 1 1
22  -4  -3  -5  1 1 1
23  -2  1  -5  1 1 1
24  -3  -3  -5  1 1 1
25  -1  1  -5  1 1 1
26  -2  -3  -5  1 1 1
27  0  1  -5  1 1 1
28  -1  -3  -5  1 1 1
29  1  1  -5  1 1 1
30  0  -3  -5  1 1 1
31  2  1  -5  1 1 1
32  1  -3  -5  1 1 1
```

```
33  3  1  -5  1 1 1
34  2  -3  -5  1 1 1
35  4  1  -5  1 1 1
36  3  -3  -5  1 1 1
37  5  1  -5  1 1 1
38  4  -3  -5  1 1 1
39  6  1  -5  1 1 1
40  5  -3  -5  1 1 1
41  7  1  -5  1 1 1
42  6  -3  -5  1 1 1
43  8  1  -5  1 1 1
44  7  -3  -5  1 1 1
45  9  1  -5  1 1 1
46  8  -3  -5  1 1 1
47  10  1  -5  1 1 1
48  9  -3  -5  1 1 1
49  11  1  -5  1 1 1
50  10  -3  -5  1 1 1
......
15516  25  20  6  1 1 1
```

Example Optical Dielectric Function File for DDSCAT

```
 Ag  Silver  (Green,  DOI:  10.103/srep30605)
1  2  3  0  0  =  columns  for  wave,  Re(n),  Im(n),  eps1,  eps2
wave(um)  Re(n)  Im(k)  eps1  eps2
0.300  1.619  0.591  2.2720  1.9145
0.301  1.612  0.558  2.2872  1.7988
0.302  1.602  0.523  2.2934  1.6768
0.303  1.590  0.487  2.2892  1.5493
0.304  1.574  0.450  2.2732  1.4175
0.305  1.554  0.413  2.2441  1.2827
0.306  1.530  0.375  2.2009  1.1469
0.307  1.502  0.337  2.1426  1.0123
0.308  1.469  0.300  2.0689  0.8814
0.309  1.432  0.264  1.9799  0.7572
0.310  1.389  0.231  1.8763  0.6427
0.311  1.342  0.202  1.7596  0.5411
0.312  1.290  0.177  1.6323  0.4555
0.313  1.234  0.158  1.4978  0.3887
0.314  1.176  0.146  1.3608  0.3429
```

0.315 1.117 0.143 1.2280 0.3199
0.316 1.065 0.149 1.1122 0.3164
0.317 1.018 0.155 1.0134 0.3150
0.318 0.974 0.161 0.9237 0.3135
0.319 0.932 0.167 0.8405 0.3121
0.320 0.890 0.174 0.7623 0.3106
0.321 0.849 0.182 0.6880 0.3092
0.322 0.808 0.190 0.6171 0.3077
0.323 0.767 0.200 0.5489 0.3063
0.324 0.726 0.210 0.4831 0.3048
0.325 0.684 0.222 0.4194 0.3033
0.326 0.642 0.235 0.3576 0.3018
0.327 0.600 0.250 0.2973 0.3003
0.328 0.557 0.268 0.2384 0.2989
0.329 0.514 0.289 0.1809 0.2974
0.330 0.472 0.313 0.1245 0.2959
0.331 0.431 0.342 0.0691 0.2944
0.332 0.392 0.373 0.0147 0.2929
0.333 0.357 0.408 -0.0389 0.2914
0.334 0.326 0.445 -0.0916 0.2900
0.335 0.299 0.483 -0.1437 0.2885
0.336 0.276 0.521 -0.1951 0.2870
0.337 0.256 0.558 -0.2459 0.2856
0.338 0.239 0.594 -0.2962 0.2841
0.339 0.225 0.630 -0.3459 0.2827
0.340 0.212 0.663 -0.3952 0.2813
0.341 0.201 0.696 -0.4440 0.2799
0.342 0.191 0.727 -0.4925 0.2784
0.343 0.183 0.758 -0.5405 0.2770
0.344 0.175 0.787 -0.5883 0.2756
0.345 0.168 0.815 -0.6356 0.2743
0.346 0.162 0.842 -0.6827 0.2729
0.347 0.156 0.868 -0.7296 0.2715
0.348 0.151 0.894 -0.7761 0.2702
0.349 0.146 0.919 -0.8225 0.2689
0.350 0.142 0.943 -0.8686 0.2676
.....
2.000 0.510 13.966 -194.7791 14.2588

Appendix B

Arduino Code

Arduino Code for Measuring I-V Curves

```
 //the relays connect to
int IN1 = 22;
int IN2 = 23;
int IN3 = 24;
int IN4 = 25;
int IN5 = 26;
int IN6 = 27;
int IN7 = 28;
int IN8 = 29;
int IN9 = 40;
int IN10 = 41;
int IN11 = 42;
int IN12 = 43;
int IN13 = 44;
int IN14 = 45;
int IN15 = 46;
int IN16 = 47;

        #define BIT_0 0 // 0 = 00 0000
#define BIT_1 1 // 1 = 00 0001
#define BIT_2 2 // 2 = 00 0010
#define BIT_3 4 // 4 = 00 0100
```

```
#define BIT_4 8 // 8 = 00 1000
#define BIT_5 16 // 16 = 01 0000
#define BIT_6 32 // 32 = 10 0000
#define BIT_7 64 // 64 = 100 0000
#define BIT_8 128 // 128 = 1000 0000

        #define ON 0
#define OFF 1

        int value2 = 0;
int value = 0;
int value3 = 0;
int value4 = 0;

        int inputPin1 = A1;
int inputPin = A0;

        float current = 0;
float voltage = 0;
float resistance = 0;

        float sensorValue = 0;
float sensorValue2 = 0;

        int numReadings = 30;

        float analogread = 0;
float analogread1 = 0;
float analogread2 = 0;
float analogread3 = 0;

        void setup()

        {
relay_init();//initialize the relay
// initialize serial communication at 9600 bits per second:
Serial.begin(9600); Serial.println ();
}

        void relay_init(void)//initialize the relay
{
//set all the relays OUTPUT
pinMode(IN1, OUTPUT);
```

```
pinMode(IN2, OUTPUT);
pinMode(IN3, OUTPUT);
pinMode(IN4, OUTPUT);
pinMode(IN5, OUTPUT);
pinMode(IN6, OUTPUT);
pinMode(IN7, OUTPUT);
pinMode(IN8, OUTPUT);
pinMode(IN9, OUTPUT);
pinMode(IN10, OUTPUT);
pinMode(IN11, OUTPUT);
pinMode(IN12, OUTPUT);
pinMode(IN13, OUTPUT);
pinMode(IN14, OUTPUT);
pinMode(IN15, OUTPUT);
pinMode(IN16, OUTPUT);

        digitalWrite(IN1, 1);
digitalWrite(IN2, 1);
digitalWrite(IN3, 1);
digitalWrite(IN4, 1);
digitalWrite(IN5, 1);
digitalWrite(IN6, 1);
digitalWrite(IN7, 1);
digitalWrite(IN8, 1);
digitalWrite(IN9, 1);
digitalWrite(IN10, 1);
digitalWrite(IN11, 1);
digitalWrite(IN12, 1);
digitalWrite(IN13, 1);
digitalWrite(IN14, 1);
digitalWrite(IN15, 1);
digitalWrite(IN16, 1);
}

        // the loop routine runs over and over again forever:
void loop() {

        outWrite();

        }

        void outWrite() {
```

```
        { digitalWrite(IN1, OFF);
digitalWrite(IN10, ON);
digitalWrite(IN11, ON);
digitalWrite(IN12, ON);
digitalWrite(IN13, ON);
digitalWrite(IN14, ON);
digitalWrite(IN15, ON);
digitalWrite(IN16, ON);

        delay(1000);

        // read the input on analog A0 and A1:

        for(int k = 0; k < numReadings; k++) {
analogread1 = analogRead(inputPin1);
value4 = value4 + analogread1;
analogread = analogRead(inputPin);
value3 = value3 + analogread;
}
value4 = value4 / numReadings;

        value3 = value3 / numReadings;

        // Convert the analog reading (which goes from 0 - 1023) to a voltage
(0 - 5V):
current = value4 * ((5.0/150.0) / 1023.0)*1000.0;

        // Convert the analog reading (which goes from 0 - 1023) to a voltage
(0 - 5V, Amp gain is 8.5:
voltage = value3 * ((5.0/8.5) / 1023.0);

        resistance = voltage* 1000 / current;

        // print out the value you read:Serial.print (", current = ");
Serial.print( voltage, 3); Serial.print (','); Serial.print(current, 3);
Serial.print (','); Serial.println(resistance, 3);
delay (1);

        }
{
digitalWrite(IN10, OFF);
digitalWrite(IN11, OFF);
digitalWrite(IN12, OFF);
```

```
digitalWrite(IN13, OFF);
digitalWrite(IN14, OFF);
digitalWrite(IN15, OFF);
digitalWrite(IN16, OFF);

        delay(1000);

        digitalWrite(IN2, ON);
digitalWrite(IN3, ON);
digitalWrite(IN4, ON);
digitalWrite(IN5, ON);
digitalWrite(IN6, ON);
digitalWrite(IN7, ON);
digitalWrite(IN8, ON);
digitalWrite(IN9, ON);

        delay (2000); //delay for the reading

        // read the input on analog A0 and A1:

        analogread3 = analogRead(inputPin1);
analogread2 = analogRead(inputPin);

        // Convert the analog reading (which goes from 0 - 1023) to a voltage
(0 - 5V):
current = analogread3 * ((5.0/150.0) / 1023.0)*1000.0;

        // Convert the analog reading (which goes from 0 - 1023) to a voltage
(0 - 5V, Amp gain is 8.5:
voltage = analogread2 * ((5.0/8.5) / 1023.0);

        // print out the value you read:Serial.print (", current = ");
Serial.print( voltage, 3); Serial.print (',');  Serial.println(current, 3);

        delay (1);
}
{
digitalWrite(IN1, ON);

        for(int i = 0; i <256; i++) {

        if(BIT_1 & i) {
digitalWrite(IN2, ON);
```

```
} else {
digitalWrite (IN2, OFF);
}

        if(BIT_2 & i) {
digitalWrite(IN3, ON);
} else {
digitalWrite (IN3, OFF);
}

        if(BIT_3 & i) {
digitalWrite(IN4, ON);
} else {
digitalWrite (IN4, OFF);
}

        if(BIT_4 & i) {
digitalWrite(IN5, ON);
} else {
digitalWrite (IN5, OFF);
}

        if(BIT_5 & i) {
digitalWrite(IN6, ON);
} else {
digitalWrite (IN6, OFF);
}

        if(BIT_6 & i) {
digitalWrite(IN7, ON); } else { digitalWrite (IN7, OFF);
}

        if(BIT_7 & i) {
digitalWrite(IN8, ON);
} else {
digitalWrite (IN8, OFF);
}
if(BIT_8 & i) {
digitalWrite(IN9, ON);
} else { digitalWrite (IN9, OFF);
}
delay (1000); //delay for the resistors
```

```
        // read the input on analog pin 1:

        for(int j = 0; j < numReadings; j++) { sensorValue2 = analogRead(inputPin1); value2 =
value2 + sensorValue2; sensorValue = analogRead(inputPin); value = value + sensorValue;
}
value2 = value2 / numReadings;

        value = value / numReadings;

        // Convert the analog reading (which goes from 0 - 1023) to a voltage
(0 - 5V): current = value2 * ((5.0/150.0) / 1023.0)*1000.0;

        // Convert the analog reading (which goes from 0 - 1023) to a voltage
(0 - 5V, Amp gain is 8.5:
voltage = value * ((5.0/8.5) / 1023.0);

        resistance = voltage* 1000 / current;

        // print out the value you read:Serial.print (", current = ");
Serial.print( voltage, 3); Serial.print (',');  Serial.print(current, 3);
Serial.print (','); Serial.println(resistance, 3);
delay (1);
        }
{
digitalWrite(IN1, ON);
digitalWrite(IN2, OFF);
digitalWrite(IN3, OFF);
digitalWrite(IN4, OFF);
digitalWrite(IN5, OFF);
digitalWrite(IN6, OFF);
digitalWrite(IN7, OFF);
digitalWrite(IN8, OFF);
digitalWrite(IN9, OFF);
digitalWrite(IN10, OFF);
digitalWrite(IN11, OFF);
digitalWrite(IN12, OFF);
digitalWrite(IN13, OFF);
digitalWrite(IN14, OFF);
digitalWrite(IN15, OFF);
digitalWrite(IN16, OFF);

        delay(2000);
} } }
```